FUNCTIONAL SURFACE CHEMISTRY OF CARBON-BASED NANOSTRUCTURES

BY

DANER ABDULA

DISSERTATION

Submitted in partial fulfillment of the requirements
for the degree of Doctor of Philosophy in Materials Science and Engineering
in the Graduate College of the
University of Illinois at Urbana-Champaign, 2011

Urbana, Illinois

Doctoral Committee:

Associate Professor Moonsub Shim, Chair and Director of Research
Professor David G. Cahill
Professor Jian-Min Zuo
Assistant Professor Eric Pop

ABSTRACT

The recently discovered abilities to synthesize single-walled carbon nanotubes and prepare single layer graphene have spurred interest in these sp^2-bonded carbon nanostructures. In particular, studies of their potential use in electronic devices are many as silicon integrated circuits are encountering processing limitations, quantum effects, and thermal management issues due to rapid device scaling. Nanotube and graphene implementation in devices does come with significant hurdles itself. Among these issues are the ability to dope these materials and understanding what influences defects have on expected properties. Because these nanostructures are entirely all-surface, with every atom exposed to ambient, introduction of defects and doping by chemical means is expected to be an effective route for addressing these issues. Raman spectroscopy has been a proven characterization method for understanding vibrational and even electronic structure of graphene, nanotubes, and graphite, especially when combined with electrical measurements, due to a wealth of information contained in each spectrum.

In Chapter 1, a discussion of the electronic structure of graphene is presented. This outlines the foundation for all sp^2-bonded carbon electronic properties and is easily extended to carbon nanotubes. Motivation for why these materials are of interest is readily gained. Chapter 2 presents various synthesis/preparation methods for both nanotubes and graphene, discusses fabrication techniques for making devices, and describes characterization methods such as electrical measurements as well as static and time-resolved Raman spectroscopy.

Chapter 3 outlines changes in the Raman spectra of individual metallic single-walled carbon nantoubes (SWNTs) upon sidewall covalent bond formation. It is observed that the initial degree of disorder has a strong influence on covalent sidewall functionalization which has implications on developing electronically selective covalent chemistries and assessing their

selectivity in separating metallic and semiconducting SWNTs. Chapter 4 describes how optical phonon population extinction lifetime is affected by covalent functionalization and doping and includes discussions on static Raman linewidths. Increasing defect concentration is shown to decrease G-band phonon population lifetime and increase G-band linewidth. Doping only increases G-band linewidth, leaving non-equilibrium population decay rate unaffected. Phonon mediated electron scattering is especially strong in nanotubes making optical phonon decay of interest for device applications. Optical phonon decay also has implications on device thermal management.

Chapter 5 treats doping of graphene showing ambient air can lead to inadvertent Fermi level shifts which exemplifies the sensitivity that sp^2-bonded carbon nanostructures have to chemical doping through sidewall adsorption. Removal of this doping allows for an investigation of electron-phonon coupling dependence on temperature, also of interest for devices operating above room temperature. Finally, in Chapter 6, utilizing the information obtained in previous chapters, single carbon nanotube diodes are fabricated and characterized. Electrical performance shows these diodes are nearly ideal and photovoltaic response yields 1.4 nA and 205 mV of short circuit current and open circuit voltage from a single nanotube device. A summary and discussion of future directions in Chapter 7 concludes my work.

To my nieces

for continuously reminding me

our world is a playground

ACKNOWLEDGEMENTS

I thank my research advisor, Professor Moonsub Shim, for the opportunity to work on interesting research, valuable technical input, his high spirit, and his patience with me. It is difficult to imagine another advisor that makes themselves as available to help as he, despite his numerous responsibilities. I owe much to the members of my doctoral committee. Professor Eric Pop was willing to lend a hand when needed and has provided great insight on my projects. Professor Jim Zuo was always a delight to speak with, having a smile on his face and contagious energy. Professor David Cahill has, time and time again, provided invaluable suggestions on much of my work and has left me wishing I could have learned more from him.

Thanks go to my lab mates Khoi Nguyen and Johnathon Tsai for being there to bounce ideas off of and keep work as light-hearted as it could have been. Former members Taner Ozel, Congjun Wang, and Ju-Hee Back have always been encouraging and provided guidance, especially when I first joined the group. I am indebted to the undergraduates that have helped me with my work, Po Shan Hsu and Scott Fong in particular. My hope is that at least some part of the time they dedicated to working with me has helped them as well. I express gratitude to our department who has educated me for two degrees across what seems to be countless years.

Finally, I thank my family. My father and mother have always been emotionally and financially supportive of my studies. Their strictness and expectation of success has forever been backed by love which helps me understand their desires for my future are genuine. Most importantly, I thank my sister who has been strong for all of us. Without her guidance throughout my entire life, I fear where I would be now. Te iubesc sora mea.

TABLE OF CONTENTS

CHAPTER 1

CARBON ALLOTROPES: OVERVIEW OF GRAPHENE AND NANOTUBES

1.1 Graphene

Being one of the most abundant elements, it is understandable that carbon, in all of its forms, is of interest. Such allotropes include sp^3 bonded diamond, one of the hardest materials known, and the sp^2 bonded variety including carbon nanotubes, C_{60}, graphite, and, the mother of them all, single-layer graphene (SLG). SLG is a single sheet of carbon atoms which has just recently been isolated in practice[1] and has led to a surge of investigations into its properties. In particular, very promising electrical characteristics have been uncovered including one of the highest carrier mobilities ever reported of a material.[2, 3] Because these properties are determined by electronic band structure dispersions, E(**k**), it is instructive to understand what makes this structure so special in graphene.

The tight-bonding method for deriving an E(**k**) relation involves solving the central equation,

$$Det[\mathrm{H}-\mathrm{ES}]=0 \qquad \text{Eq. 1.1}$$

with

$$H=\begin{pmatrix} H_{AA} & H_{AB} \\ H_{BA} & H_{BB} \end{pmatrix}, S=\begin{pmatrix} S_{AA} & S_{AB} \\ S_{BA} & S_{BB} \end{pmatrix} \qquad \text{Eq. 1.2}$$

$$H_{\mathrm{i\,j}}=\frac{1}{N}\sum_{\mathrm{R,\,R'}} e^{(i\bar{k}(R-R'))} <\varphi_i(r-R')|H|\varphi_{\mathrm{j}}(r-R)> \qquad \text{Eq. 1.3}$$

$$S_{\mathrm{i\,j}}=\frac{1}{N}\sum_{\mathrm{R,\,R'}} e^{(i\bar{k}(R-R'))} <\varphi_i(r-R')|\varphi_{\mathrm{j}}(r-R)> \qquad \text{Eq. 1.4}$$

The wavefunction of the atomic orbital j at position r of atoms located at lattice sites R or R' is ϕ_{j}, the phase factor is $e^{ik(R-R')}$, and the number of unit cells in the solid is N. The so-called transfer matrix elements H_{ij} correspond to interactions an electron in atom j experiences with the atom i. The elements S_{ij}, in the overlap matrix, correspond to a normalization that modulates the magnitude of the transfer matrix elements depending on the extent that these atomic wavefunctions overlap. It is then proper to define these matrix elements as having empirically determined magnitudes such that all which is left are the phase factors pertinent to the lattice we would like to consider—

$$N \times |H_{\mathrm{i\,j}}| = <\varphi_i(r - R')|H|\varphi_{\mathrm{j}}(r - R)> \equiv t_{\mathrm{i\,j}} \qquad \text{Eq. 1.5}$$

and

$$N \times |S_{\mathrm{i\,j}}| = <\varphi_i(r - R')|\varphi_{\mathrm{j}}(r - R)> \equiv s_{\mathrm{i\,j}} \qquad \text{Eq. 1.6.}$$

The calculations of H_{AA} and H_{BB} are then straightforward when one makes the assumption that electronic wavefunctions die off rapidly in the vicinity of another atom (a standard assumption in tight-bonding),

$$H_{AA} = H_{BB} = \frac{1}{N}\sum_{\mathrm{R=R'}} \varepsilon_{\mathrm{2p}} + \frac{1}{N}\sum_{(R=R'\pm a)} e^{(\pm i\bar{k}a)} t_{\mathrm{A\,A}} \approx \varepsilon_{\mathrm{2p}} \qquad \text{Eq. 1.7}$$

where ε_{2p} is the energy of an electron in the 2p orbital of carbon. The calculation of H_{AB} and H_{BA} then follow with the assumption that nearest neighbor interactions are far stronger than any higher order terms,

$$H_{AB} = H_{BA}{}^{*} = t_{AB}\left(e^{(i\bar{k}R'_1)} + e^{(i\bar{k}R'_2)} + e^{(i\bar{k}R'_3)}\right) = t_{AB}(2e^{(ik_x\frac{a}{2})}\cos(\frac{\sqrt{(3)}}{2}k_y a) + e^{(-ik_x\frac{a}{2})}),$$

where R'_1, etc., are defined as in Figure 1.1.

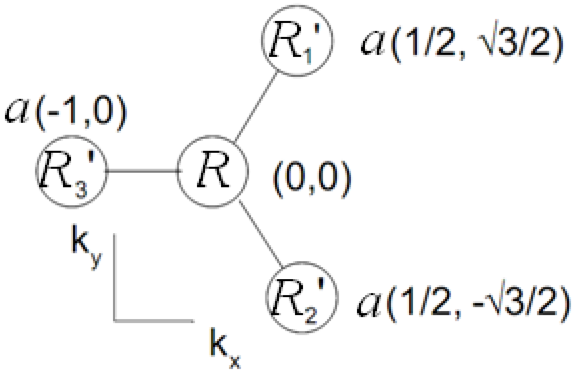

Figure 1.1. Locations of nearest neighbor atoms in graphene. Coordinates are in real space and the cooresponding reciprocal space directions are noted.

By similar methods, the calculation of the overlap matrix can be carried out to finally yield

$$(\varepsilon_{2\mathrm{p}} - E) \times (\varepsilon_{2\mathrm{p}} - E) - \left[(t - Es)\left(2e^{\left(ik_x\frac{a}{2}\right)}\cos\left(k_y a\frac{\sqrt{(3)}}{2}\right) + e^{(-ik_x a)}\right)\right] \times$$

$$\left[(t - Es)\left(2e^{\left(-ik_x\frac{a}{2}\right)}\cos\left(k_y a\frac{\sqrt{(3)}}{2}\right)\right) + e^{(ik_x a)}\right] = 0 \qquad \text{Eq. 1.8.}$$

With the Slater-Koster approximation that the overlap parameter *s*=0, the E(**k**) relation for a graphene sheet is

$$E = \varepsilon_{2\mathrm{p}} \mp t\left(1 + 4\cos\left(k_y a\frac{\sqrt{(3)}}{2}\right)\cos\left(3\mathrm{k}_x\frac{a}{2}\right) + 4\cos^2\left(k_y a\frac{\sqrt{(3)}}{2}\right)\right)^{1/2} \qquad \text{Eq. 1.9}$$

which is symmetric around the energy of a 2p orbital electron as is evident. Equation 1.9 is plotted in Figure 1.2 with $\varepsilon_{2\mathrm{p}} = 0$ and t=0.

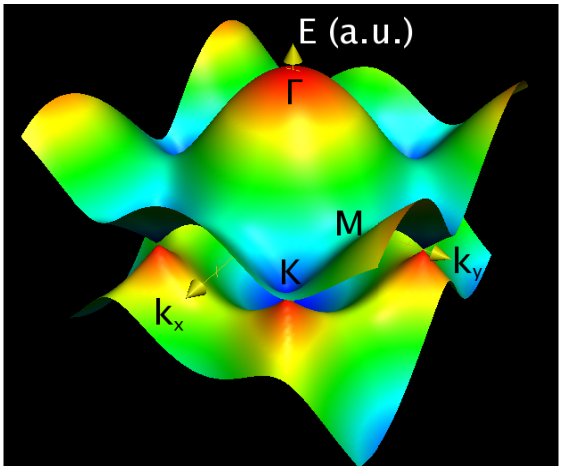

Figure 1.2. Dispersion relation of single layer graphene calculated using tight-bonding methods described in the text. Brillouin zone high symmetry points are labeled. Dirac points separating conduction and valence bands are evident at K and equivalent.

With an intrinsic, undoped piece of SLG, the Fermi level (E_F) exactly separates the conduction and valence bands (E_F=E_o). In this situation, the only part of the energy surface that has a non-zero density of states (where thermal smearing of ~kT/2 each side of E_o is taken into account) is at the K-point (and equivalent) of the Brillouin zone. The electron dispersion relation at these special "Dirac points" of charge neutrality is interesting because it is discontinuous. The mobility, according to Sommerfeld theory, is μ=qτ/m* with τ being the carrier lifetime and m* the carrier effective mass. This mass can be determined from the electronic dispersion as $m^* = \hbar^2 (d^2\,E/dk^2)^{-1}$. Therefore, it is seen that the second derivative of E(**k**) for graphene at **K** tends to infinity and hence m* approaches zero, a characteristic of the so-called "massless" Dirac fermions. Since m* approaches zero, μ goes toward infinity. In reality, this is not the case due to electron-phonon and electron-electron interactions as well as defect scattering (substrate or structural).[4, 5]

1.2 Carbon Nanotubes

If a sheet of graphene is rolled into a seamless cylinder, a carbon nanotube (CNT) is formed. The "nano" comes from the diameter of these structures being on the order of a nanometer. Multiple sheets can also form individual concentric tubes, the result of which is termed a multi-walled carbon nanotube, which can have much larger diameters. These types of CNTs are primarily of interest due to their mechanical properties. Electronically, single-walled CNTs have the desirable properties that have made them the subject of device integration, including mobilities close to that of SLG. [6-10]

The advantage that CNTs have over graphene is tunable electronic properties depending on the way they are rolled. There are a variety of ways that this can be done (Figure 1.3) giving a tube described by its chiral vector, $\mathbf{C_h}$= (n, m), on the graphene lattice which when this vector is connected head to tail defines the nanotube circumference. The length of the reciprocal space vector of the corresponding chiral vector (call this $\mathbf{K_1}$) is therefore different for each chirality. The allowed k values in the $\mathbf{K_1}$ direction are discretized in reciprocal space since the chiral vector is both the unit cell length and the entire length of one dimension of the lattice. The number of discrete k values is given by the number of Brillouin zones that exist in the unit cell of a given tube and are separated by $|\mathbf{K_1}|$. If one of these vectors lies on the corner of a Brillouin zone of graphene (a Dirac point), then it is metallic, otherwise it is semiconducting. Statistically, about 2/3 of the possible ways a tube can be rolled seamlessly will give a semiconducting nanotube (when n-m does not equal an integer multiple of 3), and the other 1/3 are metallic (n-m equals an integer multiple of 3). “Armchair” nanotubes (n=m) are said to be truly metallic because they are the only class of nanotubes where the conduction and valence bands at **K** actually meet (versus having a small curvatuve-induced bandgap in all other metallic nanotubes).

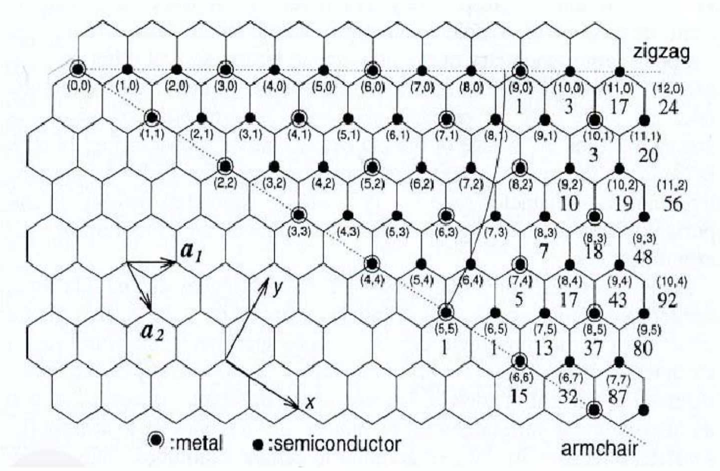

Figure 1.3. Different ways a nanotube can be rolled from a graphene sheet. (n, m) indices correspond to chirality and, when overlapped with (0, 0) form the circumference of an (n, m) nanotube.[11]

Again, it is useful to look at the various E(**k**) that different chirality nanotubes can have to understand their electronic properties. We can start with the result for graphene, Equation 1.9. To apply this to CNTs, we must consider the dimensional restriction that they carry as well as rotate k_x and k_y to coincide with the directions of $\mathbf{C_h}$ and T (the unit cell vector along the tube axis) respectively (thus, $k_y{}'$ will remain as the only variable since we desire E($\mathbf{K_2}$), i.e. the dispersion along the length of the tube). This is simply done by the proper axes transformation: $\begin{pmatrix} k'_x\hat{C_h} \\ k'_y\hat{T} \end{pmatrix} = \begin{pmatrix} \cos\theta & -\sin\theta \\ \sin\theta & \cos\theta \end{pmatrix}\begin{pmatrix} k_x \\ k_y \end{pmatrix}$ where $\theta = 30^o - \theta_{Ch}$ and θ_{Ch} is the chiral angle as will be defined shortly. The quantization of k'_x is expressed as $k'_x = \mu 2\frac{\pi}{(|C_h|)}$ where μ= 0, 1, ..., N-1 and each value corresponds to one band in the Brillouin zone. N is defined in terms of the chiral integers as $N = \frac{(|C_h \times T|)}{(|a_1 \times a_2|)} = 2\frac{(m^2+n^2+nm)}{d_R}$ with a_1 and a_2 being the unit cell vectors in real space and d_R the greatest common divisor of (2m+n) and (2n+m). This is termed the zone folding technique which essentially imposes all the bands of each Brillouin zone in a unit cell into one zone which naturally runs from -π/T to π/T (the length of $\mathbf{K_2}$). Thus, our final E(**k**) relation is that of graphene, Equation 1.9, with quantization and axes rotation accounted for in k_x and k_y:

$$k_x = \frac{\left(2\pi\mu\cos\left(\frac{\pi}{6}-\arctan\left(\sqrt{3}\frac{m}{(2\mathrm{n}+m)}\right)\right)\right)}{\left(\sqrt{3}a\sqrt{(n^2+m^2+nm)}\right)} + k'_y\sin\left(\frac{\pi}{6} - \arctan\left(\sqrt{3}\frac{m}{(2\mathrm{n}+m)}\right)\right) \qquad \text{Eq. 1.10}$$

$$k_y = (k'_y - k_x\sin(\frac{\pi}{6} - \arctan(\sqrt{3}\frac{m}{(2\mathrm{n}+m)}))) \times \cos^{-1}(\frac{\pi}{6} - \arctan(\sqrt{3}\frac{m}{(2\mathrm{n}+m)})) \qquad \text{Eq. 1.11}$$

Therefore, we have a universal E(**k**) relation for any chirality tube that is a function of only the chiral integers n and m. The E(**k**) diagrams of two nanotubes, one metallic and one semiconducting are shown in Figure 1.4 with ε_{2p} set as the reference energy and t=3eV. It is apparent, then, that if growth methods providing control over chirality can be achieved, CNTs can offer a vast array of electronic properties to choose from according to the desired application.

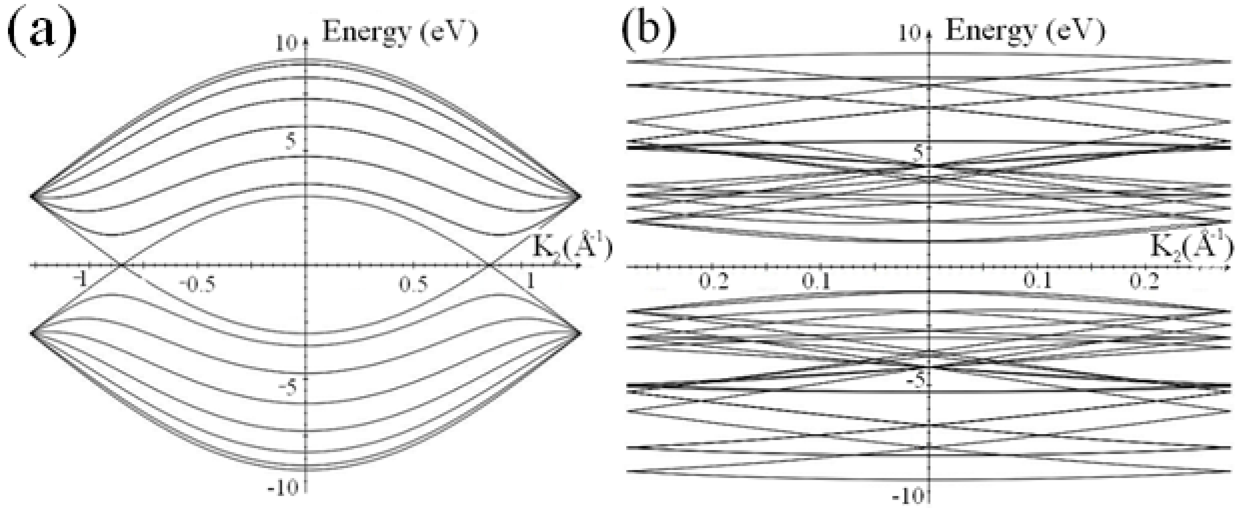

Figure 1.4. E(k) dispersion relations for a (7,7) metallic CNT (a) and a (4,2) semiconducting CNT (b) obtained from using Equations 1.9, 1.10 and 1.11 in the text.

1.3 Summary

The various allotropes of carbon all have intriguing properties, but those of sp^2 bonded graphene and carbon nanotubes are particularly interesting in the electronic transport realm. For graphene, E(**k**)=ħ**k**v, which is exceptional considering it is a linear dispersion relation only involving carrier velocity, v, and not carrier mass. One can think of graphene as a playground for electrons where, ideally, they are unperturbed by the lattice itself. This material, therefore, is an ideal candidate for investigating 2-dimensional electronic phenomena. Carbon nanotubes provide a wide range of electrical characteristics, from metallic to semiconducting, based on chirality. If chirality can be controlled, CNTs can essentially be implemented for any current carrying purpose including transistors for logic and interconnects that connect them.

1.4 References

[1] K. S. Novoselov, D. Jiang, F. Schedin, T. J. Booth, V. V. Khotkevich, S. V. Morozov, and A. K. Geim, Proc. Natl. Acad. Sci. U.S.A. **102**, 10451 (2005).

[2] X. Du, I. Skachko, A. Barker, and E. Y. Andrei, Nat. Nanotech. **3**, 491 (2008).

[3] S. V. Morozov, N. S. Novoselov, M. I. Katsnelson, F. Schedin, D. C. Elias, J. A. Jaszczak, and A. K. Geim, Phys. Rev. Lett. **100**, 016602 (2008).

[4] S. Pisana, M. Lazzeri, C. Casiraghi, K. S. Novoselov, A. K. Geim, A. C. Ferrari, and F. Mauri, Nat. Mater. **6**, 198 (2007).

[5] J. Chen, C. Jang, S. Xiao, M. Ishigami, and M. S. Fuhrer, Nat. Nanotech. **3**, 206 (2008).

[6] S. J. Tans, A. R. M. Verschueren, and C. Dekker, Nature **393**, 49 (1998).

[7] J. Kong, N. R. Franklin, C. Zhou, M. G. Chapline, S. Peng, K. Cho, and H. Dai, Science **287**, 622 (2000).

[8] S. J. Kang, C. Kocabas, T. Ozel, M. Shim, N. Pimparkar, M. A. Alam, S. V. Rotkin, and J. A. Rogers, Nat. Nanotech. **2**, 230 (2007).

[9] V. Sazonova, Y. Yaish, H. Ustunel, D. Roundy, T. A. Arias, and P. L. McEuen, Nature **431**, 284 (2004).

[10] T. Durkop, S. A. Getty, E. Cobas, and M. S. Fuhrer, Nano Lett. **4**, 35 (2004).

[11] M. S. Dresselhaus, G. Dresselhaus, and P. C. Ecklund, Science of Fullerenes and Carbon Nanotubes, AP, (New York, 1996).

CHAPTER 2

EXPERIMENTAL METHODS: SYNTHESIS, FABRICATION, AND CHARACTERIZATION TECHNIQUES

2.1 Graphene Production

2.1.1 Graphene Synthesis by Chemical Vapor Deposition (CVD)

There are a few ways graphene synthesis by chemical vapor deposition can be achieved. One is with simple heating of a SiC substrate at high temperature to the point where Si at the surface sublimes leaving graphene behind.[1, 2] Another method involves flowing a carbonaceous source over a Ni substrate which dissolves atomic carbon up to saturation and is then precipitated out as graphene.[3, 4] By far, the greatest advance in SLG synthesis is CVD using Cu substrates which provides the cleanest, most continuous, and highest fraction of single layer product.[5]

Copper catalyzed SLG is grown in a hot-wall quartz tube furnace similar to methods described in ref. [5]. First, copper foils about 30 μm thick are cleaned with acetone and isopropyl alcohol. The foils are then annealed at 1000^oC for 30 min under 10 sccm H_2 and 20 mTorr vacuum to grow the Cu grains. After annealing, the foils are inserted into 70^oC glacial acetic acid for 5min to etch off Cu oxides from the surface. For growth, the foils are placed back into the furnace and heated to 1000^oC under 10 sccm H_2 and vacuum upon which 35 sccm CH_4 is introduced and the pressure reaches ~600 mTorr. Growth runs for 30 min. Transfer of SLG off Cu foils and onto arbitrary substrates (primarily 300 nm SiO_2 on Si) is achieved by spin coating poly(methyl methacrylate) (PMMA, A6 495K MicroChem) onto the foils at 3000 rpm for 30 s, curing at 180^oC for 2 min, and placing the foils Cu-side down into a solution of 0.05 g/mL

$Fe(NO3)_3$ (Sigma) until the Cu is completely etched and PMMA on SLG is left. These films are transferred onto a bath of de-ionized water and finally onto a host substrate by dipping the substrate into the bath and lifting the PMMA/SLG film with the substrate out of the water. Substrates are allowed to dry and acetone is used to dissolve the PMMA leaving SLG to remain. An example of CVD SLG transferred onto 300 nm SiO_2 on Si is shown in Figure 2.1.

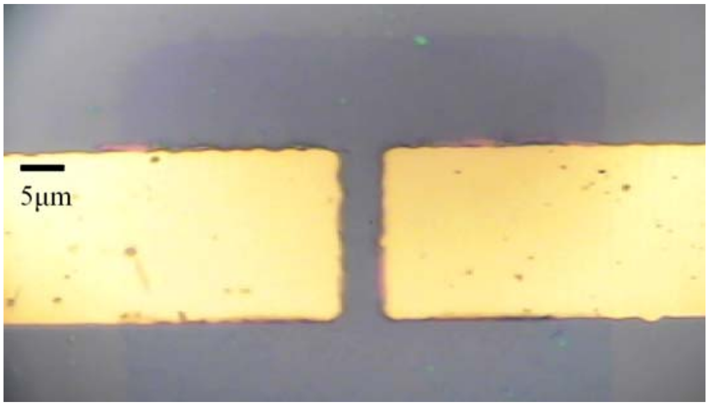

Figure 2.1. Optical image of single layer graphene synthesized using CVD on Cu foil. Substrate is 300nm SiO_2 on Si. Faint blue is graphene patterned using reactive ion etching. Yellow features are Au electrodes used to probe electrical properties.

2.1.2 Mechanical Exfoliation of Single Layer Graphene

The highest quality SLG samples are produced by mechanical exfoliation of graphite.[6] This is primarily due to source quality since graphitic carbon is usually synthesized at high temperature or at high pressure by geological processes over long periods of time. It is important to understand that graphite (not diamond) is the most thermodynamically stable form of carbon over a wide range of temperatures and pressures which is why, with time and thermal or compressive driving force, high quality graphite results.

Mechanical exfoliation starts with pealing graphitic layers off the source. Simple single-sided tape can be used for this procedure. Various host substrates can be used, but good results with SiO_2/Si having either 90 nm or 300 nm oxides have been obtained. These particular oxide thicknesses are special because they allow SLG to be clearly seen with an optical microscope due to high reflection at the air/SLG/SiO_2 interface.[7, 8] The graphitic layers on the tape are pressed onto the substrate and then peeled off. Occasionally, SLG flakes are left behind similar to what is shown in Figure 2.2.

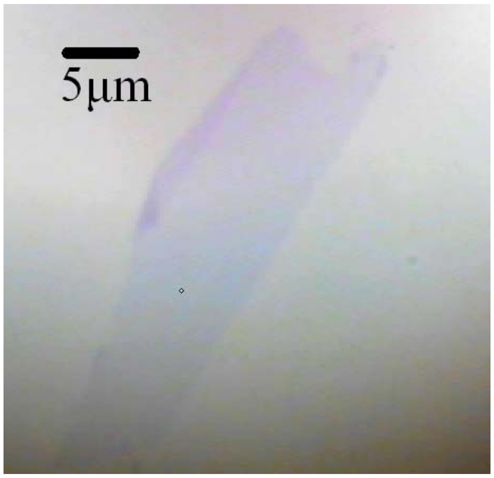

Figure 2.2. Example optical image of exfoliated single layer graphene on 300nm SiO_2/Si substrate.

2.2 Carbon Nanotube Synthesis

2.2.1 Single-Walled Carbon Nanotubes by Chemical Vapor Deposition

There are many variations of CNT synthesis using CVD [9-15], but all of the techniques share the same basic principle; saturate a nanometer-scale catalyst particle, usually a transition metal (e.g. Fe, Ni, Co) , with carbon from a carbon source (e.g. ablated graphite, hydrocarbon gases) at high temperature (usually greater than 600^{o}C). Once the catalyst carbon concentration is sufficient, the carbon supposedly precipitates out as a cylindrical tube.[16]

A well-established method of growing single-walled CNTs uses ferritin organic nanoparticles as catalyst. Ferritin is a biological macromolecular protein which stores Fe in its inner core. The particles (diluted with water depending on desired yield density) are spin coated from an aqueous solution onto SiO_2/Si substrates at 2000 rpm for 30 s after allowing the catalyst to rest on substrate for 1 min. The protein outer shell is burned off by calcining the substrate to 800°C in air. The sample is then placed in a hot wall furnace where it is heated to 900°C under Ar and H_2 flow (150 sccm each). Once this temperature is reached nanotube growth is initiated by terminating Ar flow and replacing it with CH_4 into the reaction chamber at a rate of 300 sccm for 15 min. Cooling is done under 150 sccm of Ar and H_2 each. Nanotube density is controlled with catalyst concentration (typically 10X - 100,000X diluted from stock solution). A scanning electron microscope (SEM) image of CNTs synthesized with this method is shown in Figure 2.3.

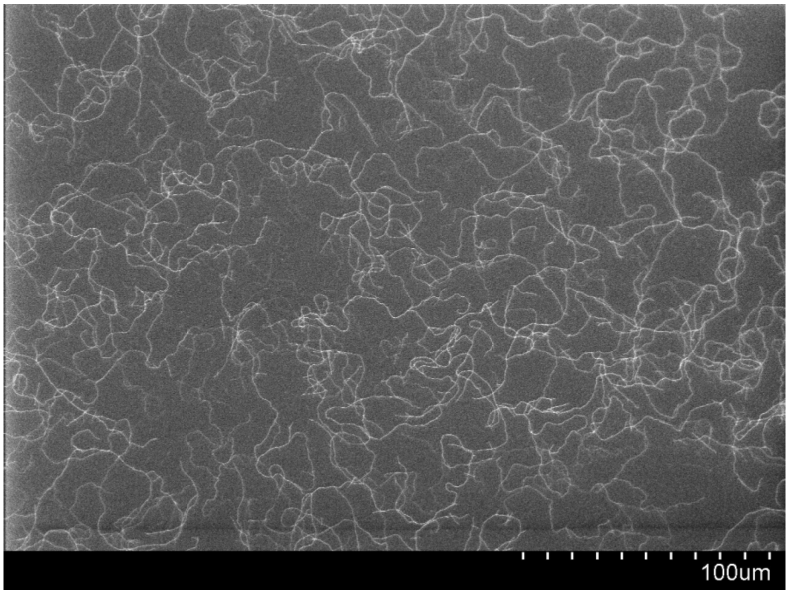

Figure 2.3. SEM image of CVD synthesized CNTs on SiO_2/Si substrate. 1kV accelerating voltage.

Substrate selection is important for nanotube growth and can even lead to yields with unique characteristics. For example, CVD growth on crystalline quartz substrates aligns the nanotubes along a particular direction[17, 18] supposedly because of strong interactions with the substrate[19-21]. The visual difference of samples grown on quartz is striking (Figure 2.4). This discovery advances the use of CNTs in electronics significantly due to the predictability of device geometry, and, in conjunction with photolithography, location.

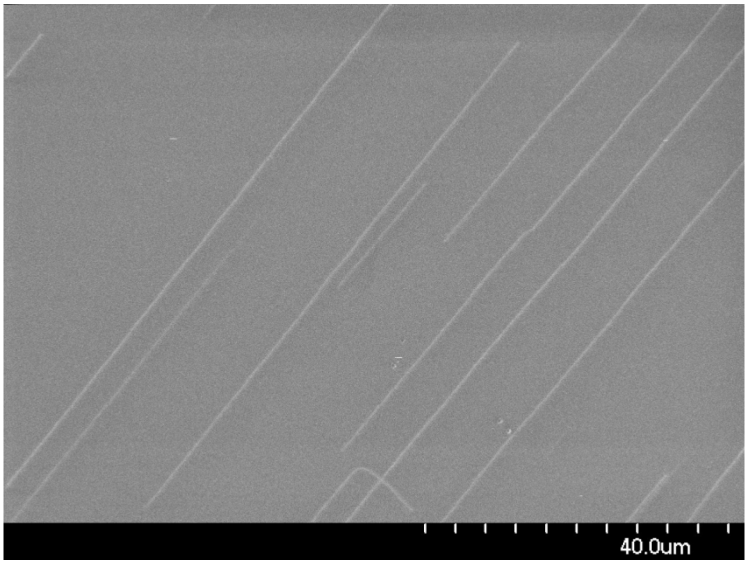

Figure 2.4. SEM image of CVD synthesized CNTs on crystalline quartz substrate. 1 kV accelerating voltage.

2.2.2 High Pressure Carbon Monoxide Synthesis

A method for achieving bulk yields of single-walled CNTs was developed by Nikolaev et al. termed the high-pressure carbon monoxide procedure or, HiPCO.[22] Because of high yields, HiPCO nanotubes are useful for measurements on thin film samples, such as those in Chapter 4. This method involves using CO disproportionation as a carbon source and $Fe(CO)_5$ decomposition to form iron catalyst, all occurring in the CVD reactor tube simultaneously. Between 1000-2000 sccm CO is bubbled through a solution of $Fe(CO)_5$ at 0^oC producing ~7 Torr partial pressure which is diluted with more CO to a partial pressure of <25 mTorr. This mixture is introduced in a hot wall CVD system (T between 800 and 1200^oC) and the nanotube soot deposits and is collected off the cool areas of the quartz reactor tube. This growth method is continuous, producing high yields in a short amount of time and nanotubes are primarily single-walled and can have diameters as small as 0.7 nm meaning large bandgap semiconducting nanotubes can be obtained.

2.2.3 Vertically Aligned Carbon Nanotube Synthesis

Continuing with the theme of mass production of nanotubes, CVD can also be used to growth thick forests of vertically aligned carbon nanotubes. One way this can be achieved is by water assisted growth using Co/Mo catalyst and ethanol as a carbon source.[23] The catalyst is made of 12 mg cobalt (III) acetate and 4 mg molybdenum (II) acetate dimer sonicated in 16 g of ethanol for 1 hr. The solution remains suitable for growth for only 3-4 hrs. SiO_2/Si substrates are dip coated in the catalyst for 1 min and pulled out at a speed of 1 mm/s upon which they are calcined in air at 400^oC for 5 min so catalyst particles can coalesce. The substrate is heated to 800^oC under vacuum in a quartz reactor tube with 1000 sccm Ar and 9 sccm H_2 totaling 20 mTorr pressure. Growth is initiated by redirecting the flow gases through a mixture of 0.67 vol% H_2O in ethanol for 30 min increasing base pressure to 30 mTorr. Yield is high density with film thicknesses up to 20 μm. An example SEM image of these nanotubes is shown in Figure 2.5 (left).

Another method provides "supergrowth" of CNTs up to 1 mm tall forests, using acetylene.[24] 15 nm of Al is evaporated using electron beam evaporation onto SiO_2/Si substrates and exposed to air so native oxide can form. 1 nm of Fe is then deposited and the samples are ready for growth. The substrates are heated to 750^oC under 120 sccm Ar and 80 sccm H_2 (no vacuum). Growth is carried out at 105 sccm Ar, 80 sccm H_2, and 15 sccm C_2H_4 for 20 min at atmospheric pressure. High density, 1 mm tall forests of nanotubes are formed with high substrate coverage, as shown in Figure 2.5 (right). The downside to both growth methods is that there is a high multi-walled CNT content.[23, 24]

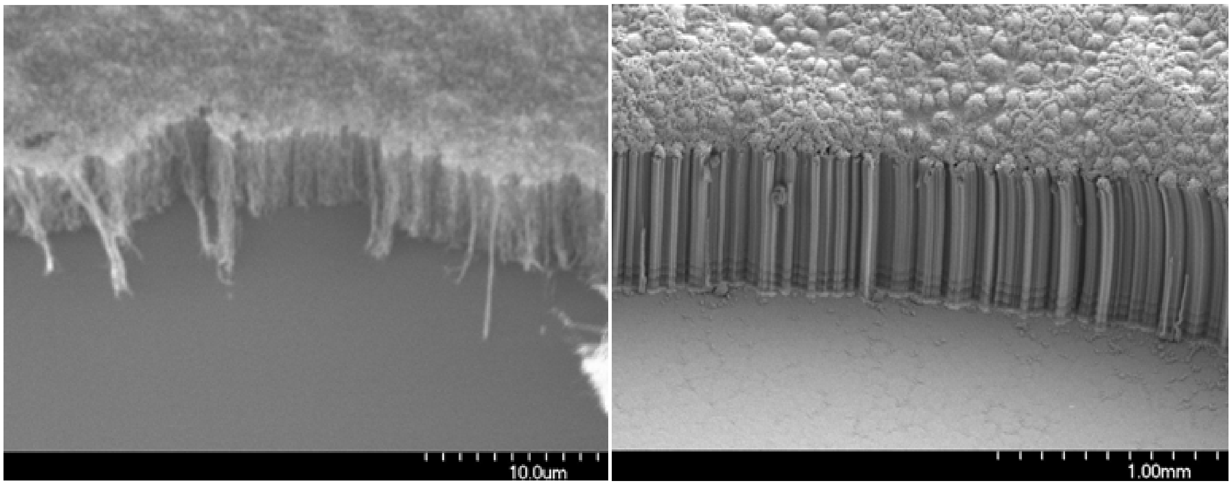

Figure 2.5. Vertically aligned carbon nanotubes synthesized using ethanol (left) and acetylene (right) chemical vapor deposition. 1 kV accelerating voltage.

2.3 Device Fabrication

2.3.1 Processing

Here, a description of how a simple transistor is made out of either CNTs or graphene which exemplifies different processes that can be used to create various other device geometries depending on the application or desired function. First, the materials synthesis (previous section) is carried out. If the goal is a single nanotube transistor, ferritin concentration is adjusted (usually 100,000X diluted from Sigma source) such that random placement of electrodes gives roughly a 20% yield in single tube devices on quartz substrate. For thin film transistors, ferritin of higher concentration or electron beam evaporation of ~0.5 nm Fe can be used for growth. Adjacent devices can be shorted if the nanotube density is too high. This can be averted by photolithographically patterning catalyst islands so that ferritin or Fe is deposited only in specific areas on the substrate onto which electrodes can be aligned. If growth needs to be random, for whatever reason, photolithography can be used to cover the channel areas of each transistor and reactive ion etching (RIE) with 100 W, 200 mTorr base pressure, and 20 sccm O_2 for 1 min can be used to etch all tubes that short adjacent devices. Graphene can be patterned using this method also, which is especially useful for CVD grown samples which provide large area coverage. Exfoliated graphene is usually 5-10 μm each side of a flake so patterning is generally not necessary. Because graphene is visible on 300 nm SiO_2/Si, the electrode mask can be aligned directly on top of SLG during lithography to make transistors.

Once the material of interest is prepared on substrate, photoresist is spun on the sample to ready it for lithography. The choices here are usually Shipley 1805, AZ 5214, or 495K PMMA with anisole solvent. Shipley resist provides quick exposure—6 s with mid-UV exposure (120 mJ/cm^2) as well as quick development, 10 s with MicroChem 351 developer. AZ resist is generally cleaner and can still be used with mid-UV irradiation—14 s exposure (120 mJ/cm^2), and about 1min development with MicroChem 327 MIF developer. PMMA provides the cleanest processing with best feature integrity, but requires deep UV exposure for a long time—up to 20 min at 2 J/cm^2 fluence and up to 10 min of development in methyl isobutyl ketone (MIBK) developer. All resists are spun at 3000 rpm for 30 s. Shipley and AZ are baked after spinning at 110^{o}C for 1 min while PMMA requires 180^{o}C for 2 min.

Metal evaporation is required, after features in the resist are developed, to make electrodes. Electron beam evaporation is utilized for this procedure, operated at a vacuum of ~3x10^{-6} Torr baseline pressure. An initial "wetting" layer of either relatively reactive Ti or Cr is needed for the electrodes to bind well to the SiO_2 substrate. Roughly 2-3 nm thick layers of either works well. Au is then evaporated to a thickness of ~35 nm making the electrodes. All evaporation is done at room temperature with substrate rotation (to promote uniformity) and at ~1 Å/s. Liftoff in acetone removes excess resist leaving behind the completed transistors.

2.3.2 Electrical Characterization

A source measurement unit (SMU) is used to apply voltage and read current on the sample channel to obtain transfer characteristics for devices fabricated. These are NOT 4-probe measurements so contact resistances can become an issue, but thermal annealing of devices usually alleviates this problem.[25] Example gate dependences are shown in Figure 2.6 for both SLG grown by CVD and a semiconducting nanotube grown with ferritin-catalyzed CVD. Two different gating methods are also represented. Back gating uses the Si substrate as a conductive medium to create capacitance in the CNT or SLG channel. Unfortunately, SiO_2 may have charge traps and also facilitates adsorption of water both of which can cause the visible hysteresis in gating behavior.[26-28] Using polymer electrolyte top gating with a Ag or Au gate electrode can alleviate this problem since gating efficiency increases to nearly 100% due to high capacitance of the ionic double layer (small Debye length). As seen in Figure 2.6, the graphene transistor gated with $LiClO_4$-$3H_2O$ in poly(ethylene oxide) (PEO, M_n=550) with a ratio of 2.4:1 by weight has nearly no hysteresis compared to the back-gated CNT transistor. Because CNTs and SLG are doped p-type in air,[29, 30] it sometimes becomes necessary to counter-dope them to push the threshold voltage closer to 0 V. If poly(ethylenimine) (PEI, Mn=25,000) is substituted for PEO in a 1:1 ratio with Li^+, this can be achieved since PEI is a good n-type dopant of carbon nanotubes.[31,32]

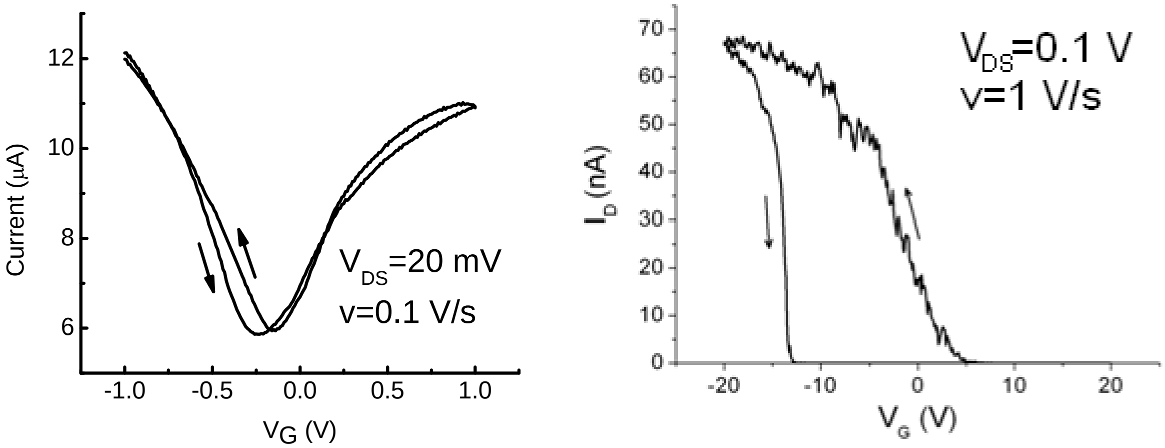

Figure 2.6. (Left) I-V_G curve for SLG grown using CVD. Polymer electrolyte top gate used. Forward and reverse sweeps shown. (Right) I-V_G curve for a (18, 7) semiconducting carbon nanotube transistor gated with back-gating.

2.4 Static Raman Spectroscopy of Graphene and Carbon Nanotubes

2.4.1 General Concepts and Typical Experimental Apparatus

Resonant Raman spectroscopy involves an excitation of a material's electronic and vibrational structure simultaneously. Experimentally, a monochromatic laser is incident on a material of choice and the majority of the light is Rayleigh scattered. Some photons, on the other hand, interact inelastically with the material such that the light undergoes a red- (Stokes) or blue-shift (anti-Stokes) in energy by releasing or absorbing a phonon from the material. If there are electronic excitations that are resonant with energy of incident photons, the process is said to be resonant and an increase in signal results. These "Raman shifts" are what appear in Raman spectra and contain a wealth of information including phonon energies.

In this work, three different laser lines, 785 nm, 633 nm, and 532 nm, have been used and the choice is specifically noted throughout. As described earlier, carbon nanotube electronic structure can change depending on chirality therefore, only certain nanotubes will meet the resonance condition with a given wavelength. The laser beam is first passed through a laserline filter which makes the beam highly monochromatic. This is important so that spectra peak widths are not broadened by excitation energy distributions. The beam then gets focused onto the sample using an objective lens. It is important to note here that, since this is an optical technique, spatial resolution is limited by the diffraction condition so traditional "micro" Raman spectroscopy cannot be done with spot sizes smaller than ~0.5 μm. The objective then collects both the Rayleigh and Raman scattered light and passes it through either an edge or notch filter which blocks the Rayleigh beam and lets the Raman light through. A notch filter is necessary when detection of both Stokes and anti-Stokes scattered light is desired. Raman scattered light is then passed through a diffraction grating and is collected using a thermoelectrically cooled charge-coupled device (CCD) to produce energy spectra, such as those shown in Figure 2.7 for graphene and carbon nanotubes. Some systems have automatically moveable diffraction gratings such that the highest resolution can be obtained without having to sacrifice spectral range. Knowing that each spectrum peak location corresponds to the extent of red- or blue-shifting and having an understanding of the photon-electron-phonon scattering mechanism can then lead to determining the phonon energy. This scattering mechanism, just like any other, requires energy and momentum conservation. Because the incident and emitted photons have relatively small momentum, phonon emission/absorption must have a net momentum change near zero, $\sum_i \boldsymbol{q_i} \sim 0$, where q is the wavevector of all phonons involved in Raman scattering, defining the selection rules. Here we consider the scattering mechanisms that give rise to the peaks of spectra shown in Figure 2.7.

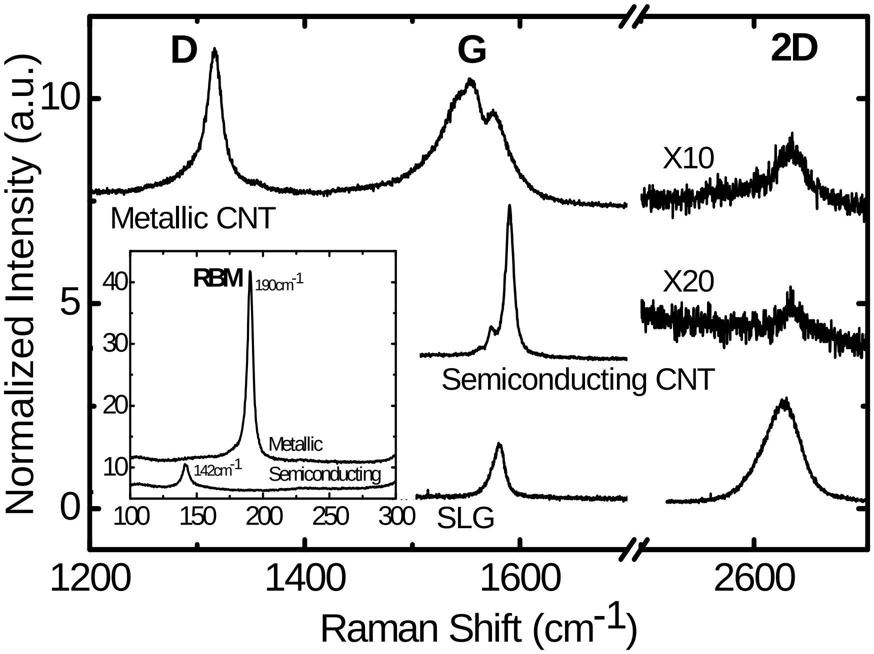

Figure 2.7. Example Raman spectra for semiconducting and metallic carbon nanotubes as well as single layer graphene. D-, G-, and 2D-bands shown as well as the RBM region for the nanotubes in the inset. 633 nm laser used. 2D-bands for carbon nanotubes scaled for visibility. There are no D-band peaks for semiconducting CNT and SLG.

2.4.2 2D-band

The 2D-band and the D-band are both "double-resonant" processes meaning that two scattering events are required for these **K**-point iTO or LO (in-plane transverse optical/longitudinal optical) degenerate phonons to be seen with Raman due to momentum conservation.[33, 34] For the 2D-band, a virtual electronic excitation due to laser energy resonance facilitates two-phonon scattering of the virtual carrier from one **K**-point across the Brillouin zone to **K'** with a single phonon (momentum **q**), and then back to the original position in the Brillouin zone with another phonon (momentum –**q**) (Figure 2.8). Raman scattering ends with virtual carrier relaxation and photon emission. The anti-Stokes process is different only in that phonons increase emitted photon energy. Figure 2.7 shows that graphene has a significantly higher intensity 2D-band peak than nanotubes. Because CNTs have an additional dimension of confinement, it is not just the magnitude of **q** that must fulfill selection rules, but also its direction which limits peak intensity.

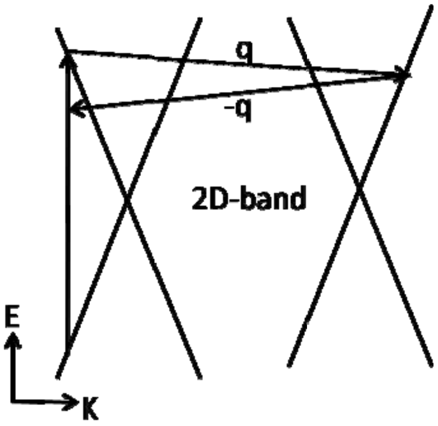

Figure 2.8. Stokes scattering mechanism giving rise to the 2D-band spectrum peak (equivalent for virtual holes not shown).

For graphene, this spectral feature is especially useful because it can be used to count layers.[35-38] The most distinguishable case is between single layer graphene, consisting of a single peak 2D-band, and bilayer graphene with a 2D-band comprised of four peaks. The reason bilayer is different is because of interlayer interaction causing an asymmetric splitting of π and π* electronic bands (i.e., valence and conduction bands) which produces a total of four possible phonon momenta, $\mathbf{q}_{1\text{-}4}$, that preserve momentum conservation.[37, 38] That is, interlayer interaction breaks the degeneracy of the A and B sublattices so scattering can occur between two pairs of Dirac cones. Therefore, this slight splitting in **K**-point phonon momentum results in a broken energy degeneracy which shows up as multiple peaks in the 2D-band. Interlayer interactions differ enough between 2- to 5-layer graphene that the extent of 2D-band peak splitting is different for each, causing characteristic lineshapes that can be used to count layers. With thicker than 5-layer graphene, these interactions start to converge and result in a lineshape equivalent to that of graphite.

One last note about the 2D-band is that it is dispersive with laser energy, as all double resonance processes are (including the D-band). [33, 34, 39, 40] Generally, this dispersion is linear with a dependence of $\delta\omega_{2D}/\delta E_{laser}$~$100cm^{-1}/eV$ for various sp^2-bonded carbon materials.[34, 40-42] With knowledge of E(**k**) near the Dirac cones, this dispersive 2D-band behavior can be used to map E(**q**), the phonon dispersion for **K**-point phonons.

2.4.3 D-band

The D-band is also a double resonant process, similar to the 2D-band, but momentum conservation is not preserved with emission/absorption of a second iTO or LO phonon, but with an elastic scattering event instead (Figure 2.9). Since only one **K**-point phonon emission is involved, the D-band comes up at half the energy of the 2D-band in Stokes Raman spectra. Elastic scattering occurs with any symmetry-breaking defect in sp^2-bonded carbon materials so this peak is useful for determining sample quality. [33, 34, 43-48] The way this is usually done is by normalizing the integrated area of the D-band peak to that of the G-band (to be discussed), so that variance in signal across measurements is taken into account, leading to the ratio I_D/I_G. This has been established as a good way to measure relative defect concentrations and is further discussed in detail in Chapter 3.[47]

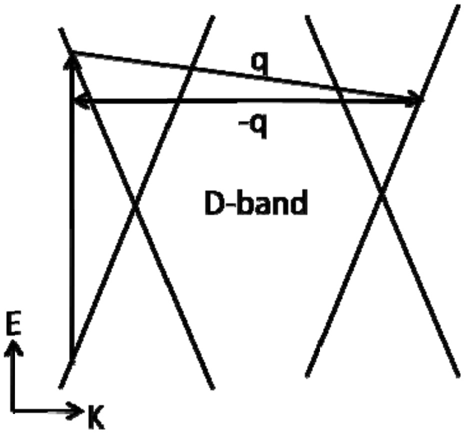

Figure 2.9. Stokes scattering mechanism giving rise to the D-band spectrum peak. An elastic scattering event occurs (equivalent for virtual holes not shown).

Another piece of useful information that the D-band provides is doping dependent frequency.[49] A monotonic downshift of D-band peak position with increasing n-type doping provides a way to determine where the sample Fermi level lies, in conjunction with high efficiency polymer top-gating and electrical measurements to determine the charge-neutral D-band frequency. This dependence supposedly arises due to the **K**-point phonon being an in-plane vibration which is sensitive to carrier concentration, similar to the G-band (to be discussed). Finally, again, because this mode arises due to double resonant scattering, it is dispersive with energy, similar to the 2D-band. This relationship is also linear with a dependence of $\delta\omega_{2D}/\delta E_{laser}$~$50cm^{-1}/eV$, half that of the 2D-band because only one phonon is involved in this scattering process.[34, 40-42, 50]

2.4.4 G-band

In graphene, the G-band peak arises due to an E_{2G}-symmetry in-plane **Γ**-point phonon. Since it is a zone-center phonon, it has no momentum meaning the virtual carrier does not traverse the Brillouin zone and back, therefore this peak is not dispersive with laser energy (Figure 2.10). The LO (longitudinal optical) and iTO phonon branches are degenerate at the **Γ**-

point because the A and B sublattices are equivalent therefore, a single Lorentzian peak makes up the G-band.[50] In semiconducting CNTs, this degeneracy is broken due to curvature and phonon wavevector quantization as a result of confinement, both causing the iTO phonon frequency to downshift (Figure 2.7).[34] When uniaxial strain is applied to graphene it splits the G-band by strongly downshifting one of the peaks.[51] In analogy, the curvature of the circumference does the same in nanotubes[33] which has led to redefining nomenclature for phonons (along with polarization dependent intensity)—LO being vibrations along the nanotube axis, and iTO being those along the circumference. The simplest nanotubes to consider, where chirality does not complicate the matter, are zig-zag CNTs where the LO peak truly corresponds to vibrations along the nanotube axis and the single, downshifted iTO peak comes from vibrations along the circumference. Curvature is further proven to be an underlying reason for multiple peaks in the G-band when considering the LO mode frequency is independent of nanotube diameter while the iTO mode shows a dependence.[33] To summarize, the physical structure of carbon nanotubes breaks E_{2G} symmetry of the G-band phonon, resulting in multiple peaks in the G-band. Curvature and phonon wavevector quantization causes peak downshifts.

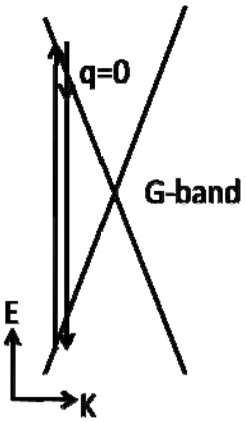

Figure 2.10. Stokes scattering mechanism giving rise to the G-band spectrum peak. E_{2G} phonons are Γ-point so their wavevector is zero (equivalent for virtual holes not shown).

For metallic nanotubes, the lineshape is significantly different than that of even semiconducting CNTs (Figure 2.7). Though curvature and confinement effects are still present, lineshapes become more complicated due to electron-phonon coupling (EPC) which introduces an asymmetric Fano lineshape within the G-band.[33,34] This coupling is a consequence of the Kohn anomaly which occurs when a phonon can scatter an electron across the Fermi surface[52, 53]. This phenomenon occurs at $E_F = \pm\hbar\omega/2$, where $\hbar\omega$ is the phonon energy, since the joint density of states for the electronic transition becomes zero otherwise. Thus, due to finite density of states near $E_F=0$ for metallic nanotubes and graphene, both materials are prone to EPC. Metallic nanotubes exhibit this effect more-so because of quantization making the Fermi surface at most 2 points rather than a complete circle.[37] EPC causes a downshift and broadening of the phonons that are involved-- in metallic tubes these are LO G-band phonons due to quantization which limits conduction electrons to along the axis of the nanotube.[33, 34, 50, 52-55] The broadening is because of a decrease in phonon lifetime from this additional scattering process and is asymmetric toward lower energy as a result of the electronic continuum being smaller in energy than the discretized phonon.[34] The downshift is caused by energy renormalization due to dynamic electron-hole pair generation.[54, 55] An equivalent way of picturing this process is electron-hole pair creation by phonon decay which would be hindered if E_F occupies the final state of either carrier and, therefore, G-band lineshape is dependent on E_F. Because EPC causes G-band peak position and width to be doping dependent, this information can be used to determine doping concentration of metallic CNTs and graphene.[30, 56-58]

2.4.5 Radial Breathing Mode

The radial breathing mode, or “RBM”, is also a **Γ**-point phonon which is characteristic only of nanotubes because it corresponds to an in-phase bond stretch of atoms along the circumference of a nanotube. Due to the nature of this vibration, it is expected that the RBM frequency, ω_{RBM}, can be related to nanotube diameter, d_t, resulting in the relationship $\omega_{RBM}(cm^{-1})=248/d_t(nm)$ for single nanotubes on SiO_2 substrate (with minor adjustments otherwise)[33, 34] or $\omega_{RBM}(cm^{-1})=218/d_t(nm) + 16\ cm^{-1}$ for HiPCO samples.[59] In conjunction with the Kataura plot, it is possible to assign (n, m) indices to specific diameter nanotubes, and therefore RBMs, knowing the laser excitation energy used.[60] The Kataura plot gives the energy spacing of van Hove singularities (i.e. electronic sub-bands) for different diameter nanotubes. Because resonance occurs with electronic transitions between these singularities (unique to a given chirality), it is easy to identify chirality knowing the excitation energy used and RBM. Due to the strong exciton binding energies in carbon nanotubes (and low-dimensional materials in general) and strong electron-electron interactions, the original Kataura plot always underestimated the excitation energies and has since been corrected.[61]

2.5 Time-Resolved Incoherent Anti-Stokes Raman Spectroscopy

Very short optical pulses can be used to study phonon dynamics in crystalline solids. Stokes Raman signal is directly proportional to the number of phonons introduced into a material by Raman scattering. If an optical pulse of just femtoseconds were used to introduce these phonons into a solid, one can imagine probing the rate at which these phonons decay with another probe beam, but this would produce phonons in the system itself. Therefore, anti-Stokes signal is better suited for time-resolved phonon studies since its intensity is proportional to phonons that are already in the sample. Therefore, a pump pulse can be used to introduce phonons and a probe pulse can be used to detect the non-equilibrium phonon population at a controllable time delay between the pulses. Time-resolved incoherent anti-Stokes Raman spectroscopy (TRIARS) measures transient anti-Stokes Raman spectra at different delay times so phonon lifetimes can be determined.

Optical phonon (OP) lifetimes can, and indeed have been measured with static Raman spectroscopy linewidths, Γ, given the Heisenberg relationship $\Gamma=(\pi c T_2)^{-1}$, with T_2 being the overall lifetime.[62-66] However, T_2 consists of contributions from non-equilibrium phonon population extinction lifetime, T_1, as well as pure dephasing lifetime, τ_{ph}, expressed as $2/T_2=1/T_1+1/\tau_{ph}$.[67] In metals and semiconductors, electron-phonon coupling EPC can allow τ_{ph} to contribute significantly to T_2 which makes T_1, the actual lifetime of interest, ambiguous.[68] Therefore, directly measuring non-equilibrium OP populations with TRIARS is a more direct way to determine OP lifetimes.

A typical pump-probe apparatus for TRIARS measurements is shown in Figure 2.11.[69] A mode-locked Ti:sapphire laser with an 80 MHz repetition rate is used. Pump:probe power ratio is 3:2. Pump and probe beams are cross polarized (pump being perpendicular to the optics table) and focused with an objective lens. A central wavelength of 787 nm with a full width at half max of ~10 nm is the source. A 785 nm laserline filter is used for the probe beam and a 790 nm longpass filter for the pump such that any Raman signal from the pump does not interfere with that from the probe.[69] The Raman scattered light is collected in a spectrograph consisting of a diffraction grating and a thermoelectrically cooled CCD array.

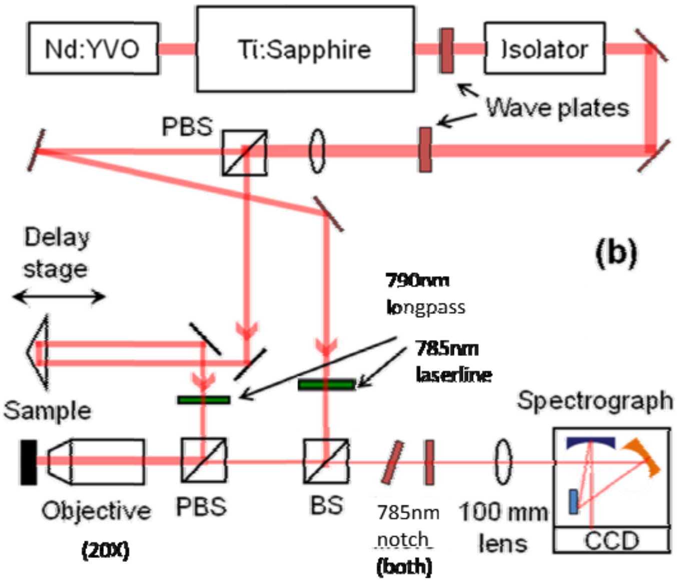

Figure 2.11. A common experimental setup for conducting pump-probe TRIARS measurements to determine OP lifetimes. Adapted from ref. [69] with slight modifications.

Due to the finite pulse widths of pump and probe beams in TRIARS measurements, the exponential decay of G-band phonon intensity, for example, must be convoluted with a "pump-probe correlation" (which is simply a Gaussian function) to give an overall function used for fitting TRIARS data:

$$\frac{I}{I_{max}} = \frac{1}{\sigma\sqrt{2\pi}} \exp\left[-\frac{(t-t_0)^2}{2\sigma^2}\right] \times [A\exp(-\frac{t}{T_1}) + B] \qquad \text{Eq. 2.1}$$

where I/I_{max} is the measured intensity normalized by the maximum intensity, σ is the pump-probe correlation value (related to the full width at half max), t is delay time of the probe, t_0 is the location of the Gaussian maximum, A and B are constants, and T_1 is the OP lifetime. Determination of σ is carried out by monitoring two-photon absorption with a GaP diode as the probe delay time is changed. An example fitting of TRIARS data for HiPCO carbon nanotubes is shown in Figure 2.12(a) which includes GaP diode response data used to obtain σ=0.32ps for this particular system. Actual TRIARS spectra taken at a few delay stage positions are shown in Figures 2.12(b) and 2.12(c) as an example also.

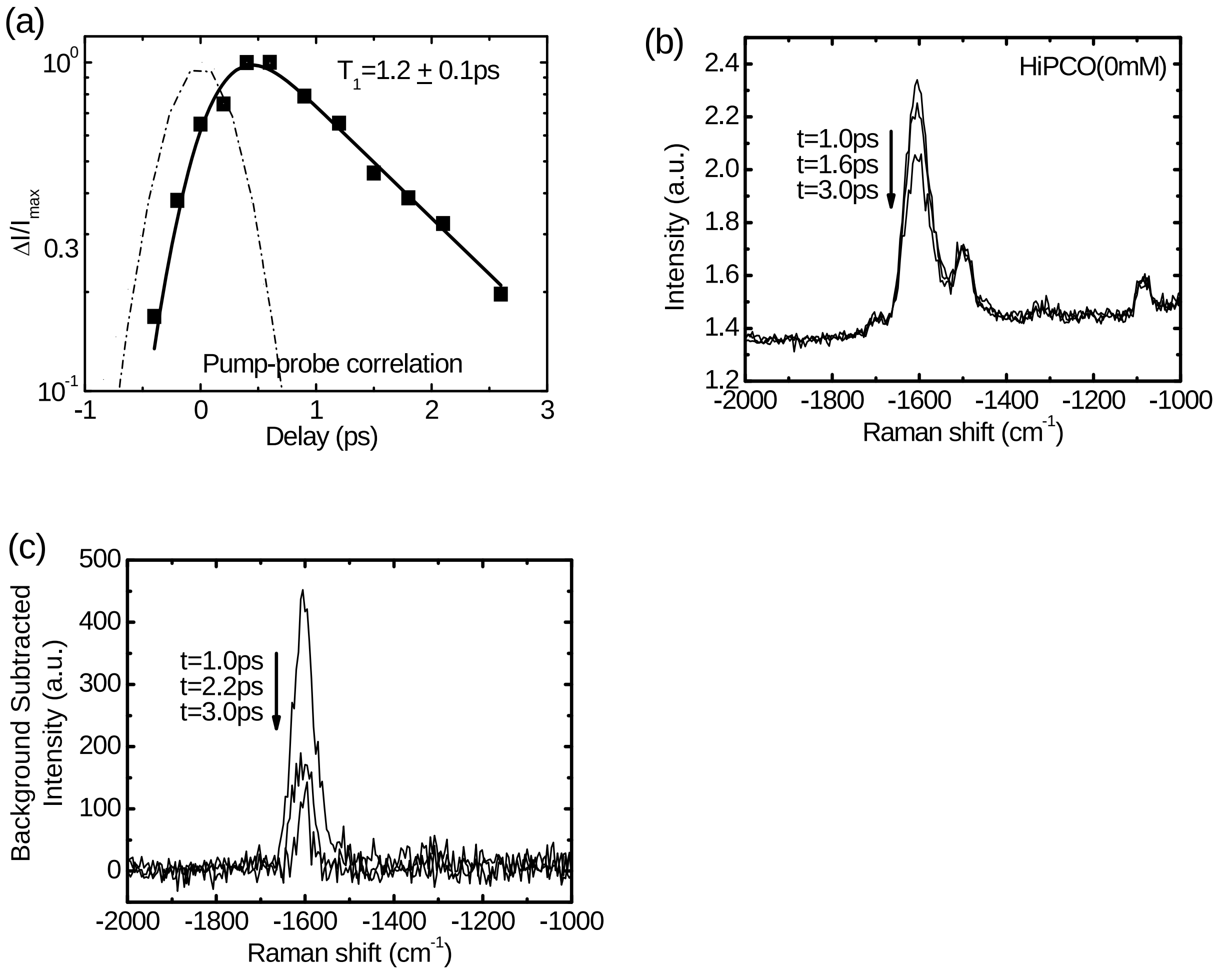

Figure 2.12. (a) Pump-probe correlation and example fitting of normalized TRIARS intensity (I/I_{max}) vs. probe delay for determining OP lifetime, T_1, using HiPCO nanotubes sample. (b) Example spectra showing raw data collected during TRIARS. (c) Spectra in (b) after background (t=-10ps) correction. 1.4 mW probe and 2.1 mW pump powers used.

2.6 References

[1] A. J. Van Bommel, J. E. Crombeen, and A. Van Tooren, Surf. Sci. **48**, 463 (1975).

[2] C. Berger *et al.*, Science **312**, 1191 (2006).

[3] Q. Yu, J. Lian, S. Siriponglert, H. Li, Y. P. Chen, and S. Pei, Appl. Phys. Lett. **93**, 113103 (2008).

[4] A. Reina, X. Jia, J. Ho, D. Nezich, H. Son, V. Bulovic, M. S. Dresselhaus, and J. Kong, Nano Lett. **9**, 30 (2009).

[5] X. Li *et al.*, Science **324**, 1312 (2009).

[6] K. S. Novoselov, D. Jiang, F. Schedin, T. J. Booth, V. V. Khotkevich, S. V. Morozov, and A. K. Geim, Proc. Natl. Acad. Sci. U.S.A. **102**, 10451 (2005).

[7] S. Roddaro, P. Pingue, V. Piazza, V. Pellegrini, and F. Beltram, Nano Lett. **7**, 2707 (2007).

[8] P. Blake, E. W. Hill, A. H. Castro Neto, K. S. Novoselov, D. Jiang, R. Yang, T. J. Booth, and A. K. Geim, Appl. Phys. Lett. **91**, 063124 (2007).

[9] H. Dai, Carbon Nanotubes, Springer, (Berlin, 2001).

[10] J. Kong, H. Soh, A. Cassell, C. F. Quate, and H. Dai, Nature **395**, 878 (1998).

[11] J. Hafner, M. Bronikowski, B. Azamian, P. Nikolaev, and D. Colbert, Chem. Phys. Lett. **296**, 195 (1998).

[12] B. Satishkumar, A. Govindaraj, R. Sen, and C. Rao, Chem. Phys. Lett. **293**, 47 (1998).

[13] P. Nikolaev *et al.*, Chem. Phys. Lett. **313**, 91 (1999).

[14] M. Su, B. Zheng, and J. Liu, Chem. Phys. Lett. **322**, 321 (2000).

[15] J.-F. Colomer *et al.*, Chem. Phys. Lett. **317**, 83 (2000).

[16] Y. Homma, Y. Kobayashi, T. Ogino, D. Takagi, R. Ito, Y. J. Jung, and P. M. Ajayan, J. Phys. Chem. B **107**, 12161 (2003).

[17] C. Kocabas, S.-H. Hur, A. Gaur, M. A. Meitl, M. Shim, and J. A. Rogers, Small **1**, 1110 (2005).

[18] C. Kocabas, S. J. Kang, T. Ozel, M. Shim, and J. A. Rogers, J. Phys. Chem. C **111**, 17879 (2007).

[19] N. Ishigami, H. Ago, K. Imamoto, M. Tsuji, K. Iakoubovskii, and N. Minami, J. Am. Chem. Soc. **130**, 9918 (2008).

[20] Q. Yu, G. Qin, H. Li, Z. Xia, Y. Nian, and S. S. Pei, J. Phys. Chem. B **110**, 22676 (2006).

[21] X. Liu, K. Ryu, A. Badmaev, S. Han, and C. Zhou, J. Phys. Chem. C **112**, 15929 (2008).

[22] P. Nikolaev, M. J. Bronikowski, R. K. Bradley, F. Rohmund, D. T. Colbert, K. A. Smith, and R. E. Smalley, Chem. Phys. Lett. **313**, 91 (1999).

[23] S. Noda, H. Sugime, T. Osawa, Y. Tsuji, S. Chiashi, Y. Murakami, and S. Maruyama, Carbon **44**, 1414 (2006).

[24] H. M. Christen, A. A. Puretzky, H. Cui, K. Belay, P. H. Fleming, D. B. Geohegan, and D. H. Lowndes, Nano Lett. **4**, 1939 (2004).

[25] S. Rosenblatt, Y. Yaish, J. Park, J. Gore, V. Sazonova, and P. L. McEuen, Nano Lett. **2**, 869 (2002).

[26] W. Kim, A. Javey, O. Vermesh, Q. Wang, Y. Li, and H. Dai, Nano Lett. **3**, 193 (2003).

[27] M. Radosavljevic, M. Freitag, K. V. Thadani, and A. T. Johnson, Nano Lett. **2**, 761 (2002).

[28] J. S. Lee, S. Ryu, K. Yoo, I. S. Choi, W. S. Yun, and J. Kim, J. Phys. Chem. C **111**, 12504 (2007).

[29] A. Gaur and M. Shim, Phys. Rev. B **78**, 125422 (2008).

[30] D. Abdula, T. Ozel, K. Kang, D. G. Cahill, and Moonsub Shim, J. Phys. Chem. C **112**, 20131 (2008).

[31] M. Shim, A. Javey, N. W. S. Kam, and H. Dai, J. Am. Chem. Soc. **123**, 11512 (2001).

[32] D. Abdula, and M. Shim, ACS Nano **2**, 2154 (2008).

[33] M. S. Dresselhaus, G. Dresselhaus, A. Jorio, A. G. Souza Filho, and R. Saito, Carbon **40**, 2043 (2002).

[34] M. S. Dresselhaus, G. Dresselhaus, R. Saito, and A. Jorio, Physics Reports **409**, 47 (2005).

[35] J. S. Bunch, A. M. van der Zande, S. S. Verbridge, I. W. Frank, D. M. Tanenbaum, J. M. Parpia, H. G. Craighead, and P. L. McEuen, Science **315**, 490 (2007).

[36] D. Graf, F. Molitor, K. Ensslin, C. Stampfer, A. Jungen, C. Hierold, and L. Wirtz, Nano Lett. **7**, 238 (2007).

[37] A. C. Ferrari, Solid State Commun. **143**, 47 (2007).

[38] A. C. Ferrari, J. C. Meyer, V. Scardaci, C. Casiraghi, M. Lazzeri, F. Mauri, S. Piscanec, D. Jiang, K. S. Novoselov, S. Roth, and A. K. Geim, Phys. Rev. Lett. **97**, 187401 (2006).

[39] R. P. Vidano, D. B. Fishbach, L. J. Willis, and T. M. Loehr, Solid State Commun. **39**, 341 (1981).

[40] I. Pocsik, M. Hundhausen, M. Koos, and L. Ley, J. Non-Cryst. Solids **227-230**, 1083 (1998).

[41] M. Ramsteiner, and J. Wagner, Appl. Phys. Lett. **51**, 1355 (1987).

[42] M. J. Matthews, M. A. Pimenta, G. Dresselhaus, M. S. Dresselhaus, and M. Endo, Phys. Rev. B **59**, R6585 (1999).

[43] C. Wang, Q. Cao, T. Ozel, A. Gaur, J. A. Rogers, and M. Shim, J. Am. Chem. Soc. **127**, 15437 (2005).

[44] J. L. Bahr, J. P. Yang, D. V. Kosynkin, M. J. Bronikowski, R. E. Smalley, and J. M. Tour, J. Am. Chem. Soc. **123**, 6536 (2001).

[45] M. Holzinger, J. Abraham, P. Whelan, R. Graupner, L. Ley, F. Hennrich, M. Kappes, and A. Hirsch, J. Am. Chem. Soc. **125**, 8566 (2003).

[46] J. M. Simmons, B. M. Nichols, S. E. Baker, M. S. Marcus, O. M. Castellini, C. S. Lee, R. J. Hamers, and M. A. Eriksson, J. Phys. Chem. B **110**, 7113 (2006).

[47] D. Abdula, K. T. Nguyen, and M. Shim, J. Phys. Chem. C **111**, 17755 (2007).

[48] A. Gupta, G. Chen, P. Joshi, S. Tadigadapa, and P. C. Eklund, Nano Lett. **6**, 2667 (2006).

[49] M. Shim, A. Gaur, K. T. Nguyen, D. Abdula, and T. Ozel, J. Phys. Chem. C **112**, 13017 (2008).

[50] L. M. Malard, M. A. Pimenta, G. Dresselhaus, and M. S. Dresselhaus, Physics Reports **473**, 51, (2009).

[51] T. M. G. Mohiuddin, A. Lombardo, R. R. Nair, A. Bonetti, G. Savini, R. Jalil, N. Bonini, D. M. Basko, C. Galiotis, N. Marzari, K. S. Novoselov, A. K. Geim, and A. C. Ferrari, Phys. Rev. B **79**, 205433 (2009).

[52] M. Lazzeri and F. Mauri, Phys. Rev. Lett. **97**, 266407 (2006).

[53] S. Piscanec, M. Lazzeri, J. Robertson, A. C. Ferrari, and F. Mauri, Phys. Rev. B **75**, 035427 (2007).

[54] J. Yan, Y. Zhang, P. Kim, and A. Pinczuk, Phys. Rev. Lett. **98**, 166802 (2007).

[55] A. H. Castro Neto and F. Guinea, Phys. Rev. B **75**, 045404 (2007).

[56] K. T. Nguyen, A. Gaur, and M. Shim, Phys. Rev. Lett. **98**, 145504 (2007).

[57] J. C. Tsang, M. Freitag, V. Perebeinos, J. Liu, and Ph. Avouris, Nat. Nanotechnol. **2**, 725 (2007).

[58] A. Das, A. K. Sood, A. Govindaraj, A. M. Saitta, M. Lazzeri, F. Mauri, and C. N. R. Rao, Phys. Rev. Lett. **99**, 136803 (2007).

[59] C. Fantini, A. Jorio, M. Souza, M. S. Strano, M. S. Dresselhaus, and M. A. Pimenta, Phys. Rev. Lett. **93**, 147406 (2004).

[60] A. Jorio, R. Saito, J. H. Hafner, C. M. Lieber, M. Hunter, T. McClure, G. Dresselhaus, and M. S. Dresselhaus, Phys. Rev. Lett. **86**, 1118 (2001).

[61] A. Jorio, C. Fantini, M. A. Pimenta, R. B. Capaz, Ge. G. Samsonidze, G. Dresselhaus, M. S. Dresselhaus, J. Jiang, N. Kobayashi, A. Gruneis, and R. Saito, Phys. Rev. B **71**, 075401 (2005).

[62] R. Cusco, E. Alarcon-Llado, J. Ibanez, L. Artus, J. Jimenez, B. Wang, and M. J. Callahan, Phys. Rev. B **75**, 165202 (2007).

[63] M. Millot, R. Tena-Zaera, V. Munoz-Sanjose, J. Broto, and J. Gonzalez, Appl. Phys. Lett. **96**, 152103 (2010).

[64] S. Anand, P. Verma, K. P. Jain, and S. C. Abbi, Physica B **226**, 331 (1996).

[65] Q. Zhao, H. Zhang, X. Xu, Z. Wang, J. Xu, and D. Yu, Appl. Phys. Lett. **86**, 193101 (2005).

[66] L. Bergman, D. Alexson, P. L. Murphy, R. J. Nemanich, M. Dutta, M. A. Stroscio, C. Balkas, H. Shin, and R. F. Davis, Phys. Rev. B **59**, 12977 (1999).

[67] S. F. Fischer, and A. Laubereau, Chem. Phys. Lett. **35**, 6 (1975).

[68] N. D. Fatti, F. Ganikhanov, P. Langot, R. Tommasi, and F. Vallee., J. Nonlinear Opt. Phys. Mater. **7**, 271 (1998).

[69] K. Kang, Y. K. Koh, C. Chiritescu, X. Zheng, and D. G. Cahill, Rev. Sci. Instrum. **79**, 114901 (2008).

CHAPTER 3

REACTION SELECTIVITY AND MODIFICATION OF VIBRATIONAL STRUCTURE WITH COVALENT SIDEWALL FUNCTIONALIZATION

This chapter characterizes changes in vibrational properties of sp^2-bonded carbon systems with introduction of defects. Covalent functionalization of carbon nanotubes is studied with static Raman spectroscopy. The results have implications on selective chemistry for improving carbon nanotube electronic devices. This work has been published in Ref. [1].

3.1 Introduction

An unprecedented combination of electrical and mechanical properties of single-walled carbon nanotubes (SWNTs)[2-4] makes them particularly appealing as high performance materials for developing areas such as flexible electronics[5] and nanoelectromechanical systems[6]. Electronic structure of SWNTs, as discussed in Chapter 1, leads to such properties as ON/OFF current ratios greater than 10^6, current densities up to 10^9A/cm^2, and hole mobilities reaching 100,000cm^2/Vs for these high-strength nanostructures.[7-10] In addition to next-generation electronics and electromechanical systems, technological advances in multiple areas from composites,[11-13] medicine delivery,[14] hydrogen storage[15, 16] to chemical/biological sensors[17-19] have also been envisioned exploiting unique properties of SWNTs. A key step in realizing most of these advances is the ability to chemically manipulate SWNTs. Whether intentional or unavoidable, covalent sidewall functionalization is a central issue in purification (in terms of removing amorphous and catalyst byproducts as well as separating metallic tubes from semiconducting ones) and in introducing desired functionalities such as chemical selectivity.

Raman spectroscopy is one of the most widely used techniques to characterize SWNTs, as discussed in Chapter 2.[20-22] From elucidating inherent properties[23] and aiding quality control[24] to monitoring chemical functionalization[25] and doping processes,[26-28] detailed insights have been gained from Raman studies. With respect to chemical functionalization, the increase in the intensity ratios of the disorder (D) and the G-band features (I_D/I_G ratio) has been commonly employed as an indication of covalent bond formation in SWNTs.[29-31] However, especially in metallic tubes, phenomena such as phonon softening via the Kohn anomaly[32-35] as well as the Fano lineshape[36-38] of the G-band complicate the situation. We have shown that metallic tubes undergo large changes in the G-band lineshape with Fermi level shift.[39] Furthermore, D-band intensities are usually significant even in non-functionalized metallic tubes. The D-band arises from a double resonance process where defect (disorder) scattering allows momentum conservation and is more likely in metallic tubes with finite density of states.[40, 41] Hence, using I_D/I_G ratio as an indication of the degree of covalent functionalization especially for metallic tubes needs to be carefully considered. Here, we utilize the reaction with 4-bromobenzene diazonium tetrafluoroborate (4-BBDT) as an example to explore how the Raman D- and G-band features of single metallic SWNTs are altered upon covalent bond formation. We first show Fermi level shift dependent D-band intensity and its implications on how the I_D/I_G ratio should be used in identifying covalent bond formation. The evolution of the Raman G- and D-band features of single metallic SWNTs upon reaction with 4-BBDT is then presented.

The particular system that we have chosen is also relevant to one of the biggest challenges in making progress towards new technologies exploiting unique properties of SWNTs. In most, if not all, prospects of integrating SWNTs into electronics, a major hurdle is the electronic inhomogeneity where a mixture of metallic and semiconducting tubes degrades performance and device-to-device uniformity. Covalent reaction with aryl diazonium salts is promising in separating metallic and semiconducting tubes due to its simplicity and relatively mild conditions.[42, 43] This approach has also been shown to be applicable directly to electrically contacted SWNTs for "on-chip" reactions where the electrical conductivity of metallic tubes can be chemically turned off.[25, 44, 45] However, the selectivity remains less than optimal due to a significant distribution of reactivity of SWNTs towards 4-BBDT. By examining Raman spectral evolution in single metallic tubes, insights on the origin of reactivity distribution may be gained.

3.2 Experimental Section

Patterned chemical vapor deposition was used to grow SWNTs on SiO_2/Si with ferritin catalyst and CH_4/H_2 feed gases following previously established methods, and as discussed in Chapter 2.[46] Substrates were pre-patterned with markers to be able to locate the same SWNTs at each step of the reaction. Functionalization was carried out with 4-BBDT (Aldrich) at concentrations of 1, 5, and 10 μM (consecutively) all in 10 mM KCl. The reaction was allowed to proceed for 10 minutes at each concentration. Raman spectra were collected on a Jobin Yvon LabRam HR 800 micro-Raman spectrometer with a 633 nm laser source using a 100x air objective. Up to ~3 mW laser intensity with spot diameter of ~1 μm has been used without any noticeable laser induced heating effects. Baseline correction was carried out by subtracting a spectrum collected a few μm away from where the nanotube was located. Simultaneous Raman and electrical measurements were carried out with SWNT devices operating with polymer electrolyte gate.[47, 48] Device fabrication and electrical characterization with top gating are described in Chapter 2.

3.3 Proper Defect Characterization through the D-band to G-band Ratio

The ratio of intensities of D and G bands in the Raman spectra has been often used as an indication of covalent functionalization of SWNTs as well as in identifying amorphous carbon contamination.[29-31] However, most metallic tubes exhibit significant D-band intensities even within the same sample where semiconducting tubes do not. This difference between metallic and semiconducting tubes arises from the fact that the D-band originates from a double resonance process, described in Chapter 2.[40, 41] In metallic tubes, there is a continuous finite density of states such that the elastic scattering event can be easily satisfied unlike in semiconducting tubes where there is a zero density of states within the band gap. Since this double resonance process is related to the G-band modes, the changes in the G-band lineshape can have a significant effect on the D-band intensities even without changes in the number of defect scattering sites.

Figures 3.1A and 3.1B show the D- and the G-band features of a single isolated metallic tube at the indicated electrochemical gate potential (V_g). The inset in Figure 3.1A shows the radial breathing mode of this metallic tube at 203 cm^{-1}. Consistent with our previous report,[39] broad asymmetric Fano lineshape of the G-band appears as the Fermi level passes through the band crossing point between the first pair of van Hove singularities (vHs) near $V_g = -0.1$ to -0.3 V (as indicated by the observed conductance minimum – not shown). Around this gate potential range, asymmetry of the Fano lineshape of the lowest frequency peak as well as broadening and softening of all G-band peaks are the most pronounced. Concurrently, there is a strong enhancement of the D-band peak intensity. The rationale for using I_D/I_G ratio as a measure of degree of functionalization is from the fact that the D-band arises from disorder scattering. Larger degree of disorder (i.e. from covalent functionalization) should lead to a more pronounced D-band. However, these changes in the Raman spectra with respect to the Fermi level shift question the validity of using I_D/I_G intensity ratio as a measure of degree of covalent functionalization of metallic tubes. While increasing the number of defects via covalent functionalization leading to enhanced D-band intensity should hold true in general, how the initial Fermi level shift dependent D-band intensity should be treated has not been considered but is a critical issue if D- and G-band features are to be used as any indication of covalent functionalization.

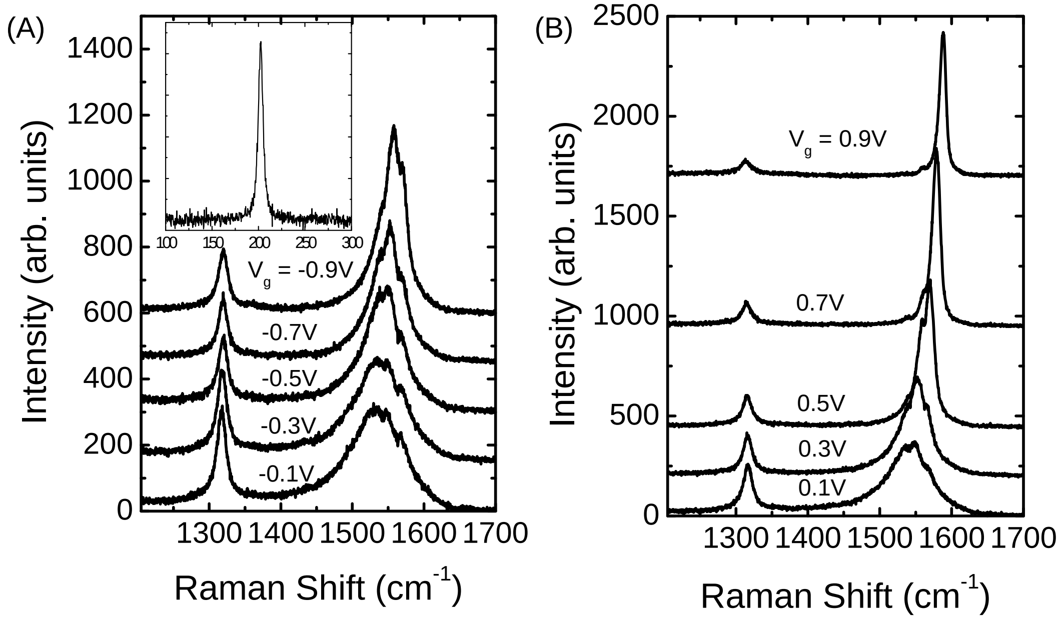

Figure 3.1. Fermi level dependent D- and G-band features in the Raman spectra of a single isolated metallic tube. Negative (A) and positive (B) gate potentials (V_g) were applied through a transparent polymer electrolyte thin film. Spectra are offset for clarity. At $V_g \sim -0.2$ V, there is a conductance minimum corresponding to the Fermi level being at half way between the first pair of vHs. The inset in (A) is the radial breathing mode of this metallic tube without external potential.

Figure 3.2A shows the I_D/I_G integrated intensity ratio where we have *not* considered the asymmetry of the lowest frequency G-band peak. The inset shows the corresponding integrated area under each band for the spectrum collected at V_g = 0V. There appears to be a large gate voltage dependence. When only the intensity maxima are used to compare I_D/I_G ratio, this apparent gate dependence becomes much more pronounced. If intensity maxima or integrated intensities neglecting the Fano lineshape of the G-band are used as an assessment of sidewall functionalization, the increase in the I_D/I_G ratio arising from the Fermi level shift can be easily misinterpreted as covalent bond formation.

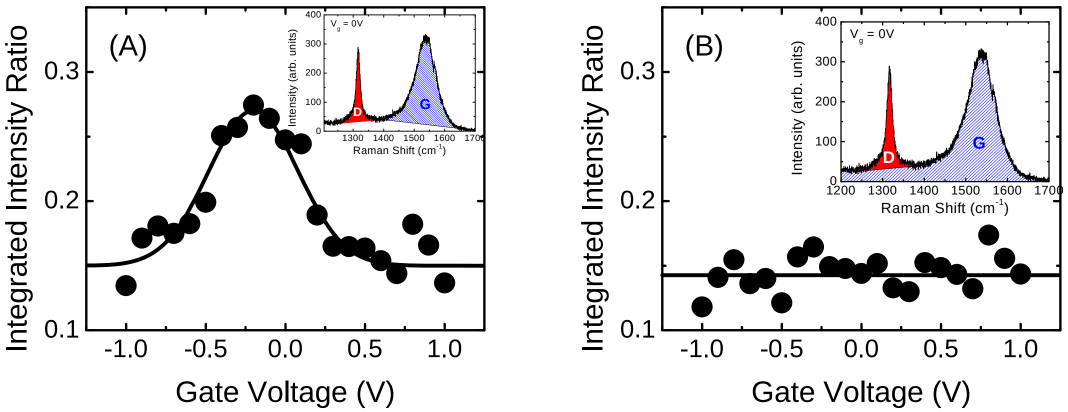

Figure 3.2. Gate voltage dependence of I_D/I_G integrated intensity ratios when the Fano lineshape is not considered (A) and when the asymmetric Fano lineshape is taken into account (B). Lines are guides to the eye. Insets show the corresponding integrated areas for the D (red) and G (blue) regions for the Raman spectrum collected at $V_g = 0V$.

Because the lineshape of the lowest frequency peak of the G-band features converts from Lorentzian to Fano lineshape as the Fermi level shifts from either one of the nearest vHs to the band crossing point, the integrated intensity of the G-band should include the lineshape asymmetry. Figure 3.2B shows the I_D/I_G integrated intensity ratio of the same metallic tube when the Fano lineshape is included as shown in the inset. In this case, the I_D/I_G ratio remains independent of the Fermi level shift. These results indicate the importance of taking Fano lineshape into account in interpreting G-band features of metallic tubes and strongly support the idea of the phonon-electronic continuum coupling being inherent to single isolated metallic tubes. More immediately, we can utilize I_D/I_G integrated intensity ratio as a qualitative measure of covalent functionalization of metallic tubes *only* if we include the Fano line area which extends below the D-band frequency range.

3.4 Spectral Changes with Covalent Functionalization

Keeping the Fano lineshape into account, the evolution of the Raman D- and G-bands of metallic tubes upon covalent sidewall functionalization is now discussed. Figure 3.3A shows the D- and the G-band features of a single metallic tube (RBM at 196 cm^{-1}) after reaction with the indicated concentrations of 4-BBDT. The results of curve fitting with a Lorentzian for the D-band and a Fano line and three Lorentzians for the G-band are also shown along with the data. Figure 3.3B shows the components from the curve fitting for the Raman spectrum prior to functionalization with 4-BBDT. The G-band features are labeled P1 through P4 with P1 being the Fano line given by $I(\omega) = I_o[1+q(\omega-\omega_o)/\Gamma]^2/\{1+[(\omega-\omega_o)/\Gamma]^2\}$, where ω_o is the Fano line spectral position with intensity I_o, q is the measure of phonon coupling to a continuum of states, and Γ is the width. This nanotube exhibits nearly all Lorentzian lineshapes for the G-band with the absolute value of q being relatively small ($|q| < 0.07$) which suggests that the Fermi level lies significantly away from the band crossing point between the first pair of vHs. The major change due to a relatively mild functionalization with 4-BBDT is the decrease in the intensity of the G-band while the D-band intensity remains nearly constant leading to increasing I_D/I_G ratio. Higher degree of functionalization leads to a decrease in the overall intensity including the D-band as shown later. Covalent sidewall functionalization should begin to perturb the electronic structure of the nanotube affecting the resonance condition with the incident light which may explain the decrease in the G-band intensity. The D-band intensity does not decrease proportionally to the G-band intensity since the covalent bonds formed should provide additional in-plane defects for disorder scattering. All D- and G-band modes exhibit noticeable linewidth increase (Figure 3.3D) but no obvious spectral shifts (Figure 3.3C) upon sidewall covalent functionalization.

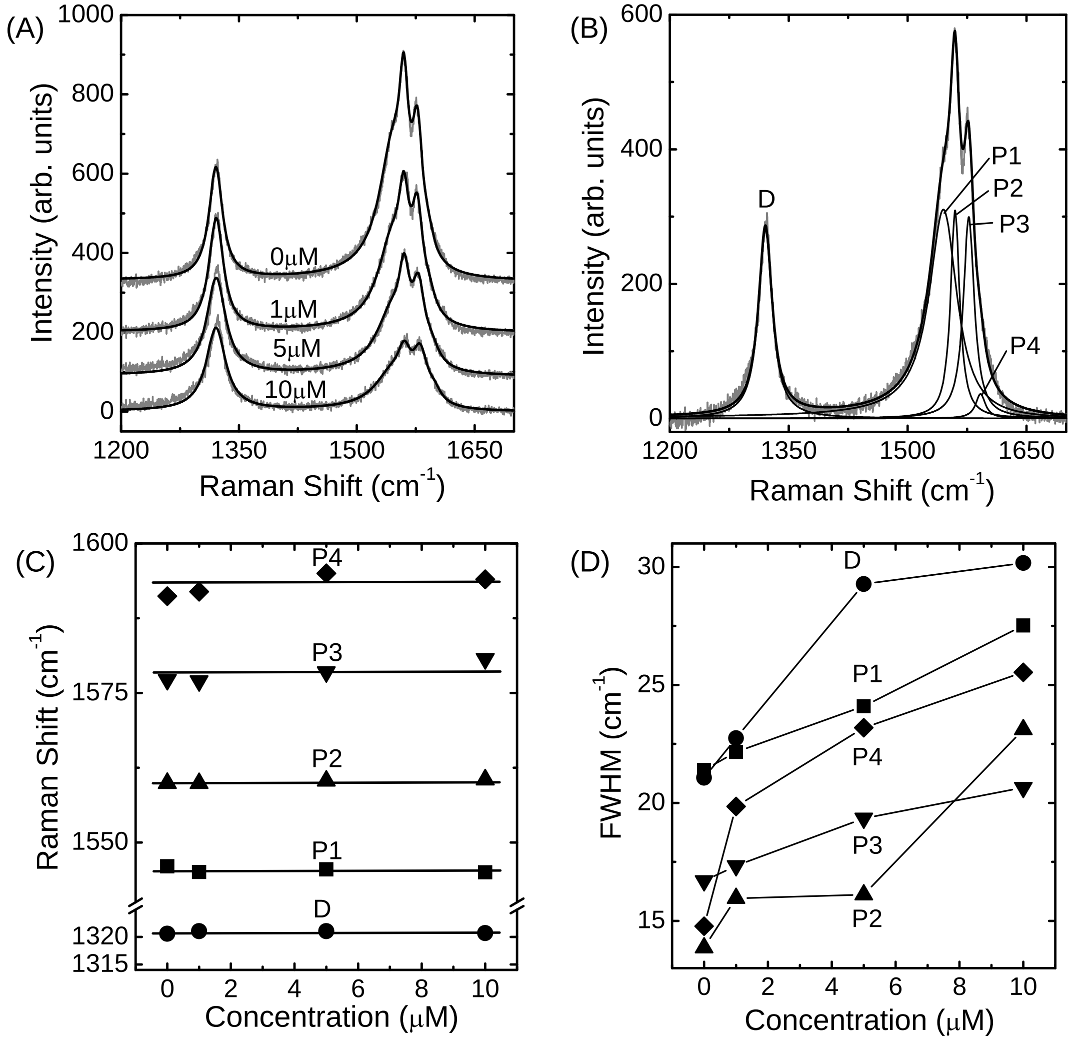

Figure 3.3. Changes in the disorder and G-band regions of a single metallic tube upon consecutive reaction with 1, 5, and 10 μM 4-BBDT (A). 0 μM corresponds to the spectrum prior to the reaction. The spectra are offset for clarity. Demonstration of curve fitting as described in the text for the Raman spectrum prior to reaction (B). Raman frequencies of each peak obtained from the curve fitting (C). No significant spectral shift is observed with increasing degree of functionalization with 4-BBDT. D- and G-band peak full width at half maximum (FWHM) evolution with increasing concentration of 4-BBDT (D). The width shown for P1, the Fano line, is Γ as defined in the text (Γ approaches HWHM as q → 0).

Metallic tubes with higher reactivity exhibit G-band spectral changes where the distinct peaks become nearly featureless. Figure 3.4 shows the Raman spectrum of another single metallic tube before and after the reaction with 1 and 10 μM 4-BBDT. The spectrum prior to reaction labeled “0 μM” is fitted including a Fano line for the G-band as described earlier. The spectrum after reaction with 1 μM 4-BBDT is also fitted in the same manner. This metallic tube exhibits a similar degree of functionalization at 1 μM as the metallic tube in Figure 3.3 at 10 μM (i.e. with respect to spectral changes). The spectrum after the reaction at 10 μM in Figure 3.4 is fitted with one Lorentzian for the D-band and two Lorentzians for the G-band. The choice of two Lorentzians for the G-band is for simplicity and minimizing the number of fitting parameters. While the reduction in the overall intensity after the reaction makes it difficult to conclude how exactly all G-band modes evolve, there is a distinct narrowing of the overall width from 1 μM to 10 μM reactions. The narrowing is due to the loss of the lowest frequency mode (i.e. the initial Fano component) as evident in the inset where the spectra are shown without the baseline offset. With a significant degree of covalent functionalization, metallic character of the nanotube may disappear leading to the loss of discrete phonon coupling to a continuum which initially gave rise to the Fano lineshape.

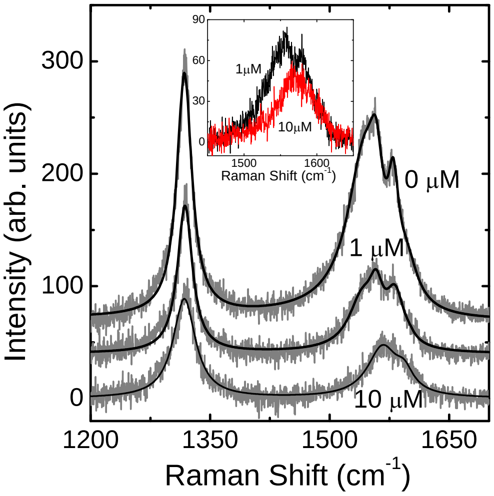

Figure 3.4. Changes in the Raman spectrum of a single metallic tube (RBM frequency = 190 cm^{-1}) that exhibits significantly large degree of fucntionalization after reaction with indicated concentrations of 4-BBDT. The "0 μM" spectrum corresponds to before functionalization. Spectra are fitted as described in the text. Inset is the G-band region without the baseline offset after reaction with the indicated concentration of 4-BBDT.

3.5 Reactivity Distribution of Metallic Carbon Nanotubes

We now consider the origin of the reactivity distribution in metallic SWNTs. Figure 3.5 shows the increase in the I_D/I_G ratios (taking the asymmetric Fano line into account) of several metallic tubes as they are reacted with increasing concentration of 4-BBDT. The reactivity as measured by I_D/I_G ratio increase exhibits a large distribution. While a reactivity distribution in semiconducting SWNTs will also contribute to the less than optimal electronic selectivity, there is an obvious contribution from the diverse response of metallic tubes. One possible contribution to the reactivity distribution is the size dependence. As the diameter decreases, the increasing curvature induced strain can render the sidewalls more reactive. However, the curvature effect is not expected to be significant until the diameter is less than about 1 nm.[49-51] The minimum diameter of the samples studied here based on the observed RBM frequency of 202 cm^{-1} is ~1.2

nm and therefore we anticipate the curvature effect to be inoperative here. Another size dependent phenomenon that may contribute is the diameter dependent density of states near the Fermi level. As the diameter decreases, the electronic density of states between the first pair of vHs is expected to increase[32, 36] and may influence the chemical reactivity of metallic tubes. Although the resonance conditions limit the range of diameters that can be observed with a fixed laser wavelength, there is no obvious trend with diameter. Whether or not there is a diameter dependent reactivity, extrinsic factors such as the initial degree of disorder may be a larger contributing factor.

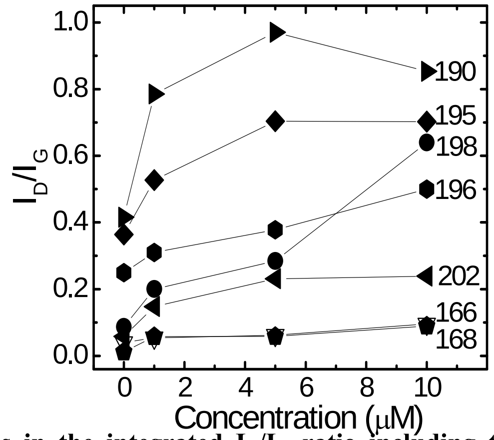

Figure 3.5. The changes in the integrated I_D/I_G ratio including the Fano line contribution of metallic tubes upon reaction with increasing 4-BBDT concentration. Each symbol type corresponds to the same nanotube. RBM frequencies (in cm^{-1}) are indicated to the right of the data points. We tentatively assign the two nanotubes with RBM at 166 and 168 cm^{-1} as metallic tubes based on the presence of asymmetric Fano lineshape of the G-band.

Since SWNTs are composed of all atoms at the surface, extrinsic factors can often have a pronounced influence on the observed properties. The degree of disorder prior to chemical functionalization can be considered as one of the measures of contributions from extrinsic factors. The initial I_D/I_G ratio (with Fano lineshape taken into account) varies by about half an order of magnitude for the seven tubes shown in Figure 3.5. Assuming that an existing disorder in the SWNT π-network will enhance the reactivity of nearby C atoms, we expect larger initial I_D/I_G ratio to lead to larger degree of functionalization. This idea of enhanced reactivity around or near an existing disorder or defect is consistent with previous theoretical and experimental studies.[52, 53] Figure 3.6 plots the change in I_D/I_G ratio as a function of the initial I_D/I_G ratio upon reaction with 5 μM 4-BBDT. There is a strong dependence with larger initial I_D/I_G ratio leading to enhanced reactivity.

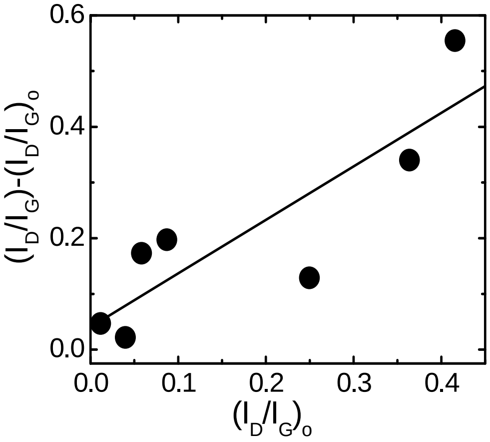

Figure 3.6. Correlation between the change in I_D/I_G ratio upon reaction with 5 μM 4BBDT and the initial I_D/I_G ratio, $(I_D/I_G)_o$. The same metallic tubes as in Figure 1.5 are shown.

In developing electronically selective covalent chemistry to separate metallic from semiconducting tubes, this dependence on the initial degree of disorder cannot be overlooked. For bulk reactions in solutions, such an effect may be even more pronounced due to additional processing conditions such as high shear mixing, ultrasonication, and/or strong acid treatments required to suspend SWNTs into solution. The varying degree of success of reaction with aryl diazonium salts in improving performance of transistors consisting of multiple SWNTs as active elements may, at least in part, be explained by the large variations in the initial degree of disorder. While further studies are needed, this initial disorder dependent reactivity suggests that “pristine” metallic tubes may not be as reactive towards 4-BBDT, perhaps to the point where their reactivity may be comparable to semiconducting tubes. At the very least, the possibility of selective interaction of metallic tubes to ambient surroundings which induces the initial in-plane disorder prior to covalent functionalization contributing to the observed electronic selectivity need to be considered.

3.6 Conclusions

We have examined how the Raman spectra of metallic tubes evolve with covalent sidewall functionalization. Often employed I_D/I_G intensity ratio as an indication of covalent functionalization (as well as an indication of degree of contamination from amorphous carbon) needs to take into account the asymmetric Fano lineshape of the lowest frequency G-band peak. Otherwise, the apparent increase in the D-band intensity due to Fermi level shift may be misinterpreted as covalent bond formation. Relatively mild covalent sidewall functionalization of metallic tubes leads to increasing integrated I_D/I_G ratio including the Fano component and all G- and D-band mode broaden. At higher degree of functionalization, the Fano component disappears. We have also shown a large dependence of metallic tube reactivity on the initial degree of disorder. This effect has important implications on covalent chemistry for functionalizing SWNTs. The varying degree of initial disorder in metallic tubes is a major contribution to the reactivity distribution observed here. Whether it is the reaction with aryl diazonium salts or any other covalent chemistry, the enhanced reactivity due to the pre-existing disorder needs to be carefully considered when developing and analyzing techniques to separate out metallic tubes from semiconducting ones.

3.7 References

[1] Abdula, D.; Nguyen, K. T.; Shim, M., *J. Phys. Chem. C* **2007**, *111,* 17755.

[2] Yaish, Y.; Park, J. Y.; Rosenblatt, S.; Sazonova, V.; Brink, M.; McEuen, P. L., *Phys. Rev. Lett.* **2004,** *92*, 046401.

[3] Javey, A.; Guo, J.; Wang, Q.; Lundstrom, M.; Dai, H., *Nature* **2003**, *424*, 654.

[4] Yu, M.-F.; Files, B. S.; Arepalli, S.; Ruoff, R. S., *Phys. Rev. Lett.* **2000**, *84*, 5552.

[5] Cao, Q.; Zhu, Z. T.; Lemaitre, M. G.; Xia, M. G.; Shim, M.; Rogers, J. A., *Appl. Phys. Lett.* **2006,** *88*, 113511.

[6] Cao, Q.; Zhu, Z. T.; Lemaitre, M. G.; Xia, M. G.; Shim, M.; Rogers, J. A., *Appl. Phys. Lett.* **2006,** *88*, 113511.

[7] Javey, A.; Kim, H.; Brink, M.; Wang, Q.; Ural, A.; Guo, J.; McIntyre, P.; McEuen, P.; Lundstrom, M.; Dai, H., *Nature Mater.* **2002**, *1*, 241.

[8] Yao, Z.; Kane, C. L.; Dekker, C. *Phys. Rev. Lett.* **2000**, *84*, 2941.

[9] Fuhrer, M. S.; Kim, B. M.; Durkop, T.; Brintlinger, T. *Nano Lett*. **2002**, 2, 755.

[10] Baughman, R. H.; Zakhidov, A. A.; de Heer, W. A., *Science* **2002,** *297*, 787.

[11] Wise, K. E.; Park, C.; Siochi, E. J.; Harrison, J. S., *Chem. Phys. Lett.* **2004,** *391*, 207.

[12] Huxtable, S. T.; Cahill, D. G.; Shenogin, S.; Xue, L. P.; Ozisik, R.; Barone, P.; Usrey, M.; Strano, M. S.; Siddons, G.; Shim, M.; Keblinski, P., *Nature Mater.* **2003,** *2*, 731.

[13] Ajayan, P. M.; Stephan, O.; Colliex, C.; Trauth, D., *Science* **1994,** *265*, 1212.

[14] Kam, N. W. S.; O'Connell, M.; Wisdom, J. A.; Dai, H. J., *Proc. Nat. Acad. Sci.* **2005,** *102*, 11600.

[15] Liu, C.; Fan, Y. Y.; Liu, M.; Cong, H. T.; Cheng, H. M.; Dresselhaus, M. S., *Science* **1999,** *286*, 1127.

[16] Dillon, A. C.; Jones, K. M.; Bekkedahl, T. A.; Kiang, C. H.; Bethune, D. S.; Heben, M. J., *Nature* **1997,** *386*, 377.

[17] Chen, X.; Tam, U. C.; Czlapinski, J. L.; Lee, G. S.; Rabuka, D.; Zettl, A.; Bertozzi, C. R., *J. Am. Chem. Soc.* **2006**, *128*, 6292.

[18] Chen, R. J.; Bangsaruntip, S.; Drouvalakis, K. A.; Kam, N. W. S.; Shim, M.; Li, Y. M.; Kim, W.; Utz, P. J.; Dai, H. J., *Proc. Nat. Acad. Sci.* **2003,** *100*, 4984.

[19] Song, C. H.; Pehrsson, P. E.; Zhao, W., *J. Phys. Chem. B* **2005,** *109*, 21634.

[20] Dresselhaus, M. S.; Eklund, P. C., *Adv. Phys.* **2000,** *49*, 705.

[21] Rao, A. M.; Chen, J.; Richter, E.; Schlecht, U.; Eklund, P. C.; Haddon, R. C.; Venkateswaran, U. D.; Kwon, Y.-K.; Tomanek, D. *Phys. Rev. Lett.* **2001**, *86*, 3895.

[22] Strano, M. S.; Doorn, S. K.; Haroz, E. H.; Kittrell, C.; Hauge, R. H.; Smalley, R. E., *Nano Lett.* **2003,** *3*, 1091.

[23] Rao, A. M.; Richter, E.; Bandow, S.; Chase, B.; Eklund, P. C.; Williams, K. A.; Fang, S.; Subbaswamy, K. R.; Menon, M.; Thess, A.; Smalley, R. E.; Dresselhaus, G.; Dresselhaus, M. S., *Science* **1997,** *275*, 187.

[24] Kim, U. J.; Furtado, C. A.; Liu, X. M.; Chen, G. G.; Eklund, P. C., *J. Am. Chem. Soc.* **2005,** *127*, 15437.

[25] Wang, C.; Cao, Q.; Ozel, T.; Gaur, A.; Rogers, J. A.; Shim, M. *J. Am. Chem. Soc.* **2005**, *127*, 11460.

[26] Shim, M.; Ozel, T.; Gaur, A.; Wang, C. J., *J. Am. Chem. Soc.* **2006,** *128*, 7522.

[27] Rao, A. M.; Eklund, P. C.; Bandow, S.; Thess, A.; Smalley, R. E. *Nature* **1997**, *388*, 257.

[28] Chen, G.; Furtado, C. A.; Kim, U. J.; Eklund, P. C. *Phys. Rev. B* **2005**, *72*, 155406.

[29] Bahr, J. L.; Yang, J. P.; Kosynkin, D. V.; Bronikowski, M. J.; Smalley, R. E.; Tour, J. M., *J. Am. Chem. Soc.* **2001,** *123*, 6536.

[30] Holzinger, M.; Abraham, J.; Whelan, P.; Graupner, R.; Ley, L.; Hennrich, F.; Kappes, M.; Hirsch, A., *J. Am. Chem. Soc.* **2003,** *125*, 8566.

[31] Simmons, J. M.; Nichols, B. M.; Baker, S. E.; Marcus, M. S.; Castellini, O. M.; Lee, C. S.; Hamers, R. J.; Eriksson, M. A., *Journal of Physical Chemistry B* **2006,** *110*, 7113.

[32] Dubay, O.; Kresse, G.; Kuzmany, H., *Phys. Rev. Lett.* **2002,** *88*, 235506.

[33] Lazzeri, M.; Piscanec, S.; Mauri, F.; Ferrari, A. C.; Robertson, J., *Phys. Rev. B* **2006,** *73*, 155426.

[34] Popov, V. N.; Lambin, P., *Phys. Rev. B* **2006,** *73*, 085407.

[35] Rafailov, P. M.; Maultzsch, J.; Thomsen, C.; Kataura, H., *Phys. Rev. B* **2005,** *72*, 045411.

[36] Brown, S. D. M.; Jorio, A.; Corio, P.; Dresselhaus, M. S.; Dresselhaus, G.; Saito, R.; Kneipp, K., *Phys. Rev. B* **2001,** *63*, 155414.

[37] Jiang, C.; Kempa, K.; Zhao, J.; Schlecht, U.; Kolb, U.; Basché, T.; Burghard, M.; Mews, A., *Phys. Rev. B* **2002,** *66*, 161404.

[38] Paillet, M.; Poncharal, P.; Zahab, A.; Sauvajol, J.-L.; Meyer, J. C.; Roth, S., *Phys. Rev. Lett.* **2005,** *94*, 237401-4.

[39] Nguyen, K. T.; Gaur, A.; Shim, M., *Phys. Rev. Lett*. **2007**, *98*, 145504.

[40] Maultzsch, J.; Reich, S.; Thomsen, C., *Phys. Rev. B* **2001,** *64,* 121407.

[41] Zolyomi, V.; Kurti, J.; Gruneis, A.; Kuzmany, H., *Phys. Rev. Lett.* **2003,** *90,* 157401.

[42] Strano, M. S.; Dyke, C. A.; Usrey, M. L.; Barone, P. W.; Allen, M. J.; Shan, H.; Kittrell, C.; Hauge, R. H.; Tour, J. M.; Smalley, R. E. *Science* **2003**, *301*, 1519.

[43] Usrey, M. L.; Lippmann, E. S.; Strano, M. S., *J. Am. Chem. Soc.* **2005,** *127*, 16129.

[44] Balasubramanian, K.; Sordan, R.; Burghard, M.; Kern, K. *Nano Lett.* **2004**, *4*, 827.

[45] An, L.; Fu, Q.; Lu, C.; Liu, J. *J. Am. Chem. Soc.* **2004**, *126*, 10520.

[46] Kong, J.; Soh, H. T.; Cassell, A. M.; Quate, C. F.; Dai, H. *Nature* **1998**, *395*, 878.

[47] Siddons, G. P.; Merchin, D.; Back, J. H.; Jeong, J. K.; Shim, M. *Nano Lett.* **2004**, *4*, 927.

[48] Ozel, T.; Gaur, A.; Rogers, J. A.; Shim, M. *Nano Lett.* **2005**, *5*, 905.

[49] Niyogi, S.; Hamon, M. A.; Hu, H.; Zhao, B.; Bhowmik, P.; Sen, R.; Itkis, M. E.; Haddon, R. C., *Acc. Chem. Res.* **2002,** *35*, 1105.

[50] Zhou, W.; Ooi, Y. H.; Russo, R.; Papanek, P.; Luzzi, D. E.; Fischer, J. E.; Bronikowski, M. J.; Willis, P. A.; Smalley, R. E., *Chem. Phys. Lett.* **2001,** *350*, 6.

[51] Zhang, Y. F.; Liu, Z. F., *J. Phys. Chem. B* **2004,** *108*, 11435.

[52] Wang, C.; Zhou, G.; Wu, J.; Gu, B. – L.; Duan, W., *Appl. Phys. Lett.* **2006**, *89*, 173130.

[53] Fan, Y.; Goldsmith, B. R.; Collins, P. G., *Nature Mater.* **2005,** *4*, 906.

CHAPTER 4

INFLUENCE OF COVALENT SIDEWALL FUNCTIONALIZATION AND DOPING ON OPTICAL PHONON DYNAMICS

In this chapter, the role that defects and doping have on metallic and semiconducting carbon nanotube G-band optical phonons are considered using time-resolved incoherent anti-Stokes Raman spectroscopy. Phonon mediated electron scattering is especially strong in nanotubes making optical phonon decay of interest for device applications. Optical phonon decay also has implications on device thermal management.

4.1 Introduction

Implementation of carbon nanotubes into micro- and nano-electronics has shown promise[1-5] with realistic performance limits now beginning to be established.[6] In the high-bias regime, current in nanotubes can be limited by carrier scattering with optical phonons (OPs).[7-10] In graphite, over 90% of the energy of photoexcited hot carriers are estimated to dissipate via OPs[11] and similar carrier relaxation pathways are expected in carbon nanotubes. Hence, monitoring non-equilibrium OP population dynamics can provide insights important for carbon nanotube-based electronic and optoelectronic devices. Dynamics of OPs may be affected by doping, nanotube type (metallic or semiconducting), and defects. Electron-phonon coupling (EPC) is in general important in how carriers relax and may also be an important factor in OP decay.[12] In carbon nanotubes, EPC leads to large differences in the G-band linewidths of metallic and semiconducting nanotubes. Metallic carbon nanotubes exhibit broadened and softened lower frequency G-band mode (LO mode) due to presence of a Kohn anomaly near the Dirac point.[13, 14] Doping via electrostatic gate potential or charge transfer, without introducing impurities within the lattice, has been shown to vary this width.[15-17] Therefore, doping and metallic versus semiconducting character may be expected to cause changes in OP dynamics. However, similar or only slightly different OP population lifetimes of G-band phonons in metallic and semiconducting nanotubes have been measured.[18]

Defects are also important to consider in OP dynamics since lattice imperfections break crystal translational symmetry and relax momentum conservation requirement.[19-21] How defects alter OP dynamics has been investigated in crystalline materials, including Bi, III-V and II-VI compound semiconductors, and graphite.[12, 20-27] One consequence of defects on OPs can be a change in the Raman linewidth. In carbon nanotubes, specifically in metallic nanotubes, introduction of defects/disorder leads to removal of line broadening due to the presence of Kohn anomaly which counteracts line broadening by defects.[28] Defect induced broadening of Raman G-band can be observed in semiconducting nanotubes as well as in metallic nanotubes that have their Fermi level shifted away from the Dirac point.[29] The spectral linewidth (the full-width-at-half-maximum, Γ) is, however, related to the overall dephasing time T_2 by $\Gamma = (\pi c T_2)^{-1}$ and T_2 consists of contributions from non-equilibrium phonon population extinction, T_1, as well as pure dephasing, τ_{ph}, expressed as $2/T_2 = 1/T_1+1/\tau_{ph}$.[30]

Time-resolved incoherent anti-Stokes Raman scattering (TRIARS) measurements have recently been used to directly measure T_1 of G-band OPs. While the measured T_1 value 1.2 ps (or lifetime broadening of 4.4 cm^{-1})[18, 31, 32] is compatible with typically reported single nanotube linewidth Γ of ~ 6 – 12 cm^{-1},[33] the larger Γ from static Raman spectra suggest possible additional pure dephasing process or inhomogenous broadening to be present even in single nanotube measurements.[32] However, relatively high energy pump beam used in TRIARS, which places the system under investigation far from equilibrium, may lead to OP lifetimes that may be different than what may be deduced from linewidths measured near equilibrium situations.[11] Time-resolved coherent anti-Stokes Raman scattering (TRCARS) studies have also been carried out to measure T_2 but seemingly conflicting results with respect to how extrinsic factors affect overall OP dephasing in carbon nanotubes have been reported.[31, 34] For single-walled carbon nanotube films on glass, one study has reported $T_2/2 = 1.1 \pm 0.1$ ps in two samples with a large difference in D-band intensities suggesting defects to have negligible effects.[34] However, a more recent study using a combination of TRCARS and TRIARS has shown that much smaller perturbations in the form of non-covalent interactions between nanotubes can significantly alter $T_2/2$ (while T_1 remains unaffected).[31] Ensemble samples containing both metallic and semiconducting nanotubes may cause additional complications. Therefore, a systematic study that sorts out effects of doping, defects, and nanotube type is necessary to elucidate OP dynamics.

In this work, we examine how G-band OP liftetime and Raman linewidth in carbon nanotubes are affected by varying doping, metallic vs. semiconducting character, and defect density. OP lifetimes are measured by TRIARS and compared to linewidth of individual nanotubes. Degree of doping is controlled either by electrostatic gate potential in the case of single nanotubes or by molecular adsorption that leads to charge transfer for thin films of nanotubes. Defect density, or the degree of disorder, is varied by annealing and covalent functionalization. A comparison between samples exhibiting high metallic and predominantly semiconducting contributions to the Raman signal is also carried out.

4.2 Experimental Details

Samples were made from either carbon nanotubes prepared by high pressure carbon monoxide (HiPCO) process (Carbon Nanotechnologies Inc.) or by arc-discharge (CarboLex

Inc.). Approximately 2 mg of both starting materials separately were first acid treated by sonication in 20 mL of 8 M HNO_3 for 1 h at 50 ^{o}C, centrifuged, washed with deionized water, centrifuged again and finally dispersed in ethanol by sonicating for 1 h at room temperature. For arc-discharge nanotubes, which exhibit a significant D-band before and after the acid treatment, different annealing steps were taken to vary the degree of disorder. HiPCO nanotubes exhibit relatively small D-band and therefore the defect concentration was varied by covalent functionalization.

After the acid treatment, arc-discharge nanotubes were spin coated onto SiO_2/Si substrates with markers (300 nm oxide, markers are areas of oxide patterned and etched with reactive-ion etching prior to nanotube deposition) from the ethanol suspension. The sample where no further processing was carried out after this step is referred to as "Arc(As Prep.)". The sample that was annealed at 400 ^{o}C for 1 h under 500 cm^3/min flow of Ar after deposition on substrate is termed "Arc(Ar)". In order to further reduce defect concentration, another sample was heated to 350 ^{o}C in air then cooled to room temperature upon reaching 350 ^{o}C. This sample is called "Arc(Air)".

HiPCO nanotube samples were covalently functionalized by mixing acid-treated tubes suspended in ethanol (~0.1 mg/mL) with 20 mM, 100 mM, or 200 mM aqueous solution of 4-nitrobenzene diazonium tetrafluoroborate (4-NBDT, Fluka) in 1:1 volume ratio; sonicating for 1 min; allowing the reaction to go on for 20 min; centrifuging and rinsing the nanotubes with deionized water; centrifuging and re-suspending them in ethanol. These suspensions were then used to spin coat nanotubes onto markered substrates. These samples are labeled "HiPCO(10 mM)", "HiPCO(50 mM)", and "HiPCO(100 mM)" according to the concentration of 4-NBDT after mixing nanotube and functionalizing solutions. A fourth sample, "HiPCO(0 mM)", was made in the same manner, but distilled water without 4-NBDT was used to make the 1:1 reaction mixtures. After OP lifetime measurements were carried out, these four samples were exposed to high molecular weight poly(ethylenimine) (PEI, Sigma) for doping purposes. Neat PEI was spin coated on the samples and allowed to adsorb for 1 h, then thoroughly rinsed with distilled water to remove excess PEI. Samples doped as such are noted along with the concentration of 4-NBDT they were functionalized with previously [e.g., "HiPCO(100 mM/PEI)"]. Finally, a last sample of non-functionalized HiPCO nanotubes on-substrate [prepared in the same manner as HiPCO(0 mM)] was annealed at 400 °C for 1 h under 500 cm^3/min flow of Ar and is called "HiPCO(Ar)".

The above arc-discharge and HiPCO samples of ensemble/bundles of nanotubes are collectively referred to as "thin film samples." For single nanotube and device measurements, carbon nanotubes were grown directly on Si/SiO_2 substrates by chemical vapor deposition using ferritin catalyst and CH_4/H_2 following Ref. 16. Electrical contacts to individual carbon nanotubes were made by patterning 35 nm thick Au electrodes with 5 nm Ti wetting layer on top of the nanotubes. Electrochemical gate potential was applied to these contacted nanotube devices using a 20 wt% $LiClO_4 \cdot H_2O$ in PEI solution.

Static Raman spectroscopy was carried out on a Jobin Yvon LabRam HR 800 micro-Raman spectrometer with a 785 nm laser excitation source (75 W/cm^2 intensity unless otherwise noted) and a 50X air objective providing a spot size with a $1/e^2$ radius of 1.5 μm. A mode-locked Ti:sapphire laser with an 80 MHz repetition rate was used for TRIARS measurements.[18, 35] Total laser fluence was 58.3 $\mu J/cm^2$ (unless otherwise noted) and the pump:probe power ratio was kept at 3:2. Pump and probe beams were cross polarized and focused with a 20X air objective to a spot size with a $1/e^2$ radius of 3.75 μm. A central wavelength of 787 nm with a full-width-at-half-maximum of ~10 nm was used. A 785 nm laser line filter was used for the probe beam and a 790 nm long-pass filter was used for the pump to prevent Raman signal from the pump interfering with that from the probe.[36] The Raman scattered light was collected in a spectrograph consisting of a diffraction grating and a thermoelectrically cooled CCD array. The OP population lifetimes are obtained by fitting the data collected to a convolution of the pump-probe correlation with a response function of abrupt rise followed by an exponential decay. Pump-probe correlation is measured by two-photon absorption in a GaP detector as described in Ref. 36.

4.3 Processing Effects on Doping, Metallic/Semiconducting Character, and Defects

Static Raman spectroscopy is a useful tool to determine relative degree of doping, metallic/semiconducting character, and defect concentration of each sample type. Relative defect concentration can be estimated using a ratio of integrated area of the D-band to that of the G-band (A_D/A_G).[29] The relative degree of doping can be inferred from shifts in the D-band. The G-band shifts symmetrically (or nearly symmetrically) with respect to carrier concentration and cannot be used to distinguish p- or n-doping.[15-17] The D-band, on the other hand, shows a monotonic decrease in frequency from p-type to n-type[37] and is therefore used here to determine relative doping levels. Note that, throughout this paper, we refer to doping specifically as increasing the number of carriers, either by charge transfer or by electrostatic gating, without the introduction of impurities and therefore defects/disorder into the lattice. Raman peak frequencies and A_D/A_G ratios are acquired by fitting the obtained Raman spectra, examples of which are shown in Figure 4.1. HiPCO samples are fitted with one Lorentzian for the D-band and two Lorentzians for the G-band. This G-band lineshape combined with RBM frequencies observed indicates that predominantly semiconducting nanotubes contribute to the Raman spectra of HiPCO tubes at the laser energy of 1.58 eV (785 nm) used here. Spectra of arc-discharge samples are fitted with one Lorentzian for the D-band and two Lorentzians and a Fano line (horizontal hatches) for the G-band to account for EPC effects in metallic nanotubes.[16] Based on the ratio of integrated intensities of the Fano line and the total G-band, A_{Fano}/A_G, for all arc-discharge nanotube samples, we estimate metallic tube contribution to the Raman signal to be about 35%. This value does not change with the degree of disorder as shown in Figure 4.1(b).

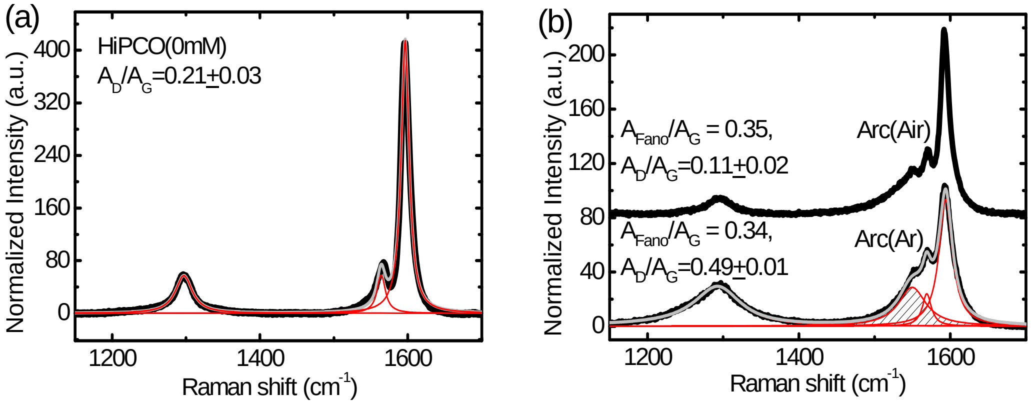

Figure 4.1. Raman spectra of non-functionalized HiPCO nanotubes, "HiPCO(0 mM)" (a), and argon and air annealed arc-discharge samples, "Arc(Ar)" and "Arc(Air)", respectively (b), along with examples of curve fitting. Grey lines are the curve fitting results and the red curves are the components of the fit. Ratios of the Fano peak (shaded red) integrated intensity to that of the G-band (A_{Fano}/A_G) for characterizing metallic nanotube content and relative disorder (A_D/A_G) for arc-discharge nanotubes are also noted. Spectra in (b) are offset for clarity.

The degree of doping, on the other hand, does change with disorder induced by covalent functionalization with 4-NBDT. HiPCO samples show that functionalization with 4-NBDT leads to p-type doping as inferred from the D-band frequency up-shift[37] along with increasing A_D/A_G, as quantified in Figure 4.2. Because of the concurrent doping and defect density increase, PEI is used as a "counter-dopant" to separate out the two effects. PEI adsorption does not change A_D/A_G.[38] Note, however, that annealing in Ar decreases the defect concentration. For arc-discharge nanotubes, which start with a higher degree of defects, different annealing processes are carried out to vary defect concentration. Annealing causes only minor changes in the degree of doping (D-band frequency change of 2 cm^{-1} or less). Both annealing and covalent functionalization do not alter the distribution of nanotube types (semiconducting and metallic) and diameters as verified by radial breathing modes (RBMs) measured across all specimens (Figure 4.3).

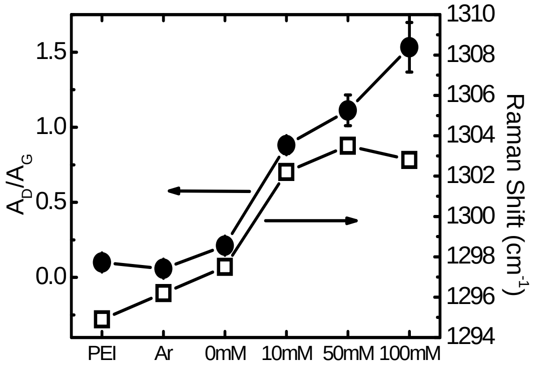

Figure 4.2. Relative disorder (defined as integrated intensity ratio of D-band to G-band, A_D/A_G) and D-band frequency (representing relative degree of doping, ~1300cm^{-1}) of functionalized (4-NBDT solution concentration in mM), Ar-annealed, and PEI doped HiPCO samples. Error bars (some smaller than the symbols) are obtained from average of spectra collected at three different locations of each sample. Connecting lines are guides to the eye.

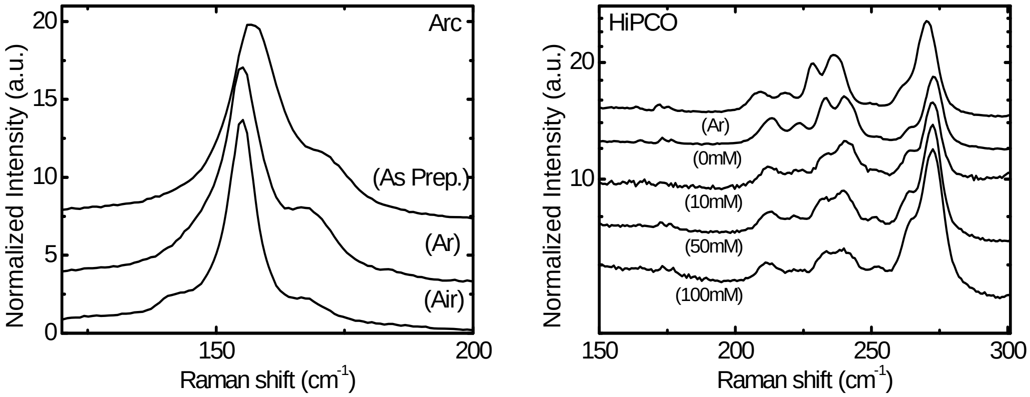

Figure 4.3. Static Raman spectra of RBM regions for various arc-discharge (left) and HiPCO (right) nanotube samples. Spectra are offset for clarity.

4.4 Potential Laser-Induced Sample Damage and Heating

Before discussing TRIARS measurements of OP lifetimes, possible laser-induced damage and heating need to be considered. This is especially important since introduction of defects in graphitic materials is known to lower thermal conductivity,[39, 40] which can then enhance laser heating and damage. Laser-induced damage can be easily monitored by examining A_D/A_G ratio in the Raman spectrum. Raman spectra of our most defective/functionalized (and therefore least thermally conductive) sample after PEI doping, HiPCO(100 mM/PEI), shows no increase in A_D/A_G after TRIARS measurements and laser heating measurements (discussed below) where laser intensity was varied up to the maximum used in all experiments here. Therefore, we conclude that we are in a regime where laser damage is negligible.

Even in the absence of actual damage, laser irradiation of carbon nanotubes may cause sample heating, which is known to change the phonon lifetime.[18] Raman thermometry can be used to determine the degree of laser induced heating through frequency shifts of the G-band.[41] Static Raman measurements with the sample mounted on a heating stage under Ar are carried out to calibrate G^+ peak shift with temperature. From Figure 4.4(a), we determine –0.033cm^{-1}/K, similar to the slope for graphene in Ref. 41. Figure 4.4(b) shows G^+ peak frequencies at different laser intensities for HiPCO(0 mM) and HiPCO(100 mM/PEI) samples. Even for our most defective sample under laser intensities higher than those used for TRIARS measurements, no down-shift in the G^+ peak frequency is observed. Therefore, we expect laser heating to have a negligible effect in sample temperature increase (< ~20 K based on our spectral resolution of 0.7 cm^{-1}). Given the assumption that lifetime scales inversely with temperature,[35] this upper limit in laser-induced temperature increase leads to less than ~6 % change in T_1. Furthermore, we have also measured T_1 at multiple laser fluences to verify that laser heating effects are insignificant even for the sample with the highest degree of functionalization (Figure 4.5). Indeed, within our experimental error of ±0.1 ps, T_1 is the same for both half and double the usual TRIARS laser fluence used.

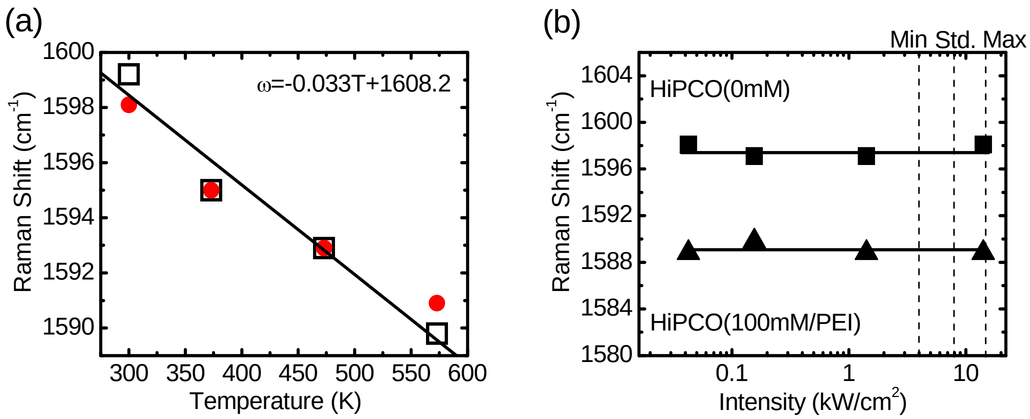

Figure 4.4. (a) Temperature dependence of G^+ peak frequency obtained for HiPCO(0 mM) sample measured by heating the substrate and probing with low intensity (127 W/cm^2) HeNe laser. Circles and squares correspond to two different heating cycles. (b) Effects of laser intensity on G^+ peak frequency of HiPCO(0 mM) and HiPCO(100 mM/PEI) samples. "Min" and "Max" refer to the minimum and maximum TRIARS laser intensities used to verify that the laser heating and damage are negligible. "Std." is the value of intensity used for all other TRIARS measurements (I = 7.9 kW/cm^2). Relative disorder, A_D/A_G, is the same after laser power dependence and TRIARS measurements even for the most defective sample, HiPCO(100 mM/PEI).

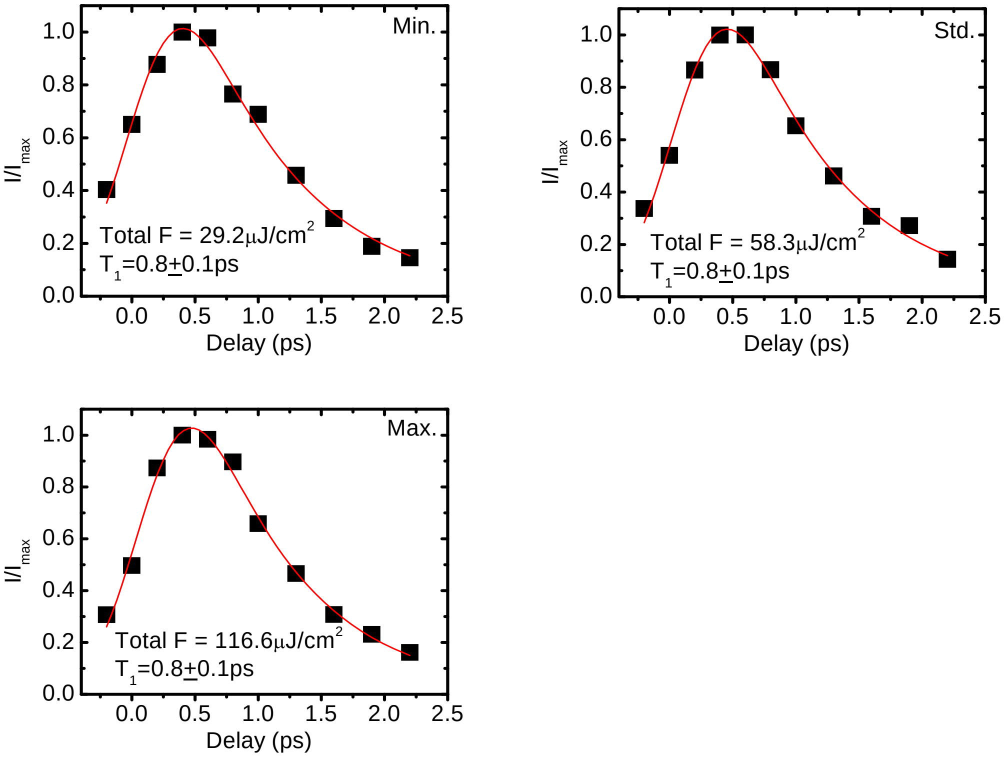

Figure 4.5. OP lifetime, T_1, for HiPCO(100 mM/PEI) sample at multiple total laser fluences showing that the lifetime is independent of fluence used. "Min", "Std.", and "Max" naming conventions are identified in Figure 4.4(b). HiPCO(100 mM/PEI) is used as it is expected to be least thermally conductive due to it having the highest defect concentration.

4.5 Doping Effects on Optical Phonon Linewidth

Having established that, even at the highest fluence for the most defective samples, laser heating and damage are negligible, we consider now how doping affects G-band OP lifetime and Raman linewidth. Examples of TRIARS spectra at different time delays for HiPCO(0 mM) sample are shown in Figure 4.6(a). Figure 4.6(b) shows the OP decay in three of the non-functionalized samples as measured by TRIARS. In Figure 4.7, G-band OP lifetimes are plotted as a function of D-band frequency for all thin film samples. Note that at a fixed laser energy, higher frequency D-band corresponds to more p-type doping. For arc-discharge nanotubes, annealing in air does not alter the D-band frequency (and therefore the degree of doping) but increases the OP lifetime slightly from 1.0 ± 0.1 ps to 1.3 ± 0.1 ps. Annealing in Ar and PEI adsorption do alter the D-band frequency in HiPCO nanotubes but T_1 remains the same within the experimental error. For HiPCO(10 mM), HiPCO(50 mM), and HiPCO(100 mM) samples, T_1 remains the same after PEI doping even with a D-band frequency difference of up to ~8 cm^{-1} (or Fermi level position difference on the order of 1 eV).[37] However, in the latter set of functionalized samples, defects altering T_1 may prevent observation of possible doping induced changes in T_1.

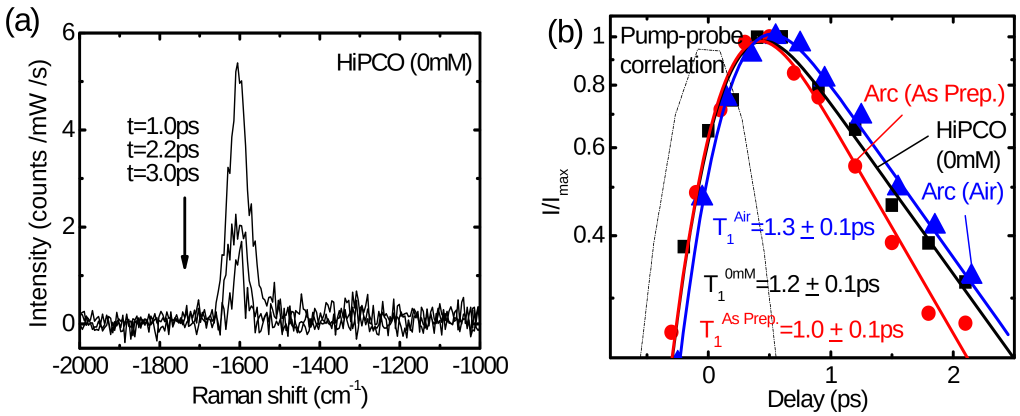

Figure 4.6. (a) Examples of background (signal at delay stage position of t = -10ps) subtracted TRIARS spectra. (b) Normalized integrated TRIARS intensity (I/I_{max}) as a function of probe delay for Arc(As Prep), Arc(Air), and HiPCO(0 mM) samples with A_D/A_G of 0.56 ± 0.01, 0.11 ± 0.02, and 0.21 ± 0.03 respectively. Pump-probe correlation is also shown.

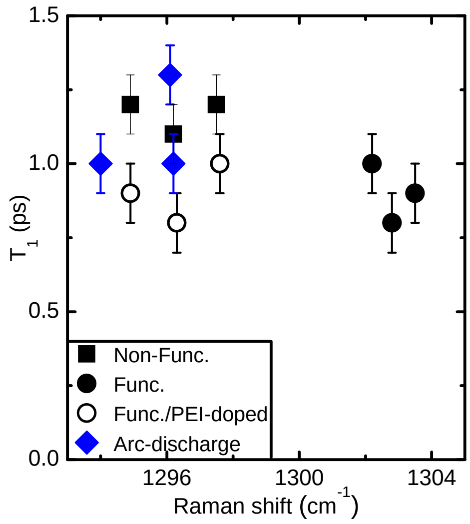

Figure 4.7. OP lifetime, T_1, vs. D-band frequency for non-functionalized (square), functionalized (filled circle), and functionalized/PEI-doped (open circle) HiPCO nanotubes as well as air- and Ar-annealed and non-annealed arc-discharge samples (diamond). No obvious dependence on degree of doping is observed.

In the low defect limit (i.e. non-functionalized nanotube films), doping with PEI leads to a relatively small downshift in the D-band frequency (< 3 cm^{-1}). A larger change in the degree of doping is likely to be necessary to ascertain whether or not there is an effect from doping. Unfortunately, dense films of bundled nanotubes used in TRIARS measurements do not exhibit significant Raman D-band frequency shifts upon electrolyte gating. Therefore, we consider doping dependent linewidth of individual nanotubes, which can be gated much more effectively and are more likely to provide homogeneous linewidths. We limit our discussion here to semiconducting nanotubes since the degree of line broadening dominated by EPC in metallic nanotubes varies from tube to tube as well as with doping. If optical phonon relaxation by carrier excitation in metallic nanotubes dominated the lifetime, typical G-band linewidths of several tens of cm^{-1} would also correspond to a time scale beyond our temporal resolution of TRIARS measurements. Furthermore, high electronic temperature induced by the pump in TRIARS has been shown to remove EPC effects in graphite as evidenced by transient stiffening of the G-band[11] and we anticipate similar effects making carrier excitation induced fast decay expected in metallic nanotubes to have negligible contributions to our measured TRIARS signal. Figure 4.8(a) shows the gate voltage dependence of G^+ peak linewidth for a single semiconducting nanotube which does not exhibit measurable D-band (i.e. low defect limit). G^- peak linewidths are usually similar to those of G^+ peak and therefore we focus on the higher intensity G^+ peak. At the charge neutrality point (V_G = - 0.3 V), the linewidth is the narrowest with Γ = 5 cm^{-1}, corresponding to $T_2/2$ = 1.1 ps. This value is similar to the measured OP lifetime of ~1.2 ps for low defect samples.

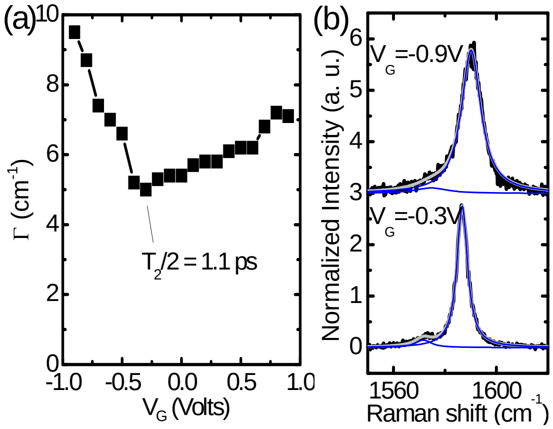

Figure 4.8. (a) Dependence of G^+ peak linewidth Γ on doping (varied by gate voltage, V_G) for a single semiconducting nanotube with no observable D-band. (b) Fitted Raman spectra at V_G = -0.3 V and V_G = -0.9 V, the narrowest and broadest spectra respectively. Overall fit in gray and components in blue. Simultaneous electrical/static Raman measurement conditions are described in Ref. 16.

When electrostatic gating introduces carriers into the semiconducting nanotube, G^+ peak linewidth nearly doubles to 9.5 cm^{-1}. Static Raman spectra of the G-band (along with two-Lorentzian curve fits) at two indicated gate voltages are shown in Figure 4.8(b). The increase in G-band linewidth of semiconducting nanotubes with doping has also been reported previously, with larger increase using electrolyte gate[17] (as used here) than with back gate[15] configuration due to the much higher efficiency of polymer electrolyte gating. Semiconducting nanotubes are expected to exhibit G-band phonon softening similar to metallic nanotubes but with a smaller degree of softening and *without* line broadening due to virtual electron-hole pair generation rather than actual carrier excitation.[15, 42] A possible origin of the broadening may be gate inducing charges near the nanotube (e.g. on substrate and/or adsorbed molecules) leading to variations in local electric fields which in turn can cause inhomogeneous broadening. Doping causing only inhomogeneous broadening and leaving the homogeneous linewidth unchanged would be consistent with doping independent T_1. Unfortunately, strongly non-equilibrium behavior expected of OPs due to the pump pulse in TRIARS prevents direct comparison of T_1 with linewidth obtained by static Raman measurements. Doping dependent Raman linewidth does, however, indicate that the observed variations in the G-band linewidth of individual semiconducting nanotubes (which is often reported to range between 6 to 12 cm^{-1})[33] are, at least in part, due to variations in molecular adsorption from the ambient and/or substrate induced doping/charging.[37, 43]

4.6 Defect Effects on Optical Phonon Lifetime

While doping broadens Raman linewidth without an apparent change to T_1, we observe that defects alter both. HiPCO(0 mM) and Arc(As-Prep.) samples, whose TRIARS measurements are shown in Figure 4.6(b), are prepared in the same manner here as samples reported in Ref. 18. The T_1 values measured are similar in both cases with the HiPCO sample having a slightly longer lifetime (1.0 ± 0.1 ps vs. 1.2 ± 0.1 ps). However, the difference in the degree of disorder between these two samples is significant. For HiPCO(0 mM) sample, $A_D/A_G = 0.21 \pm 0.03$ whereas $A_D/A_G = 0.56 \pm 0.01$ for Arc(As-Prep.) sample as shown in Figure 4.1(a) and bottom spectrum in Figure 4.1(b), respectively. After annealing in air, arc-discharge nanotubes show a marked decrease in A_D/A_G down to 0.11 ± 0.02 [top spectrum in Figure 4.1(b)]. This reduction in defect density leads to an increase in T_1 from 1.0 ± 0.1 ps to 1.3 ± 0.1 ps, now comparable to HiPCO(0 mM). This result suggests that HiPCO and arc-discharge nanotubes, although having different degree of metallic/semiconducting contributions to the measured static Raman spectra, exhibit similar OP lifetimes. Based on pump-induced transient decoupling of OP-mediated electronic transitions observed in graphite,[11] similar OP lifetimes in metallic and semiconducting nanotubes may be expected and can explain these results. The key difference observed between HiPCO and arc-discharge tubes prior to annealing appears to be the consequence of variations in the defect concentration.

Covalent functionalization with 4-NBDT provides a more systematic way to investigate the influence of defects on OP lifetime. Figure 4.9(a) shows the two extremes. Functionalization of HiPCO nanotubes with 100 mM 4-NBDT decreases T_1 from 1.2 ± 0.1 ps to 0.8 ± 0.1 ps while increasing A_D/A_G from 0.21 ± 0.03 to 1.53 ± 0.17. The dependence of T_1 on A_D/A_G for all thin film samples studied is shown in Figure 4.9(b). The corresponding lifetime broadening, defined here as $(2\pi c T_1)^{-1}$, is shown in Figure 4.10. In order to compare to reported correlation between defect density and D to G ratio,[44-52] data in Figure 4.10 are plotted using D-band and G-band peak height ratios, I_D/I_G, rather than the integrated intensity ratios. Using integrated intensity ratios leads to the same trend. Based on Ref. 49, where defect concentrations were estimated from thermogravimetric analysis of 4-NBDT functionalized nanotubes, we estimate the sample with maximum disorder to have defect density of ~1 defect per 50 lattice C atoms.[53] Using a more widely used relation for nanographitic materials,[48, 50-52] we calculate crystallite size L_a ~ 130 nm from which we estimate defect density of ~1 defect per 300 lattice C atoms.[54] Taking the average of these two values, we estimate ~1 defect per 175 lattice C atoms to cause 0.4 ps decrease in T_1 or a change in lifetime broadening of ~2 cm^{-1}.

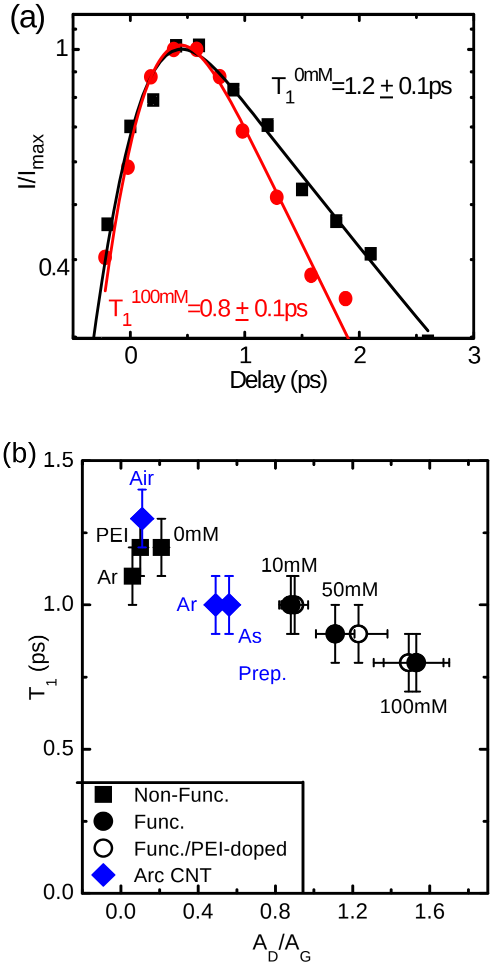

Figure 4.9. (a) Normalized integrated TRIARS intensity (I/I_{max}) as a function of probe delay for HiPCO(0 mM) (black square) and HiPCO(100 mM) (red circle) samples with A_D/A_G of 0.21 ± 0.03 and 1.53 ± 0.17, respectively. (b) OP lifetime (T_1) dependence on relative defect concentration (i.e., A_D/A_G) for non-functionalized (square), functionalized (filled circle), and functionalized/PEI-doped (open circle) HiPCO nanotubes as well as arc-discharge samples (diamond). T_1 error bars are from least-squares curve fitting and A_D/A_G error bars are from variations measured at three different locations in each sample.

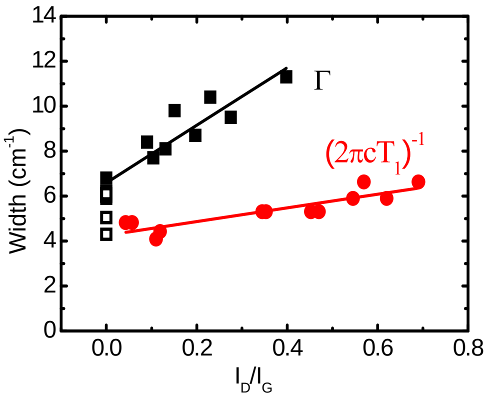

Figure 4.10. Influence of relative defect concentration, I_D/I_G (peak height ratio), on lifetime broadening, $(2\pi cT_1)^{-1}$, calculated from T_1 values measured by TRIARS and total linewidth of G^+ peak, Γ, of single semiconducting nanotubes from static Raman measurements. Lines are linear fits. Open squares correspond to linewidths of electrostatically gated single semiconducting nanotubes where charge neutrality is ensured.

Figure 4.10 also compares the G^+ peak linewidth Γ of individual semiconducting nanotubes with lifetime broadening of thin film samples. Both increase approximately linearly with defect density. The static Raman linewidth of single nanotubes exhibits stronger dependence on I_D/I_G but this may be a consequence of defect induced inhomogeneous broadening.[21, 24, 55, 56] However, in the limit of zero-defects for charge neutral nanotubes, Γ and lifetime broadening converge. Note that the slight offset for the filled squares at $I_D/I_G = 0$ is likely to be arising from doping/charging as discussed in the previous section. The open squares are from electrochemically gated nanotubes where zero-doping is ensured. These data points therefore provide a better upper limit on the homogeneous linewidth.

While the convergence of Γ and lifetime broadening at zero-charge and zero-doping limit can imply that T_1 dominates the overall dephasing time in nanotubes, effects of high transient electronic temperature induced by the pump beam in the TRIARS measurements need to be considered before such conclusions can be made. In graphite, the high electronic temperature has been shown to lead to an equivalent effect as gate shifting the Fermi level away from the Dirac point and OP relaxation via carrier excitation becomes no longer accessible or less likely.[11]

The measured T_1 of 2.2 ~ 2.4 ps in Refs. 11 and 35 is in reasonable agreement with calculated lifetime based on anharmonic decay, mainly into two acoustic phonons. In graphene, a faster T_1 of ~ 1.2 ps has been suggested to arise from coupling to the substrate.[35] Carbon nanotubes also exhibit similar faster T_1 of ~1.2 ps but the substrate is not likely to be providing additional decay paths. In the relatively thick films of nanotubes used here and in Ref. 18, the majority of the nanotubes are not directly supported by the substrate. Furthermore, nanotubes suspended in D_2O exhibit similar T_1 of 1.1 ps.[32] TRIARS measurements are carried out with OP population far from equilibrium and the decay rate observed may be different than that expected of near-equilibrium situation and therefore comparison to linewidth obtained through static Raman measurements may be problematic. However, slower, rather than faster, OP relaxation is expected far from equilibrium as shown in bilayer graphene and graphite[57] and as suggested by a slight decrease in T_1 with decreasing pump power in carbon nanotubes.[18] Even if we assume zero-doping, zero-charge limit Γ of 4 ~ 5 cm^{-1} giving only an upper limit for homogeneous linewidth, imposing that the pump in TRIARS measurements causes measured T_1 values to be larger than the actual (or near-equilibrium) lifetime would lead to an unreasonable result of lifetime broadening being larger than the homogeneous width. One possible explanation of observed T_1 in carbon nanotubes being faster than the expected anharmonic decay rates in graphene and graphite is coupling of G-band mode to RBM phonons.[58] Since this decay path is accessible only when the nanotube is photoexcited, near-equilibrium OP lifetime can be expected to be longer in this case. Then, Γ ~ 4 cm^{-1} from static Raman measurements must include additional decay path, dephasing process or inhomogeneous broadening. However, it appears somewhat fortuitous that any of these processes should lead to the near-equilibrium linewidth being same as lifetime broadening that includes an unrelated anharmonic decay into

RBM phonon far from equilibrium. Whether or not the convergence of Γ and lifetime broadening is an unrelated coincidence remains an open question.

Decreasing T_1 with defects observed in Figure 4.9(b) is surprising in that defects have been shown to have little or no effect on OP lifetimes in other materials.[55, 56] In graphene, conflicting results exist where both I_D/I_G dependent[59] and independent[57] OP lifetimes have been reported. Point defects are often considered to cause elastic scattering of phonons and therefore the rates of anharmonic decay into lower energy phonons are not expected to be altered.[12, 60] However, 4-NBDT molecules used here introduce relatively large nitrophenyl groups chemisorbed on the sidewalls of nanotubes and hence may not be treated as simple point defects. The combination of adsorbed chemical groups and lattice disorder induced by functionalization with 4-NBDT may lead to additional relaxation pathways. Existing defects can also enhance reactivity of neighboring lattice atoms,[61, 62] and therefore the distribution of functional groups and disorder in the lattice may not be uniform which may further facilitate OP relaxation.

4.7 D-band Optical Phonon Lifetime

For the samples with the highest degree of functionalization, HiPCO(50 mM) and HiPCO(100 mM), the D-band intensity is large enough which makes it possible to determine an OP population lifetime for this peak as well, as shown in Figure 4.11. As discussed in Chapter 2, the D-band is a double-resonance scattering processing including an elastic scattering event which is required for the D-band to appear from the probe pulse, independent of how the phonons were introduced (e.g. with a pump pulse). Despite this, the inelastic and elastic processes occur simultaneously and on the order of 100 fs so the TRIARS-determined OP lifetime of this phonon should be as valid as that for the G-band. It appears that, despite a significant difference in A_D/A_G, the lifetimes between the two samples are the same which is surprising since G-band OP lifetime has been shown to depend on defect concentration. One possible reason for this result can be that 4-NBDT does not have any modes near D-band phonon energies into which D-band phonons from the nanotubes can decay into (unlike G-band phonons). This further motivates a study of OP lifetime dependence on defect concentration of different defect types (e.g. ion irradiation, charged, covalent with different functional groups).

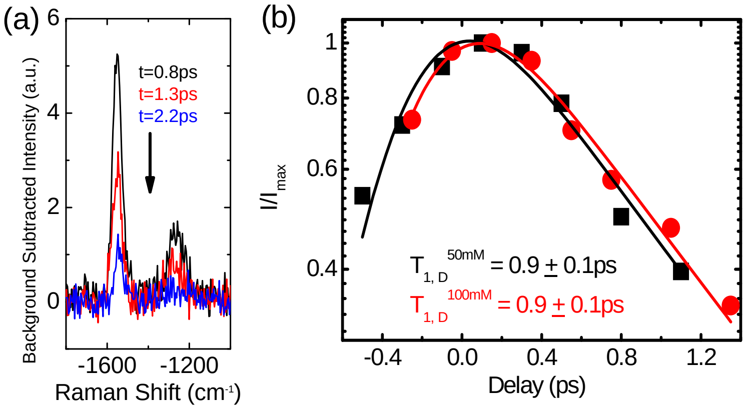

Figure 4.11. (a) Example background (t=-10ps) subtracted spectra at different delay stage positions for HiPCO(100 mM). (b) Normalized integrated TRIARS intensity (I/I_{max}) of the D-band as a function of probe delay for HiPCO(50 mM) (black square) and HiPCO(100 mM) (red circle) samples with A_D/A_G of 1.11 ± 0.10 and 1.53 ± 0.17 respectively. D-band OP lifetimes, $T_{1,D}$, are indicated. Plots manually offset by t_0 (see Chapter 2.2) for I_{max} to approximately coincide. D-band intensity for other samples too small to obtain $T_{1,D}$.

4.8 Conclusions

By varying the doping level in individual semiconducting carbon nanotubes using polymer electrolyte gating, we have shown that Raman G-band linewidth as narrow as ~4 cm^{-1} can be observed at the charge neutrality point. Variations in molecular adsorption from the ambient and/or substrate induced doping/charging may be the main reason for larger values and variations in linewidths (6 – 12 cm^{-1}) often reported. Optical phonon lifetime does not change within the doping range achievable here for thin films of nanotubes. Increasing disorder, on the other hand, alters both linewidth and the lifetime. Lifetime broadening inferred from measured T_1 and linewidth Γ measured by static Raman both scale linearly with I_D/I_G with the latter having a stronger dependence likely due to inhomogeneous broadening caused by covalent functionalization. In the limit of zero-doping and zero-defects, the measured Γ of single semiconducting nanotubes coincide with lifetime broadening expected from measured T_1 of 1.2 ps. By reducing the degree of defect induced changes on the observed OP lifetime, we have also shown that samples displaying different degree of metallic/semiconducting character exhibit similar T_1 value of ~1.2 ps.

4.9 References

[1] Tans, S. J.; Verschueren, A. R. M.; Dekker, C., *Nature* **1998,** *49*, 393.

[2] Kong, J.; Franklin, N. R.; Zhou, C.; Chapline, M. G.; Peng, S.; Cho, K.; Dai, H., *Science* **2000,** *287,* 622.

[3] Kang, S. J.; Kocabas, C.; Ozel, T.; Shim, M.; Pimparkar, N.; Alam, M. A.; Rotkin, S. V.; Rogers, J. A., *Nat. Nanotechnol.* **2007**, *2*, 230.

[4] Sazonova, V.; Yaish, Y.; Ustunel, H.; Roundy, D.; Arias, T. A.; McEuen, P. L., *Nature* **2004**, *341*, 284.

[5] Abdula, D.; Shim, M., *ACS Nano* **2008**, *2*, 2154.

[6] Zhou, X.; Park, J.; Huang, S.; Liu, J.; McEuen, P. L., *Phys. Rev. Lett.* **2005**, *95*, 146805.

[7] Yao, Z.; Kane, C. L.; Dekker, C., *Phys. Rev. Lett.* **2000**, *84*, 2941.

[8] Javey, A.; Guo, J.; Paulsson, M.; Wang, Q.; Mann, D.; Lundstrom, M.; Dai, H., *Phys. Rev. Lett.* **2004,** *92*, 106804.

[9] Park, J. Y.; Rosenblatt, S.; Yaish, Y.; Sazonova, V.; Ustunel, H.; Braig, S.; Arias, T. A.; Brouwer, P.; McEuen, P. L., *Nano Lett.* **2004**, *4*, 517.

[10] Perebeinos, V.; Tersoff, J.; Avouris, P., *Phys. Rev. Lett.* **2005**, *94*, 086802.

[11] Yan, H.; Song, D.; Mak, K. F.; Chatzakis, I.; Maultzsch, J.; Heinz, T. F., *Phys. Rev. B* **2009**, *80*, 121403(R).

[12] Del Fatti, N.; Ganikhanov, F.; Langot, P.; Tommasi, R.; Vallee, F., *J. Nonlinear Opt. Phys. Mater.* **1998**, *7*, 271.

[13] Wu, Y.; Maultzsch, J.; Knoesel, E.; Chandra, B.; Huang, M.; Sfeir, M. Y.; Brus, L. E.; Hone, J.; Heinz, T. F., *Phys. Rev. Lett.* **2007**, *99*, 027402.

[14] Piscanec, S.; Lazzeri, M.; Mauri, F.; Ferrari, A. C.; Robertson, J., *Phys. Rev. Lett.* **2004**, *93*, 185503.

[15] Tsang, J. C.; Freitag, M.; Perebeinos, V.; Liu, J.; Avouris, Ph., *Nat. Nanotechnol.* **2007**, *2*, 725.

[16] Nguyen, K. T.; Gaur, A.; Shim, M., *Phys. Rev. Lett.* **2007,** *98*, 145504.

[17] Das, A.; Sood, A. K.; Govindaraj, A.; Saitta, A. M.; Lazzeri, M.; Mauri, F.; Rao, C. N. R., *Phys. Rev. Lett.* **2007,** *99*, 136803.

[18] Kang, K.; Ozel, T.; Cahill, D. G.; Shim, M., *Nano Lett.* **2008,** *8*, 4642.

[19] Petzelt, J.; Setter, N., *Ferroelectrics* **1993,** *150*, 89.

[20] Cusco, R.; Alarcon-Llado, E.; Ibanez, J.; Artus, L.; Jimenez, J.; Wang, B.; Callahan, M. J., *Phys. Rev. B* **2007,** *75*, 165202.

[21] Millot, M.; Tena-Zaera, R.; Munoz-Sanjose, V.; Broto, J.; Gonzalez, J., *Appl. Phys. Lett.* **2010,** *96*, 152103.

[22] Anand, S.; Verma, P.; Jain, K. P.; Abbi, S. C., *Physica B* **1996,** *226*, 331.

[23] Zhao, Q.; Zhang, H.; Xu, X.; Wang, Z.; Xu, J.; Yu, D., *Appl. Phys. Lett.* **2005,** *86,* 193101.

[24] Bergman, L.; Alexson, D.; Murphy, P. L.; Nemanich, R. J.; Dutta, M.; Stroscio, M. A.; Balkas, C.; Shin, H.; Davis, R. F., *Phys. Rev. B* **1999,** *59*, 12977.

[25] Hase, M.; Ishioka, K.; Kitajima, M.; Ushida, K.; Hishita, S., *Appl. Phys. Lett.* **2000,** *76*, 1258.

[26] Ishioka, K.; Hase, M.; Kitajima, M.; Ushida, K., *Appl. Phys. Lett.* **2001,** *78*, 3965.

[27] Ishioka, K.; Hase, M.; Ushida, K.; Kitajima, M., *Appl. Surf. Sci.* **2002,** *197*, 726.

[28] Nguyen, K. T.; Shim, M., *J. Am. Chem. Soc.* **2009,** *131*, 7103.

[29] Abdula, D.; Nguyen, K. T.; Shim, M., *J. Phys. Chem. C* **2007,** *111*, 17755.

[30] Fischer, S. F.; Laubereau, A., *Chem. Phys. Lett.* **1975,** *35,* 6.

[31] Lee, Y. J.; Parekh, S. H.; Fagan, J. A.; Cicerone, M. T., *Phys. Rev. B* **2010,** *82*, 165432.

[32] Song, D.; Wang, F.; Dukovic, G.; Zheng, M.; Semke, E. D.; Brus, L. E.; Heinz, T. F., *Phys. Rev. Lett.* **2008,** *100,* 225503.

[33] Jorio, A.; Souza Filho, A. G.; Dresselhaus, G.; Dresselhaus, M. S.; Swan, A. K.; Unlu, M.S.; Goldberg, B. B.; Pimenta, M. A.; Hafner, J. H.; Lieber, C. M.; Saito, R., *Phys. Rev. B* **2002,** *65,* 155412.

[34] Ikeda, K.; Uosaki, K., *Nano Lett.* **2009,** *9*, 1378.

[35] Kang, K.; Abdula, D.; Cahill, D. G.; Shim, M., *Phys. Rev. B* **2010,** *81*, 165405.

[36] Kang, K.; Koh, Y. K.; Chiritescu, C.; Zheng, X.; Cahill, D. G., *Rev. Sci. Instrum.* **2008,** *79*, 114901.

[37] Shim, M.; Gaur, A.; Nguyen, K. T.; Abdula, D.; Ozel, T., *J. Phys. Chem. C* **2008,** *112*, 13017.

[38] Shim, M.; Ozel, T.; Gaur, A.; Wang, C., *J. Am. Chem. Soc.* **2006,** *128*, 7522.

[39] Hooker, C. N.; Ubbelohde, A. R.; F. R. S.; Young, D. A., *Proc. R. Soc. A* **1963,** *276*, 83.

[40] Klemens, P. G.; Pedraza, D. F., *Carbon* **1994,** *32*, 735.

[41] Abdula, D.; Ozel, T.; Kang, K.; Cahill, D. G.; Shim, M., *J. Phys. Chem. C* **2008,** *112*, 20131.

[42] Das, A.; Sood, A. K., *Phys. Rev. B* **2009,** *79*, 235429.

[43] Gaur, A.; Shim, M., *Phys. Rev. B* **2008,** *78*, 125422.

[44] Tuinstra, F.; Koenig, J. L., *J. Chem. Phys.* **1970,** *53*, 1126.

[45] Ferrari, A. C.; Robertson, J., *Phys. Rev. B* **2000,** *61*, 14095.

[46] Niyogi, S.; Bekyarova, E.; Itkis, M. E.; Zhang, H.; Shepperd, K.; Hicks, J.; Sprinkle, M.; Berger, C.; Lau, C. N.; deHeer, W. A.; Conrad, E. H.; Haddon, R. C., *Nano Lett.* **2010,** *10*, 4061.

[47] Lucchese, M. M.; Stavale, F.; Ferreira, E. H. M.; Vilani, C.; Moutinho, M. V. O.; Capaz, R. B.; Achete, C. A.; Jorio, A., *Carbon* **2010,** *48*, 1592.

[48] Ni, Z. H.; Ponomarenko, L. A.; Nair, R. R.; Yang, R.; Anissimova, S.; Grigorieva, I. V.; Schedin, F.; Blake, P.; Shen, Z. X.; Hill, E. H.; Novoselov, K. S.; Geim, A. K., *Nano Lett.* **2010,** *10,* 3868.

[49] Stephenson, J.; Hudson, J. L.; Leonard, A. D.; Price, B. K.; Tour, J. M., *Chem. Mater.* **2007,** *19*, 3491.

[50] Cancado, L. G.; Takai, K.; Enoki, T.; Endo, M.; Kim, Y. A.; Mizusaki, H.; Jorio, A.; Coelho, L. N.; Magalhaes-Paniago, R.; Pimenta, M. A., *Appl. Phys. Lett.* **2006,** *88*, 163106.

[51] Soin, N.; Roy, S. S.; Ray, S. C.; McLaughlin, J. A., *J. Raman Spectrosc.* **2010,** *41*, 1227.

[52] Chen, J.; Cullen, W. G.; Jang, C.; Fuhrer, M. S.; Williams, E. D., *Phys. Rev. Lett.* **2009,** *102*, 236805.

[53] In Ref. 49, a 633 nm laser was used whereas we have used a 785 nm source. To estimate defect density measured by 785 nm laser source, we multiply our measured I_D/I_G by $(633\text{ nm}/785\text{ nm})^4$ to account for the laser wavelength to the 4th power dependence.

[54] The relation $L_a(\text{nm}) = (2.4\times10^{-10})\lambda^4(nm) \times (I_D/I_G)^{-1}$ is used to obtain crystallite size L_a which takes into account excitation wavelength λ. Approximating a circular crystallite shape, the number of functional groups per lattice carbon atom can be estimated as: $\#/\text{C} = [2\pi(L_a/2)/(a_{C\text{-}C}\times\cos(30^{\circ}))]/[\rho\times\pi(L_a/2)^2]$ where $a_{C\text{-}C}$ is the C-C bond length and ρ is carbon atom density of graphene, which reduces to $\#/\text{C} = 3a_{C\text{-}C}/L_a$. This equation treats the circumference of the crystallite as being entirely functionalized and therefore the ratio of the number of atoms along the circumference to those within the area of the crystallite equals #/C.

[55] Tsen, K. T.; Morkoc, H., *Phys. Rev. B* **1998,** *37*, 7137.

[56] Kash, J. A.; Jha, S. S.; Tsang, J. C., *Phys. Rev. Lett.* **1988,** *58*, 1869.

[57] Wang, H.; Strait, J. H.; George, P. A.; Shivaraman, S.; Shields, V. B.; Chandrashekhar, M.; Hwang, J.; Rana, F.; Spencer, M. G.; Ruiz-Vargas, C. S.; Park, J., *Appl. Phys. Lett.* **2010,** *96*, 081917.

[58] Gambetta, A.; Manzoni, C.; Menna, E.; Meneghetti, M.; Cerullo, G.; Lanzani, G.; Tretiak, S.; Piryatinski, A.; Saxena, A.; Martin, R. L.; Bishop, A. R., *Nat. Phys.* **2006,** *2*, 515.

[59] Dawlaty, J. M.; Shivaraman, S.; Chandrashekhar, M.; Rana, F.; Spencer, M. G., *Appl. Phys. Lett.* **2008**, *92*, 042116.

[60] Hase, M.; Kitajima, M., *J. Phys.: Condens. Matter* **2010,** *22,* 073201.

[61] Wang, C.; Zhou, G.; Wu, G.; Gu, B.; Duan, W., *Appl. Phys. Lett.* **2006,** *89*, 173130.

[62] Fan, Y.; Goldsmith, B.R.; Collins, P. G., *Nat. Mater.* **2005,** *4*, 906.

CHAPTER 5

CHARGE TRANSFER DOPING VIA ADSORPTION

Having understood how covalent chemistry can influence optical phonon properties in sp^2-bonded carbon nanostructures, we now consider non-covalent adsorption chemistry. Here, a discussion of adsorption-induced doping in single layer graphene is provided through the use of static Raman spectroscopy. Inadvertent doping due to sample ambient environment exemplifies doping sensitivity of these all-surface nanostructures-- an advantage for device fabrication. Removal of this doping has allowed us to investigate electron-phonon coupling dependence on temperature, also of interest for devices operating above room temperature. This work has been published in Ref. [1].

5.1 Introduction

Having one of the highest carrier mobilities ever reported[2, 3] because of unique electronic structure, as discussed in Chapter 1, integration of single-layer graphene (SLG) in electronic devices is of pronounced interest. Raman spectroscopy has proven to be a key tool for characterization of SLG doping and vibrational band structure[4-8] which are arguably the most important characteristics governing electronic transport: doping determines carrier type and concentration and phonon band structure determines the vibrational modes that cause carrier scattering. Though the response of graphene to various gas atmospheres has been considered for sensor applications,[9, 10] there have been limited studies addressing effects an ambient air environment has on the Fermi level position and phonon modes of this all-surface material.[11-13] Carbon nanotubes exhibit significant changes in electrical and optical characteristics due to ambient air.[14-18] These effects of the ambient surrounding are important to consider since SLG would undergo processing, such as lithography, for use in devices or even be operated in contact with various materials (such as top gate dielectrics for transistors or low-k material for interconnects) that may compromise its supposed high performance.

Our Raman spectroscopy study elucidates the differences between “air-altered” and “intrinsic” behavior of SLG on SiO_2 substrates. By intrinsic, we refer to the behavior observed under Ar atmosphere after minimizing effects of ambient air by thermal annealing under Ar. A primary cause of these discrepancies is shown to be effects of O_2 from ambient air. With this knowledge, we then proceed to investigate the temperature dependence of G-band (occuring ~1585 cm^{-1}) and 2D-band (~2680 cm^{-1}) peak frequencies and linewidths of intrinsic SLG. This information is valuable in understanding electron-phonon coupling (EPC) and anharmonic phonon-phonon interactions in graphene and is also useful for predicting performance of graphene-based electronic devices operating at elevated temperatures.

Graphene samples were made via mechanical exfoliation of highly-oriented pyrolytic graphite on SiO_2/Si substrates with 300 nm thick oxide, as discussed in Chapter 2.[19, 20] Raman spectra were acquired with a 532 nm laser excitation and a 100X long working distance air objective providing a spot size of ~1 μm. Power at the objective is ~3 mW. *In situ* Raman measurements were carried out in an air-tight heating stage having an inlet and exhaust for gas flow. All Ar annealing was carried out with a flow rate of 20 cm^3/min and heating and cooling rates of 10 K/min. Spectra were collected 10 min after each temperature of interest was reached (298K, 373K, 473K, and 573K). Unlike heating SLG under O_2-rich atmosphere, which has been shown to lead to large D-band appearance and observable etch pits,[12] our mild thermal treatment under inert atmosphere does not create an observable D-band.

5.2 Effects of Ambient Environment on Single-Layer Graphene

Figure 5.1 shows the Raman spectra and corresponding fitting curves for the G- and 2D-bands of a SLG sample (referred to here on as sample S1) as prepared in air, after Ar annealing at 573K, and after subsequent exposure to O_2 flow of 10 cm^3/min for 5 min at 298K. Fits are composed of a single Lorentzian curve for both G- and 2D-bands, the latter being evidence that S1 is SLG.[21-23] Spectra for another sample (S2, discussed later) are shown in Figure 5.3 which confirms it is SLG also. The inset of Figure 5.1 shows absence of the D-band (expected at ~1340 cm^{-1}).[4] Even with extended collection time and averaging giving a signal-to-noise ratio of ~60 or better for the 2D-band peak, no D-band is observed at the same baseline noise level. All spectra taken for S1 and S2, independent of temperature and sample environment, do not exhibit any detectable D-band which is indicative of the quality of our samples.

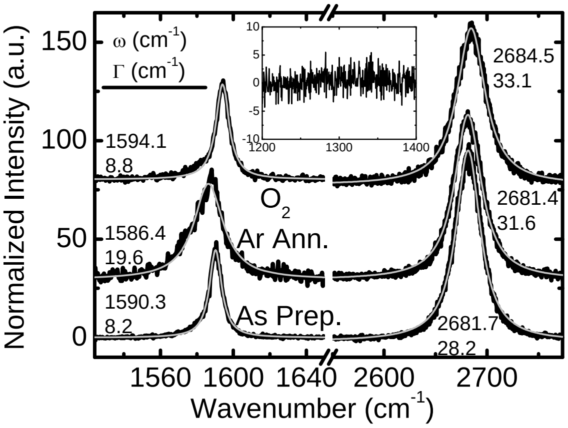

Figure 5.1. G- and 2D-band behavior of single-layer graphene (sample S1) as prepared, after Ar annealing, and after subsequent O_2 exposure. Middle spectrum labeled "Ar Ann." corresponds to measurement at room temperature (same temperature as the other two spectra) after Ar annealing at 573 K. Inset is of the D-band region showing no peak intensity. Lorentzian fits are in gray within the actual data. Peak positions, ω, and full width at half max, Γ, are indicated.

Ar annealing causes a downshift in G-band peak position (ω_G) of ~4 cm^{-1} and a FWHM (Γ_G) increase of ~11 cm^{-1}, both of which indicate that the Fermi level (E_F) shifts toward the charge neutral Dirac point energy (E_o).[4, 5, 24] We note that similar spectral changes have been observed even under milder Ar annealing temperatures of 393 K.[13] Both graphene and metallic carbon nanotubes are known to exhibit strong electron-phonon coupling (EPC) as E_F approaches E_o causing G-band to broaden due to this additional scattering process.[4-7, 23] A reduction in carrier concentration also causes the Fermi surface wavevector, k_F, to decrease and ω_G to soften by the Kohn anomaly condition $q = 2k_F$, with q being the wavevector of phonons susceptible to EPC. Both behaviors are understood to be symmetric about E_o (i.e. the values of ω_G and Γ_G are only dependent on doping magnitude, not type).[5] Recent electrical measurements have shown that graphene transistors in ambient air exhibit p-type doping.[25] In fact most, if not all, measurements reported to date require external gate potential to shift E_F to E_o.[4, 5] Raman, near-IR absorption, photoluminescence and electrical measurements and theoretical considerations on carbon nanotubes have shown the same p-type doping effects with O_2 specifically being considered as the cause.[17, 26-33] Therefore, we suspect the observed changes in the G-band upon Ar-annealing arise from a reduction in p-type doping by thermal removal of oxygen containing species from SLG. The spectral progression of S1 after exposure to pure O_2 supports this explanation since opposite behaviors in ω_G and Γ_G (i.e., upshifting and narrowing) are seen relative to Ar annealing.

Thermal desorption of other molecules could accompany removal of oxygen species when heating. Thus, the density of adsorbed oxygen-containing groups (and therefore p-type doping) after pure O_2 exposure may be greater since the surface is "cleaned" by Ar-annealing. The larger value of ω_G under O_2 with respect to as-prepared in air supports this idea. Our spectrometer resolution of ~0.5 cm^{-1} is not sufficient to resolve the difference in Γ_G between the two cases. The similar values arise possibly because SLG in both conditions is doped enough not to be significantly affected by Kohn anomaly-induced broadening (Γ_G values converge to ~8 cm^{-1} for $|E_F - E_o| >$ ~400meV).[5]

The FWHM of the 2D-band (Γ_{2D}) does not exhibit broadening due to EPC because the associated phonons are too high in energy.[5] This explains the relatively small differences in Γ_{2D} observed under the three conditions. On the other hand, this peak is still susceptible to frequency downshifts due to removal of p-type doping but, unlike ω_G, ω_{2D} remains approximately constant at 2682 cm^{-1}. Based on experimental report, we expect ω_{2D} to remain approximately constant between $E_F - E_o$ values of –200 meV and +400 meV and then begin to decrease with further n-type doping.[5] $E_F - E_o$ values up to –200 meV have been shown to be typical of air doping of carbon nanotubes.[34] This may explain why Ar annealing leaves ω_{2D} practically unchanged at ~2682 cm^{-1} even though it does lead to a Fermi level shift according to changes in the G-band. Only upon pure O_2 exposure after annealing does ω_{2D} finally increase indicating $E_F - E_o < -200$ meV. This provides additional evidence that Ar annealing may induce desorption of other molecules in addition to oxygen containing species, as mentioned above.

The details of the subsequent Ar-annealing cycle of O_2-exposed S1 (Ar annealed and exposed to O_2 prior to temperature dependence measurements) as well as of air-exposed sample, S2 (Ar annealed and exposed to air overnight prior to temperature dependence measurements), are now discussed. The values of ω_G, Γ_G, ω_{2D}, and Γ_{2D} during this annealing cycle are shown in Figure 5.2 for both samples. G-band trends upon heating are consistent with removal of oxygen species causing a loss in p-type doping as considered above. An interesting point to note is the difference in temperatures at which ω_G and Γ_G (of both samples) begin to follow their cooling curves. This may indicate that Γ_G provides a more sensitive measurement of doping. ω_{2D} does not show much difference between heating and cooling cycles because of the range of $E_F - E_o$

between ~ –200 meV and +400 meV where it is nearly independent of doping. Γ_{2D} stays within ~ 2 cm^{-1} while heating which, again, is because EPC does not affect Γ_{2D}. Explanations of intrinsic trends in ω_G, Γ_G, ω_{2D}, and Γ_{2D} during observed sample cooling are considered below. The two critical points that Figure 5.2 relays are: (1) ambient environment of SLG greatly affects sample doping level and must be taken into account not only in Raman investigations but also in electrical and optical studies where EPC and E_F position dictate many properties of interest and (2) upon cooling, values of ω_G, Γ_G, ω_{2D}, and Γ_{2D} all begin to converge implying that SLG becomes intrinsic after Ar annealing, independent of sample history (excluding intentional harsh oxidative or other covalent bond forming/breaking processes). This simple Ar annealing approach may be used to eliminate large variations in doping levels observed across as-prepared SLG samples.[11]

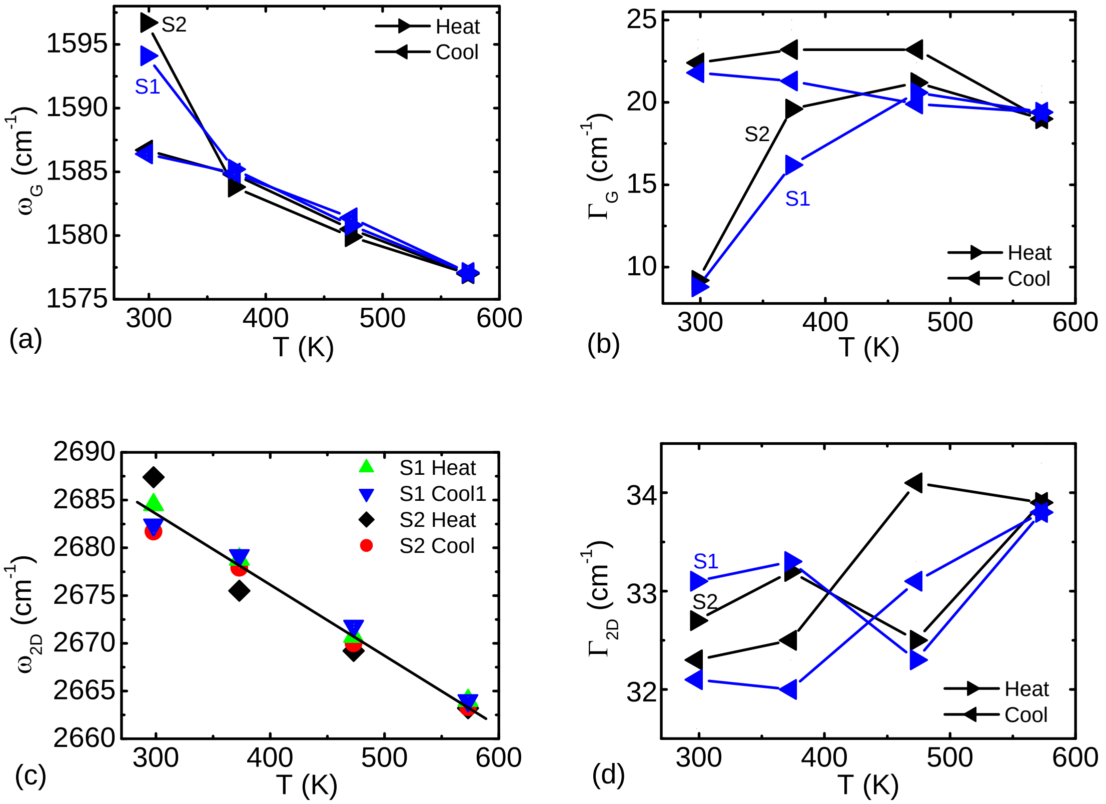

Figure 5.2. G-band and 2D-band peak frequencies (ω_G, ω_{2D}) and full width at half max values (Γ_G, Γ_{2D}) for O_2 exposed sample, S1, and air exposed sample, S2, during the first Ar-annealing cycle after doping. Initial data points prior to heating are taken under O_2 for S1 and air for S2 while all others are under Ar. Forward arrows indicate heating and reverse arrows indicate cooling in (a), (b), and (d). Line for ω_{2D} is a guide to the eye.

5.3 Intrinsic Behavior of Single-Layer Graphene Raman Features with Temperature

With initial complications of air environment on linewidths and frequencies defined, additional heating cycles under Ar were conducted to study the response of G- and 2D-band peaks of intrinsic SLG with temperature. The spectra for cooling during the very last Ar-annealing cycle of S2 are shown in Figure 5.3 as an example. Figure 5.4 shows the dependence of ω_G, Γ_G, ω_{2D}, and Γ_{2D} on temperature for S1 averaged over three sequential coolings (S2 shows the same behavior). Note that in Figure 5.1 $\Gamma_G = 19.6$ cm^{-1} for S1 after the first Ar annealing while Figure 5.4b shows it should be closer to 25.5 cm^{-1}. It is likely that S1 is not intrinsic after just one heating and cooling cycle. Therefore, only data taken after at least two complete cycles are considered here which seems to be enough to reach intrinsic behavior (i.e. overlapping data between cycles). $\omega_G(T)$ and $\omega_{2D}(T)$ in Figure 5.4 are fitted with linear relationships similar to Calizo *et al.*[35] (solid lines, black). A polynomial fit of $\omega_G(T)$ is also included (dashed line, blue) with fixed coefficients estimated from *ab initio* results of Bonini *et al.*[36] For the linear fit of $\omega_G(T)$, our values of slope and intercept are expectedly larger than those of ref. 35 owing to our investigation of temperatures above room temperature rather than below. For the polynomial fit, the only fitting parameter of ω_G at T = 0 K and direct use of fixed coefficients for graphene given in footnote 31 of ref. 36 give a reasonable agreement within ~ 2 cm^{-1}.

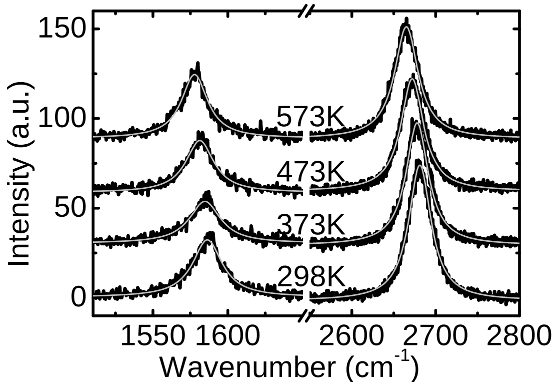

Figure 5.3. Progression of Raman spectrum with temperature while cooling during the last Ar-annealing cycle of sample S2. Lorentzian fits to each peak are in gray within actual data.

While Γ_{2D} increases with increasing temperature, Γ_G shows an unusual decrease with temperature. $\Gamma_G(T)$ is determined by the sum of electron-phonon ($\Gamma_G^{e\text{-}p}$) and phonon-phonon ($\Gamma_G^{p\text{-}p}$) contributions. $\Gamma_G^{p\text{-}p}$ is expected to vary by only ~0.5 cm^{-1} across the temperature range considered here[36] and has been fixed to equal 2 cm^{-1} for the subsequent analysis. $\Gamma_G^{e\text{-}p}$ is estimated following ref. 36 as,

$$\Gamma_G^{e-p}(T) = \left\{\Gamma_G^{e-p}(T=0)\right\} \times \left[f\left(-\frac{\hbar\omega_0}{2k_B T}\right) - f\left(\frac{\hbar\omega_0}{2k_B T}\right) \right] \qquad \text{Eq. 5.1}$$

where

$$\Gamma_G^{e-p}(T=0) = \frac{\sqrt{3}a_0^2\hbar^2}{4M\beta^2}\left\langle D_{E_{2G}}^2 \right\rangle_F \qquad \text{Eq. 5.2}$$

from ref. 37,

$$f(x) = [\exp(x)+1]^{-1} \qquad \text{Eq. 5.3}$$

is the Fermi-Dirac distribution, $a_0 = 2.46$ Å is the graphite lattice parameter, M is the mass of a carbon atom, $\beta = 5.52$Å·eV is the calculated slope of the electron dispersion at the **K**-point of the Brillouin zone, $\hbar\omega_0$ is the E_{2G} phonon energy, and $\left\langle D_{E_{2G}}^2 \right\rangle_F$ is the EPC matrix element for E_{2G} phonons. Thermal smearing of the electron energy distribution increasing population above and decreasing population below the Dirac point decreases Γ_G^{e-p} (and therefore Γ_G) with increasing temperature, which is observed in Figure 5.4b.

Data in Figure 5.4b is fitted using Eq. 5.1 plus a 2 cm^{-1} offset to take Γ_G^{p-p} into account. Here, $\hbar\omega_0$ is fixed at 196 meV for simplicity since it only changes by ~1.5 meV from 298K to 573K. Then the only fitting parameter is $\Gamma_G^{e-p}(T=0)$ and the best fit to the experimental data is obtained with $\Gamma_G^{e-p}(T=0) = 24.9$ cm^{-1} which is about a factor of 2 larger than the calculated value given in refs. 36 and 37. We note that $\left\langle D_{E_{2G}}^2 \right\rangle_F$ has been calculated by many groups[7, 37-43] and has been predicted to have values as low as 8.5 $eV^2/Å^2$, giving $\Gamma_G^{e-p}(T=0) = 2.1$ cm^{-1}, and as high as 86 $eV^2/Å^2$, giving $\Gamma_G^{e-p}(T=0) = 20.7$ cm^{-1}. Given the amount of uncertainty in this value, in addition to possible variations in β, we believe our obtained fitting parameter $\Gamma_G^{e-p}(T=0) = 24.9$ cm^{-1} is reasonable.

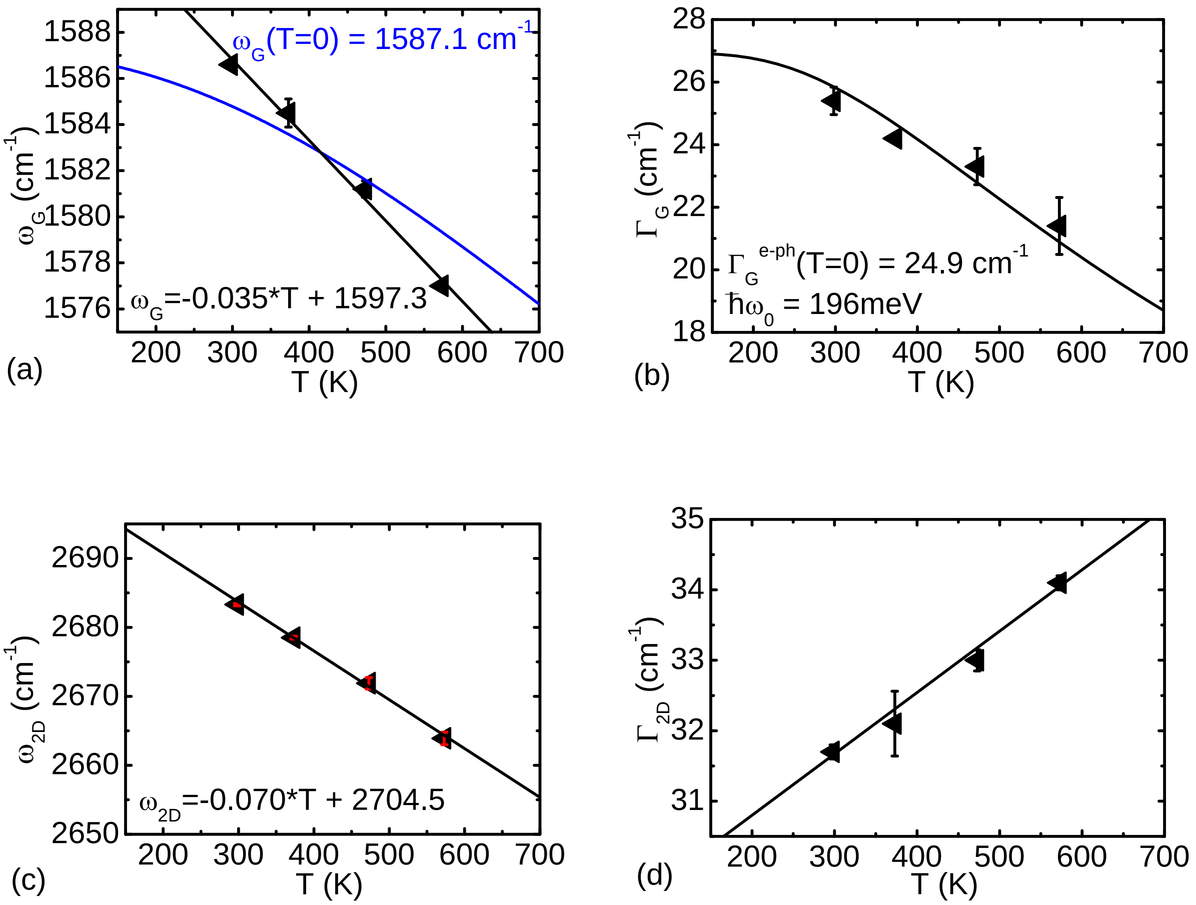

Figure 5.4. Temperature dependence of ω_G, Γ_G, ω_{2D}, and Γ_{2D} of sample S1 after minimizing effects of air ambient by Ar annealing. $\omega_G(T)$ and $\omega_{2D}(T)$ are fitted to a linear relationship (solid lines, black) as in ref. 35 and a polynomial fit (dashed line, blue) for $\omega_G(T)$ is also included as in ref. 36. Γ_G is fitted to $\Gamma_G^{e\text{-}p}(T) + 2$ cm^{-1}, as described in the text, while the line for Γ_{2D} is simply a guide to the eye. Data points in each plot are an average of three cooling cycles with standard deviation as error bars.

5.4 Conclusion

To summarize, we have described the p-type doping effect that ambient O_2 has on the Raman spectrum of air-exposed single-layer graphene suggesting graphene is highly sensitive to doping via adsorption. The ability to remove these environmental effects has allowed for the direct experimental observation of temperature enhanced reduction of EPC in intrinsic graphene due to electron energy smearing leading to decreasing G-band phonon mode linewidth with increasing temperature. Both ambient air doping and the temperature effects on Raman spectra have been explained within the context of the strong EPC near the Dirac point.

5.5 References

[1] Abdula, D.; Ozel, T.; Kang, K.; Cahill, D. G.; Shim, M. *J. Phys. Chem. C* **2008**, *112,* 20131.

[2] Du, X.; Skachko, I.; Barker, A.; Andrei, E.Y. *Nat. Nanotech.* **2008**, *3*, 491.

[3] Morozov, S. V.; Novoselov, N. S.; Katsnelson, M. I.; Schedin, F.; Elias, D. C.; Jaszczak, J. A.; Geim, A. K. *Phys. Rev. Lett.* **2008**, *100*, 016602.

[4] Pisana, S.; Lazzeri, M.; Casiraghi, C.; Novoselov, K.; Geim, A. K.; Ferrari, A. C.; Mauri, F. *Nat. Mater.* **2007**, *6*, 198.

[5] Das, A. et al. *Nat. Nanotech.* **2008**, *3*, 210.

[6] Lazzeri, M.; Mauri, *Phys. Rev. Lett.* **2006**, *97*, 266407.

[7] Piscanec, S.; Lazzeri, M.; Mauri, F.; Ferrari, A. C.; Robertson, J. *Phys. Rev. Lett.* **2004**, *93*, 185503.

[8] Maultzsch, J.; Reich, S.; Thomsen, C.; Requardt, H.; Ordejón, P. *Phys. Rev. Lett.* **2004**, *92*, 075501.

[9] Wehling, T.O.; Novoselov, K. S.; Morozov, S. V.; Vdovin, E. E.; Katsnelson, M. I.; Geim, A. K.; Lichtenstein, A. I. *Nano Lett.* **2008**, *8*, 173.

[10] Schedin, F.; Geim, A. K.; Morozov, S. V.; Hill, E. W.; Blake, P.; Katsnelson, M. I.; Novoselov, K. S. *Nat. Mater.* **2007**, *6*, 652.

[11] Casiraghi, C.; Pisana, S.; Novoselov, K. S.; Geim, A. K.; Ferrari, A. C. *Appl. Phys. Lett.* **2007**, *91*, 233108.

[12] Liu, L.; Ryu, S.; Tomasik, M. R.; Stolyarova, E.; Jung, N.; Hybertsen, M. S.; Steigerwald, M. L.; Brus, L. E.; Flynn, G. W. *Nano Lett.* **2008**, *8*, 1965.

[13] Haluska, M. et al. *Phys. Stat. Sol. (b)* **2007**, *244*, 4143.

[14] Gaur, A.; Shim, M. *Phys. Rev. B* **2008**, *78*, 125422.

[15] Heinze, S.; Tersoff, J.; Martel, R.; Derycke, V.; Appenzeller, J.; Avouris, Ph. *Phys. Rev. Lett.* **2002**, *89*, 6801.

[16] Shim, M; Siddons, G. P. *Appl. Phys. Lett.* **2003**, *83*, 3564.

[17] Dukovic, G.; White, B. E.; Zhou, Z.; Wang, F.; Jockusch, S.; Steigerwald, M. L.; Heinz, T. F.; Friesner, R. A.; Turro, N. J.; Brus, L. E. *J. Am. Chem. Soc.* **2004**, *126*, 15269.

[18] Nguyen, K. T.; Gaur, A.; Shim, M. *Phys. Rev. Lett.* **2007**, *98*, 145504.

[19] Novoselov, K. S.; Jiang, D.; Schedin, F.; Booth, T. J.; Khotkevich, V. V.; Morozov, S. V.; Geim, A. K. *Proc. Natl. Acad. Sci. U.S.A.* **2005**, *102*, 10451.

[20] Zhang, Y. B.; Tan, Y. W.; Stormer, H. L.; Kim, P. *Nature* **2005**, *438*, 201.

[21] Bunch, J. S.; van der Zande, A. M.; Verbridge, S. S.; Frank, I. W.; Tanenbaum, D. M.; Parpia, J. M.; Craighead, H. G.; McEuen, P. L. *Science* **2007**, *315*, 490.

[22] Graf, D.; Molitor, F.; Ensslin, K.; Stampfer, C.; Jungen, A.; Hierold, C.; Wirtz, L. *Nano Lett.* **2007**, *7*, 238.

[23] Ferrari, A. C. *Solid State Comm.* **2007**, *143*, 47.

[24] Yan, J.; Zhang, Y.; Kim, P.; Pinczuk, A. *Phys. Rev. Lett.* **2007**, *98*, 166802.

[25] Romero, H. E.; Shen, N.; Joshi, P.; Gutierrez, H. R.; Tadigadapa, S. A.; Sofo, J. O.; Eklund, P. C. *doi:10.1021/nn800354m*.

[26] Collins, P. G.; Bradley, K.; Ishigami, M.; Zettl, A. *Science* **2000**, *287*, 1801.

[27] Sumanasekera, G. U.; Adu, C. K. W.; Fang, S.; Eklund, P. C. *Phys. Rev. Lett.* **2000**, *85*, 1096.

[28] Shim, M.; Back, J. H.; Ozel, T.; Kwon, K.-W. *Phys. Rev. B* **2005**, *71*, 205411.

[29] Strano, M.S. et al. *J. Phys. Chem. B* **2003**, *107*, 6979.

[30] O'Connell, M. J. et al. *Science* **2002**, *297*, 593.

[31] Jhi, S. H.; Louie, S. G.; Cohen, M. L. *Phys. Rev. Lett.* **2000**, *85*, 1710.

[32] Sumanasekera, G. U.; Adu, C. K. W.; Fang, S.; Eklund, P. C. *Phys. Rev. Lett.* **2000**, *85*, 1096.

[33] Froudakis, G. E.; Schnell, M.; Muhlhauser, M.; Peyerimhoff, S. D.; Andriotis, A. N.; Menon, M.; Sheetz, *R. M. Phys. Rev. B* **2003**, *68*, 115435.

[34] Shim, M.; Gaur, A.; Nguyen, K. T.; Abdula, D.; Ozel, T. *J. Phys. Chem. C* **2008**, *112*, 13071.

[35] Calizo, I.; Miao, F.; Bao, W.; Lau, C. N.; Balandin, A. A. *Appl. Phys. Lett.* **2007**, *91*, 071913.

[36] Bonini, N.; Lazzeri, M.; Marzari, N.; Mauri, F. *Phys. Rev. Lett.* **2007**, *99*, 176802.

[37] Lazzeri, M.; Piscanec, S.; Mauri, F.; Ferrari, A. C.; Robertson, J. *Phys. Rev. B* **2006**, *73*, 155426.

[38] Piscanec, S.; Lazzeri, M.; Robertson, J.; Ferrari, A. C.; Mauri, F. *Phys. Rev. B* **2007**, *75*, 035427.

[39] Mahan, G. D. *Phys. Rev. B* **2003**, *68*, 125409.

[40] Park, J. Y.; Rosenblatt, S.; Yaish, Y.; Sazonova, V.; Ustunel, H.; Braig, S.; Arias, T. A.; Brouwer, P. W.; McEuen, P. L. *Nano Lett.* **2004**, *4*, 517.

[50] Jiang, J.; Saito, R.; Gruneis, A.; Dresselhaus, G.; Dresselhaus, M. S. *Chem. Phys. Lett.* **2004**, *392*, 383.

[51] Perebeinos, V.; Tersoff, J.; Avouris, P. *Phys. Rev. Lett.* **2005**, *94*, 086802.

[52] Koswatta, S.; Hasan, S.; Lundstrom, M. S.; Anantram, M. P.; Nikonov, D. E. *cond-mat/0511723*.

CHAPTER 6

FUNCTIONAL CHEMISTRY ROUTE TO CARBON NANOTUBE DIODES AND PHOTOVOLTAICS

In this chapter we utilize the fact that sp^2-bonded carbon nanostructures can be readily doped to manifest an operating single semiconducting carbon nanotube diode. N-type and p-type doping via charge transfer from adsorbed molecules is described. Both electrical performance as well as photovoltaic light response is characterized. This work has been published in Ref. [1].

6.1 Introduction

High performance cost-efficient computing, communication, and energy harvesting systems are among many improvements anticipated by incorporating nanoscale materials into electronics and photovoltaics. Due to their unique electronic properties, as discussed in Chapter 2, carbon nanotubes have been at the forefront in the development of next generation electronic devices[2-5]. The p-n diode is arguably the most pivotal electronic and photovoltaic device. However, theoretical studies have had mixed conclusions on how well a carbon nanotube would perform as the active element in a diode[6, 7] with one of the key issues being Zener breakdown caused by small depletion width within the nanotube. Experimentally, this has been averted by implementing an intrinsic region to separate heavily doped regions resulting in a p-i-n structure.[8-11] A major drawback of these p-i-n devices lies in the dual-gate geometry for electrostatic doping which requires cumbersome device fabrication and unnecessarily adds two more terminals to one of the simplest circuit elements. Furthermore, the addition of the intrinsic region degrades device performance by possibly uncovering carrier trap sites (and therefore sometimes requiring further fabrication steps to suspend the active area above the substrate) as well as increasing the series resistance. Chemical doping has been another approach where p-doping of nanotubes by ambient air[12-15] is preserved with a polymethylmethacrylate (PMMA) protecting layer over half of the device channel while potassium[16] converts the other half n-type[17]. A leaky diode behavior results in this case due to the degenerate doping from such a low work function metal. Such a device also has to be kept under vacuum to maintain the n-doped region. Replacing potassium with small amine molecules can maintain rectifying behavior but only a p-p^- junction has been achieved.[18] Intratube p-n diodes have also been fabricated using nanotubes partially impregnated with Fe atoms during chemical vapor deposition with ferrocene,[19] but this process lacks the precise spatial control over defining doped regions which may lead to low yields of functional devices.

Here, we fabricate single semiconducting carbon nanotube p-n diodes by simple patterning of polymers using conventional lithography. Spatial doping modulation is achieved by deep UV lithography of PMMA containing tetracyanoquinodimethane (TCNQ) followed by spin casting polyethylenimine (PEI). Half of the channel covered by PMMA/TCNQ enhances p-type character[20] while the PEI covered region becomes air-stable n-type[21]. These devices do not make use of an artificial intrinsic region and are entirely on substrate with a simple two terminal geometry. We show that they are high quality, low-leakage diodes. Doping levels and spatial doping profiles and their effects on diode performance are examined by a combination of Raman and electrochemical gating measurements. Finally, we present our initial studies on photovoltaic response of these intratube p-n diodes.

6.2 Methods

Devices were fabricated on pre-annealed single-crystal AT-cut quartz wafers for aligned nanotube growth, as discussed in Chapter 2. Ferritin catalyst with CH_4/H_2 CVD method was used for growth and devices with one semiconducting carbon nanotube spanning ~55μm channel lengths were made, according to details in Chapter 2. All devices were annealed in 150 sccm Ar flow at 300°C for 1 hour prior to measurements to ensure symmetric I_{DS}-V_{DS} characteristics before p-n junction fabrication. Polymethylmethacrylate (PMMA) with 0.03wt% tetracyanoquinodimethane (TCNQ) was used to define p-region and neat polyethylenimine (PEI, M.W. ~25,000 daltons, Aldrich) was used for n-region. First, PMMA/TCNQ was spin coated at 3000 rpm for 60s. Standard deep UV lithography was carried out to open a window over half of the channel. Then PEI was spin cast on the device at 3000 rpm for 2min. For electrochemical gating measurements, a solution of 30wt% PEI and $LiClO_4 \cdot 3H_2O$ (4:1 PEI: $LiClO_4 \cdot 3H_2O$ by weight) in methanol was used instead of neat PEI.

Electrical measurements were conducted with an Agilent 4156C semiconductor parameter analyzer. Raman data were collected using a Jobin Yvon LabRam HR 800 micro-Raman with a 633nm laser excitation and a 100x air objective providing a spot size of ~1µm. Raman signals from polymer films are removed using background spectra taken where there is no nanotube present. Scanning electron microscope images were obtained on a Hitachi 4700 SEM operating at 1kV accelerating voltage. Imaging was done prior to electrical measurements to identify connected devices while Raman spectroscopy was used to verify electron-beam induced damage was negligible.

6.3 Dark Current Characteristics

The progression of I_{DS}-V_{DS} behavior at each step of fabrication for a representative device is shown in Figure 6.1 along with schematics of the device geometry. After Ar annealing of as-fabricated device (geometry I), I_{DS}-V_{DS} characteristics is symmetric which ensures that changes in the electrical behavior are due to intentional doping. The onset of current rectification at negative voltages is already achieved in device geometry II even without PEI which indicates that PMMA/TCNQ dopes nanotubes more p-type than air, in accordance with the direction of applied bias. After application of PEI, significantly better diode behavior results. Important to note is that we do not see the onset of Zener breakdown as Zhou, et al., have[17] with a potassium-doped abrupt p^+-n^+ junction where I_{DS}-V_{DS} becomes nearly ohmic. Our diodes show a reverse current that is 3 orders of magnitude smaller than the forward current when biased at the sweep extrema indicating that we are close to the standard p-n doping profile.

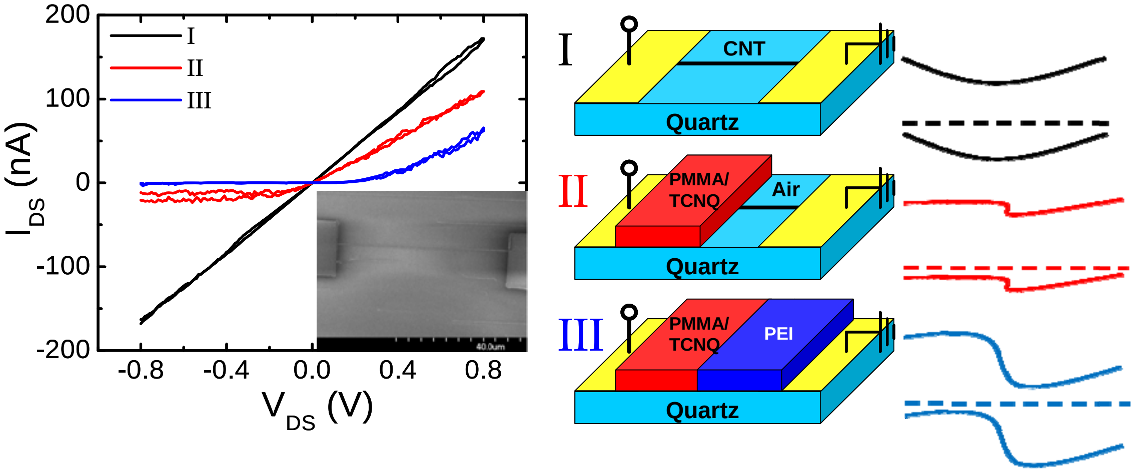

Figure 6.1. I_{DS}-V_{DS} characteristics and probable band diagrams at three stages of device fabrication: (I) initial, (II) nanotube protected with PMMA/TCNQ over half the channel and exposed to air on the other half, and (III) completed diode with PEI filling the patterned window. Voltage is always applied on the PMMA/TCNQ side. Both forward and reverse sweeps are shown. Inset is an SEM image of the device in stage I.

To characterize the performance of the devices, we fit our data to a modified Shockley equation with a series resistance, R_s, similar to Lee et al.[9] and Bosnick et al.[11]:

$$I_{DS} = I_R \left\{ \exp\left[\frac{q(V_{DS} - IR_s)}{nk_BT} \right] - 1 \right\} \qquad \text{Eq. 6.1.}$$

I_R is the ideal diode leakage current, q is the electric charge, and k_BT is the thermal energy. The ideality factor, n, is a measure of carrier generation and recombination from trap sites within the depletion region and takes on values between 1 and 2 with larger values being when trap-mediated generation-recombination current becomes dominant.

Figure 6.2 shows the fitting results for three devices. A small drawback to using polymers as dopants is their slight conductivity and/or charging which can lead to non-negligible hysteresis at small current levels. Because of this hysteresis, we fit only the data in the voltage range where nanotube conductivity is predominant. With the exception of device 2 which contains electrolyte dissolved in PEI, I_{DS} down to a few pA can be analyzed reliably without complications from the hysteresis. Both the forward and the reverse voltage sweeps are shown in Figures 6.1 and 6.2 to confirm that the hysteresis does not degrade overall performance.

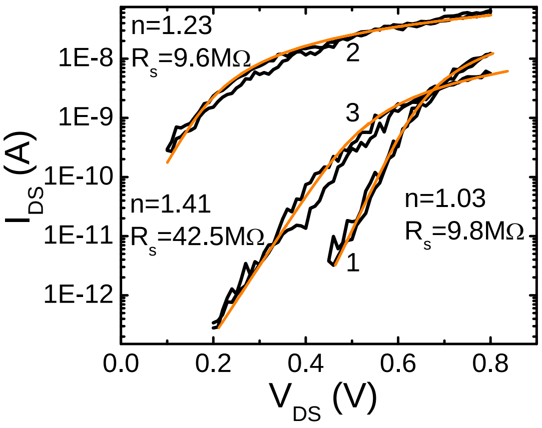

Figure 6.2. Forward bias current and curve fits for three different devices (labeled 1, 2, and 3) having a range of performance parameters. Device 2 has electrolyte in the PEI defined n-region which may be the reason for its higher leakage current. Both forward and reverse sweeps are shown.

As the fitting parameters suggest, fabrication of a nearly ideal, on-substrate, two-terminal diode without the intentional use of an intrinsic region is possible. This region has previously been deemed necessary[11] to prevent Zener breakdown[17] due to the small depletion widths expected in abrupt intratube p-n junctions[6]. The absence of this region is expected to decrease R_s and reduce the number of viable defect states that would otherwise increase n. Both devices 1 and 2 show nearly ideal behavior with R_s being only about half of that observed in p-i-n diodes of Ref. 9 and close to that of p-i-n diodes in Ref. 11. Note that our diodes have much longer channel lengths (~20 times or more) than devices in Refs 9 and 11. Scaled to same lengths, we expect about an order of magnitude decrease in the series resistance. The larger series resistance of device 3 is a consequence of the extent of doping which is explained later.

In addition to simplicity in fabrication, an advantage of using PEI to achieve n-type character is the stability in air. Potassium-doped devices must be kept under vacuum due to the small work function of the alkali metal.[17] Fe-filled carbon nanotube diodes have been shown to be air stable, but the lack of spatial control over doping may lead to low yields of working p-n junctions.[19] Of the 10 single tube p-n diodes fabricated by photo-patterning of polymers, all have shown rectifying behavior. Figure 6.3 shows the electrical behavior of diode 3 immediately after fabrication as well as after 1 month in ambient air. The increase in the forward bias current may indicate that the device improves over time, but the reverse current also increases slightly. One probable cause of this may be PEI diffusion into the PMMA/TCNQ region which grades the junction causing I_{DS}-V_{DS} to look increasingly more ohmic. The ability to cross-link PEI[22] can possibly improve stability. Nevertheless, the diode still shows rectifying behavior even after such a long time in air.

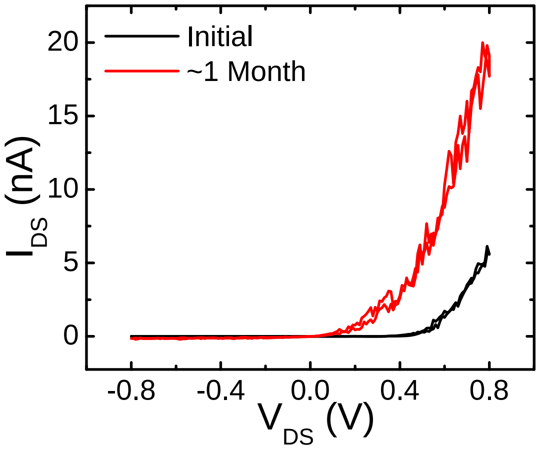

Figure 6.3. Changes in electrical behavior of device 3 after 1 month in ambient air. Forward and reverse sweeps are shown for both cases.

6.4 Doping Profile and Degree of Doping on Diode Performance

In addition to electrical measurements, Raman spectroscopy has been one of the key approaches to studying charge transfer/doping in carbon nanotubes[23-27]. In the limit of low doping levels, both p- and n-doping leads to an essentially symmetric upshift in the G-band LO phonon peak positions (ω_{G+}).[28, 29] That is, when the Fermi level moves toward either the valence or the conduction band edge, ω_{G+} increases symmetrically from a minimum value $\omega_{G+}^{(0)}$ (which occurs precisely at mid-gap). A spatial profile of the change in ω_{G+} ($\Delta\omega_{G+}$) around the depletion region of device 2 is shown in Figure 6.4a. Here, $\Delta\omega_{G+} = \omega_{G+}$(geometry III) – ω_{G+}(geometry I), where the device geometries correspond to schematics in Figure 6.1. Prior to any polymer patterning (geometry I), ω_{G+} is nearly constant at ~1589 cm^{-1} in this region of the nanotube. The charge neutral line is placed where the minimum in $\Delta\omega_{G+}$ appears (i.e. where $\omega_{G+}^{(0)}$ is). At this point $\Delta\omega_{G+} = -1$ cm^{-1} and therefore the initial ω_{G+} is only 1 cm^{-1} higher than $\omega_{G+}^{(0)}$ indicating that this nanotube begins as nearly intrinsic. Upon polymer patterning to define the p-n junction, there is about 8 cm^{-1} upshift with respect to $\omega_{G+}^{(0)}$ on the PMMA/TCNQ side (p-region) indicating that the tube is doped significantly more p-type than in air. This difference in doping leads to p-i junction for the device having geometry II and explains the rectifying behavior even without PEI as observed in Figure 6.1. The PEI covered side (n-region) of the nanotube also exhibits an upshift in ω_{G+} (~5 cm^{-1} with respect to $\omega_{G+}^{(0)}$). Larger $\Delta\omega_{G+}$ on the p-region indicates that the amount of p-doping by PMMA/TCNQ is somewhat larger than that of n-doping by PEI. The junction is also easily identified by the sudden discontinuity in the FWHM due to doping, as shown in Figure 6.4b.

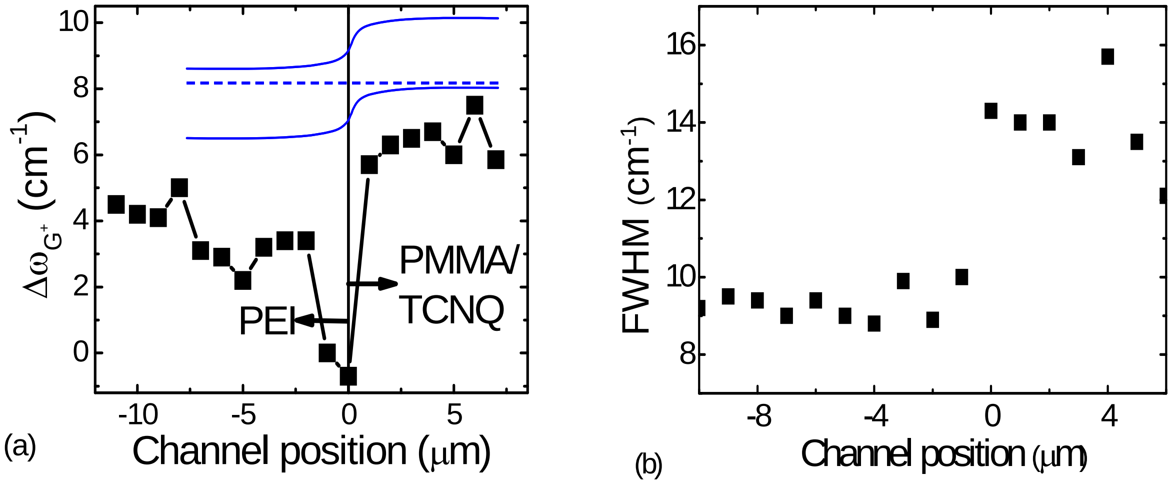

Figure 6.4. (a) Change in the G-band LO phonon position ($\Delta\omega_{G+}$) of device 2 along the nanotube length around the junction. The vertical line represents the charge neutral point where $E_F = (E_c–E_v)/2$. The inset is a schematic band diagram showing the doping profile of the device according to the observed $\Delta\omega_{G+}$. (b) Spatial profile of the full-width-at-half-maximum of the G-band peak.

The Raman spectra of p- and n-regions of all three devices in Figure 6.2 are shown in Figure 6.5a. Device 3 which has the lowest performance (i.e. ideality factor $n = 1.41$ and large series resistance $R_s = 42.5$ MΩ) exhibits the smallest changes in ω_{G+} with respect to $\omega_{G+}^{(0)}$ (assuming $\omega_{G+}^{(0)}$ to be the same for all three tubes – this assumption is justified given Ref. 30 where $\omega_{G+}^{(0)}$ has been shown to be independent of diameter for semiconducting tubes). Following

Ref. 28, $\Delta\omega_{G+}^{n}$ ($\Delta\omega_{G+}^{p}$), the G$^+$ peak spectral shift with respect to $\omega_{G+}^{(0)}$ for the n-region (p-region), should scale as n_n^3 (p_p^3) in the low doping regime. n_n and p_p are the majority carrier densities. Device 3, then, has the lowest overall doping level with both p- and n-regions closer to being intrinsic than the other two devices. This leads to a larger series resistance as observed. We also expect less ideal diode behavior for device 3 since low majority carrier density will cause larger depletion widths (W) which in turn leads to larger trap-mediated generation-recombination current (i.e. the trap generation-recombination current is proportional to W, see Eq. 6.2 below). According to Ref. 6, $W \propto \exp(C/\rho)$ for a symmetric p-n junction ($n_n = p_p \propto \rho$), with doping fraction ρ and constant C. We define an average G$^+$ peak position shift as $\Delta\overline{\omega}_{G+} = (\Delta\omega_{G+}^{n} + \Delta\omega_{G+}^{p})/2$ and note $\Delta\overline{\omega}_{G+} \propto \rho^3$ from the cubic relation described above, leading to $\ln(W) \propto (\Delta\overline{\omega}_{G+})^{-1/3}$. The decreasing ideality factor n with $\Delta\overline{\omega}_{G+}$ shown in Figure 6.5b may then be explained by larger doping levels causing smaller W which in turn decrease trap-mediated generation-recombination current.

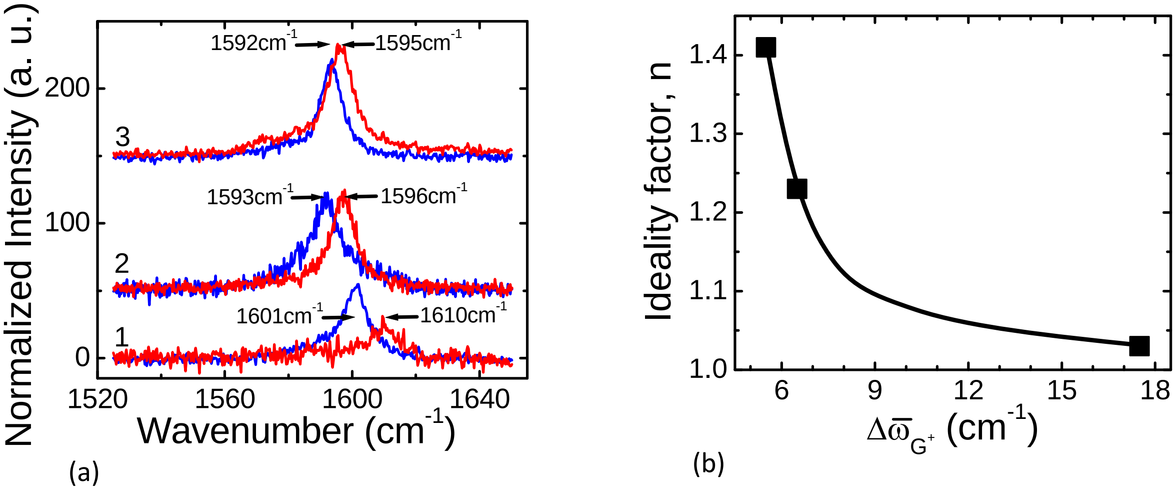

Figure 6.5. (a) Raman G-band spectra of the p-region (red) and n-region (blue) of the three diodes from Figure 2. Arrows point to ω_{G+} frequencies at the maxima. (b) Device performance dependence on Raman G$^+$ peak shift for the same three devices. The ideality factor, *n*, depends on the degree of doping on each side of the junction, the average of which is represented by $\Delta\overline{\omega}_{G+}$. The line is a guide to the eye.

To further investigate the extent of n-doping and its effects on device performance, we have electrochemically gated the PEI/electrolyte region of device 2. We first discuss reverse-bias regime. Figure 6.6 shows the reverse current, I_o, for varying gate potential on the PEI side, V_g^{PEI}. I_o is given by[31]:

$$I_o = qA\left(\sqrt{\frac{D_p}{\tau_\mathrm{p}}}\frac{n_i^2}{n_n} + \sqrt{\frac{D_n}{\tau_\mathrm{n}}}\frac{n_i^2}{p_p} + \frac{n_i W}{\tau_g}\right) \qquad \text{Eq. 6.2.}$$

with cross-sectional area A, minority carrier diffusion coefficients D_n and D_p, lifetimes τ_p and τ_n, generation lifetime τ_g, and intrinsic carrier concentration n_i. Note that I_o is different from I_R in Eq. 6.1 since the third term describing trap-mediated generation current in the depletion region gets incorporated into the ideality factor in Eq. 6.1. The first two terms are the ideal reverse-bias saturation current (I_R in Eq. 6.1). At constant temperature and bandgap (i.e. constant n_i), increasing the doping level of n- or p- or both regions should lead to a smaller I_o since n_n and/or p_p will increase and W will decrease. However, Figure 6.6 shows that I_o actually increases with n-region doping level (from V_g^{PEI}= –200 to +800 mV). Different behavior at V_g^{PEI} = –800 mV is the expected leaky diode behavior of a p-i (or p-p$^-$) junction. Assuming diffusion coefficients and lifetimes remain constant, the only reason I_o would increase with doping level is if n_i increased. At a fixed temperature, n_i becomes larger only if the band gap becomes smaller. A similar trend of increasing I_o with doping has been observed with the dual-gate diodes and has been attributed to band gap renormalization (BGR)[10]. BGR is the reduction of the band gap at high doping fractions of a semiconductor due to many-body interactions.[32] We can estimate the ratio of reverse-bias saturation currents at two different V_g^{PEI} values V_{g1} and V_{g2} as: $I_o(V_{g1})/I_o(V_{g2}) \approx \exp\{[E_a(V_{g2}) - E_a(V_{g1})]/k_BT\}$ where E_a is the activation energy for minority carrier formation outside of W as described by Lee.[10] Then, we obtain an E_a difference $[E_a(V_{g2}) - E_a(V_{g1})]$ of ~0.02 eV for V_g^{PEI} = 200 and 800mV which is very similar to that seen for dual back-gate voltages of 5 and 7 V reported in Ref. 10. The smaller gate voltage range needed here is due to the higher efficiency of polymer electrochemical gating.[33, 34] These results further support the idea of BGR affecting intratube p-n diode operation.

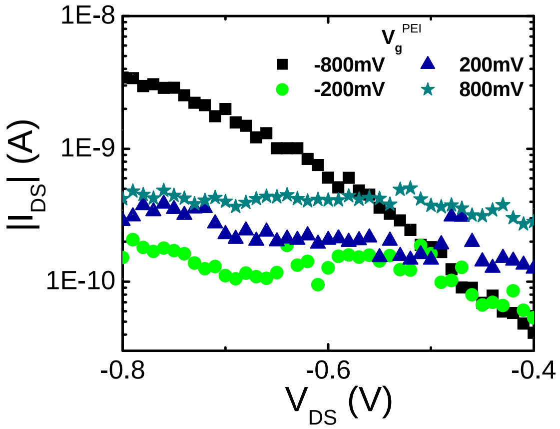

Figure 6.6. Magnitude of reverse currents for multiple gating potentials on the n-region, V_g^{PEI}, as indicated. Hystereses in each curve within the voltage range shown were negligible and the forward and reverse sweeps were averaged for clarity.

Figure 6.7 shows how the series resistance and ideality factor depend on the electrochemical gate potential applied to the n-region of device 2. Curve fitting to obtain n and R_s is carried out in the same manner as described for devices in Figure 6.1. The largest value of R_s is seen at $V_G^{PEI} = -500$ mV. We expect the highest resistance when a p-i doping profile is achieved since the “depletion width” is about the size of the entire, highly resistive, intrinsic region. That is, at $V_G^{PEI} = -500$ mV, we completely remove all doping on this side. A Fermi level shift of ~500 mV by PEI doping is consistent with Refs. 34 and 35. As a more positive V_G^{PEI} increases carrier density in the n-region, W decreases which in turn decreases R_s as observed. At a more negative gate voltage of –800 mV, the n-region is now converted to slightly p-type leading again to lower R_s values but at the price of leaky p-p$^-$ junction behavior consistent with the observed reverse current in Figure 6.6. The PEI/electrolyte gate dependence of n shows a minimum value at $V_G^{PEI} = -200$ mV (i.e. about 300 mV above the middle of the band gap inferred from the R_s maximum at –500 mV). As the electrochemical gate potential places the Fermi level at or below the midgap, less ideal diode behavior is expected as p-i or p-p$^-$ junctions are formed and is reflected by the increasing n value for $V_G^{PEI} < -200$ mV. The increasing n for $V_G^{PEI} > -200$ mV may be affected by BGR. The overall gate dependence of n suggests that optimized doping levels may provide ideal behavior even for diodes such as device 3 with large initial n and R_s.

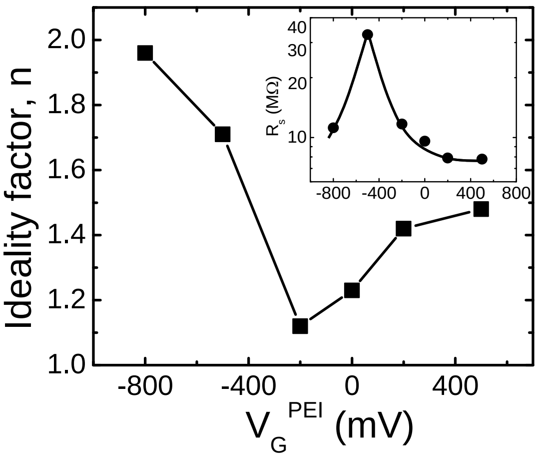

Figure 6.7. Ideality factor and series resistance (inset) dependences on V_G^{PEI} for device 2. Lines are guides to the eye.

6.5 Photovoltaic Response

We now discuss the photovoltaic response of the polymer patterned intratube diodes. The laser from the Raman spectrometer has been used here as the excitation source. This allows a simultaneous measurement of the Raman G-band map (top image in Figure 6.8) and spatially resolved photoresponse. When the depletion region is excited, the photo-generated electrons and holes are separated by the electric field of the junction which causes an increase in the reverse current. In Figure 6.8, a sharp increase in the reverse current is seen only at the channel position around 28 μm where the depletion region is located. Photocurrent due to excitation in the doped regions away from the junction is only ~20 pA and is expectedly smaller than reported photocurrent in un-doped carbon nanotubes.[36]

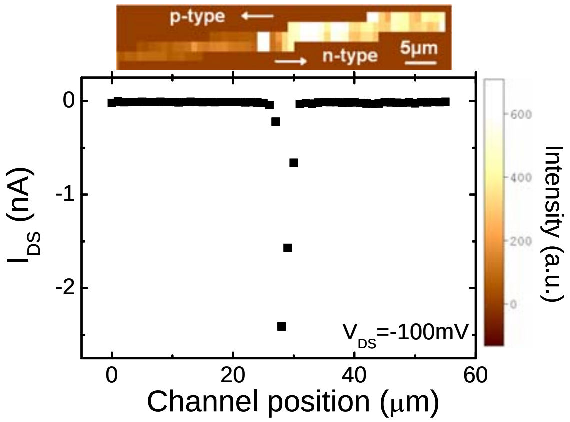

Figure 6.8. Response of reverse current to 0.44MW/cm^2 633nm excitation for device 2 as the laser (~1µm spot size) is scanned along the channel of the diode. The Raman intensity spatial map (above) is scaled 1:1 on the position axis of the figure. Lower intensity for the p-type region is primarily due to photon scattering through both PEI and the protecting PMMA/TCNQ layer underneath while the laser is only scattered through PEI on the n-type side.

The I_{DS}-V_{DS} response to photoexcitation at the diode junction is shown in Figure 6.9a. An open circuit voltage (V_{oc}) of 205 mV and a short circuit current (I_{sc}) of 1.4 nA are observed at both laser intensities used. In the limit of low photo-generated carrier densities, I_{sc} is expected to scale linearly with the excitation intensity.[9] The same I_{DS}-V_{DS} characteristics at the two intensities indicate that we are in the high intensity (saturation) regime. Although we cannot measure efficiency in this regime, the maximum power and the fill factor for this intratube p-n diode can be determined. The power square region is enlarged for the higher intensity excitation response along with the corresponding power in Figure 5.9b. The maximum power this nanotube diode can provide is about 0.14 nW. The fill factor of the power square is a measure of how well V_{oc} and I_{sc} translate to power output and is calculated as $FF = (I_M V_M)/I_{sc}V_{oc} = 0.498$ for this device. While I_{sc} and power cannot be compared directly, FF obtained here is in the upper end of the range reported for suspended dual-gate diodes with similar V_{oc}.[9] Further studies are underway to better quantify photovoltaic properties.

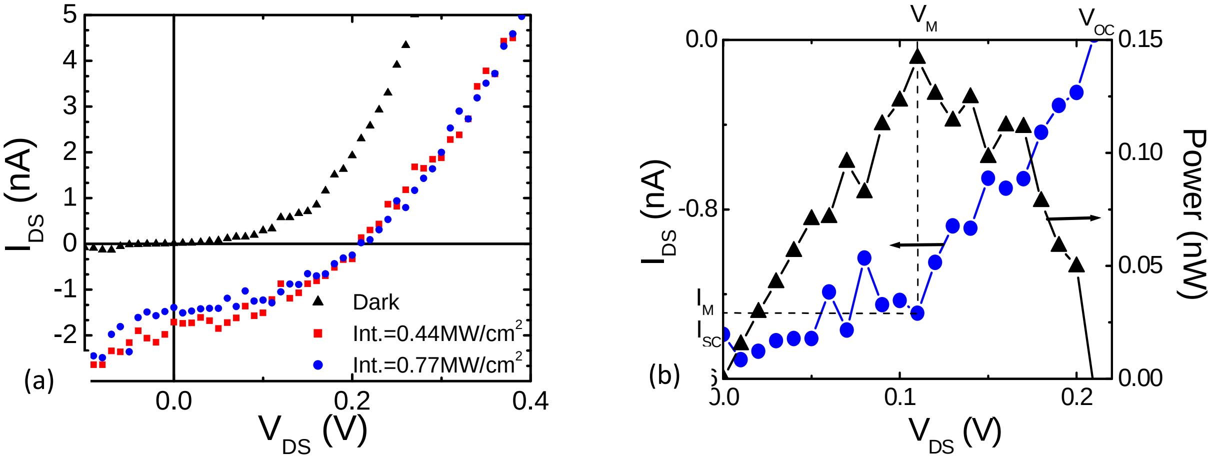

Figure 6.9. (a) Photovoltaic response of device 2 under laser (633 nm) excitation at the p-n junction. Hysteresis is negligible at this scale and therefore, the forward and reverse sweeps have been averaged for clarity. (b) Close-up of I_{DS} in the power square region for laser intensity 0.77MW/cm^2 (left axis). Power = $|I_{DS} \times V_{DS}|$ is plotted on the right axis. V_M and I_M are the diode voltage and current values at maximum power. I_{sc} and V_{oc} are short circuit current and open circuit voltage.

6.6 Reverse Bias Light Response

Figure 6.10 shows the reverse-bias region of the I_{DS}-V_{DS} behavior for the same device as in Figure 6.9. The response to light is unusual in that the current continues to increase with increasing reverse bias. Typically, light induces a constant addition in carrier concentration due to photoexcitation which, itself, provides a constant increase in current which is independent of bias. A possible explanation of this phenomenon is multiple carrier generation through impact excitation at high bias which has been observed in p-i-n structures.[37] The concept suggests that, with photon energies high enough for E_{22} excitations, carriers can gain enough kinetic energy within the depletion region for impact excitation of additional carriers which occurs at reverse bias voltage steps equal to the bandgap energy. Figure 6.10 shows there is a possible step around V= -0.2 V which begins to level off around V= -0.6 V. These steps have been shown to arise only at low temperature (<100 K) and begin becoming less discrete with increasing temperature. Since our device geometry should provide a significantly smaller depletion region width relative to those in Ref. 37 (~700 nm), low temperature may not be required for us to observe these current steps because the carriers gain sufficient kinetic energy for impact excitation long before they can scatter with phonons. We also do not see the expected multiple steps in our data. Our I_{DS}-V_{DS} behavior is actually very similar to that of p-i-n diodes when the excitation energy is just approximately equal twice the bandgap energy.[37] It is highly probable the same scenario is occurring with our device as it is Raman resonant meaning our laser energy is equal to a transition between van Hove singularities, probably E_{22} according to the Kataura plot. Therefore, multiple carrier generation seems to be feasible in our polymer-doped carbon nanotube diodes, even at room temperature.

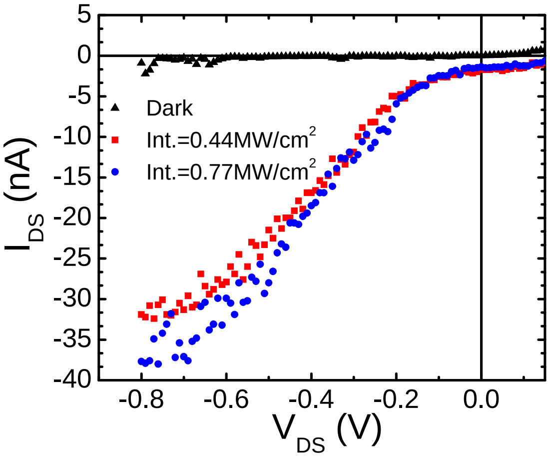

Figure 6.10. Reverse-bias region of the I_{DS}-V_{DS} behavior for device 2 with and without excitation at the p-n junction using a 633 nm laser. Laser intensities indicated.

6.7 Conclusion

We have presented a facile route to nearly ideal two-terminal carbon nanotube diodes that are stable in air. Raman spectroscopy and electrochemical gating measurements have been used to examine how the degree of doping and the doping profile along the length of the nanotube affect diode performance. With optimized doping levels, nearly ideal diode behavior without the need for an intrinsic region has been demonstrated. Initial studies on photovoltaic response presented here indicate that these devices perform comparably to electrostatically dual-gated nanotube diodes[9] without the need for cumbersome fabrication steps to define additional terminals and trenches to suspend the nanotube. Ease of doping and selective covalent silencing of metallic nanotubes can, in principle, allow one to create thin film carbon nanotube solar cell arrays for efficient energy harvesting for a distribution of wavelengths.

6.8 References

[1] Abdula, D.; Shim, M. *ACS Nano* **2008**, *2,* 2154.

[2] Tans, S. J.; Verschueren, A. R. M.; Dekker, C. *Nature*. **1998**, *393*, 49-52.

[3] Kong, J.; Franklin, N. R.; Zhou, C.; Chapline, M. G.; Peng, S.; Cho, K.; Dai, H. *Science*. **2000**, *287*, 622-625.

[4] Kang, S. J.; Kocabas, C.; Ozel, T.; Shim, M.; Pimparkar, N.; Alam, M. A.; Rotkin, S. V.; Rogers, J. A. *Nature Nanotechnology*. **2007**, *2*, 230-236.

[5] Sazonova, V.; Yaish, Y.; Ustunel, H.; Roundy, D.; Arias, T. A.; McEuen, P.L. *Nature*. **2004**, *431*, 284-287.

[6] Francois, L.; Tersoff, J. *Phys. Rev. Lett.* **1999**, *83*, 5174-5177.

[7] Esfarjani, K.; Farajian, A. A.; Hashi, Y.; Kawazoe, Y. *Appl. Phys. Lett.* **1999**, *74*, 79.

[8] Lee, J. U.; Gipp, P. P.; Heller, C. M. *Appl. Phys. Lett.* **2004**, *85*, 145.

[9] Lee, J. U. *Appl. Phys. Lett.* **2005**, *87*, 073101.

[10] Lee, J. U. *Phys. Rev. B.* **2007**, *75*, 075409.

[11] Bosnick, K.; Gabor, N.; McEuen, P. *Appl. Phys. Lett.* **2006**, *89*, 163121.

[12] Collins, P. G.; Bradley, K.; Ishigami, M.; Zettl A. *Science*. **2000**, *287*, 1801-1804.

[13] Sumanasekera, G. U.; Adu, C. K. W.; Fang, S.; Eklund, P. C. *Phys. Rev. Lett.* **2000**, *85*, 1096-1099.

[14] Dukovic, G.; et al. *J. Am. Chem. Soc*. **2004**, *126*, 15269-15276.

[15] Shim, M.; Back, J. H.; Ozel, T.; Kwon, K.-W. *Phys. Rev. B*. **2005**, *71*, 205411.

[16] Lee, R. S.; Kim, H. J.; Fischer, J. E.; Thess, A.; Smalley, R. E. *Nature*. **1997**, *388*, 255-257.

[17] Zhou, C.; Kong, J.; Yenilmez, E.; Dai, H. *Science*. **2000**, *290*, 1552-1555.

[18] Kong, J.; Dai, H. *J. Phys. Chem. B*. **2001**, *105*, 2890-2893.

[19] Li, Y. F.; Hatakeyama, R.; Shishido, J.; Kato, T.; Kaneko, T. *Appl. Phys. Lett.* **2007**, *90*, 173127.

[20] Takenobu, T.; Takano, T.; Shiraishi, M.; Murakami, Y.; Ata, M.; Kataura, H.; Achiba, Y.; Iwasa, Y. *Nature Materials*. **2003**, *2*, 683-688.

[21] Shim, M.; Javey, A.; Kam, N. W. S.; Dai, H. *J. Am. Chem. Soc*. **2001**, *123*, 11512-11513.

[22] Kurth, D. G.; Broeker, G. K.; Kubiak, C. P.; Bein, T. *Chem. Mater.* **1994**, *6*, 2143-2150.

[23] Rao, A. M.; Eklund, P. C.; Bandow, S.; Thess, A.; Smalley, R. E. *Nature.* **1997**, *388*, 257-259.

[24] Kazaoui, S.; Minami, N.; Matsuda, N.; Kataura, H.; Achiba, Y. *Appl. Phys. Lett.* **2001**, *78*, 3433.

[25] Kavan, L.; Rapta, P.; Dunsch, L.; Bronikowski, M. J.; Willis, P.; Smalley, R. E. *J. Phys. Chem. B.* **2001**, *105*, 10764-10771.

[26] Kavan, L.; Dunsch, L. *Nano Lett.* **2003**, *3*, 969-972.

[27] Shim, M.; Ozel, T.; Gaur, A.; Wang, C. *J. Am. Chem. Soc.* **2006**, *128*, 7522-7530.

[28] Tsang, J. C.; Freitag, M.; Perebeinos, V.; Liu, J.; Avouris, Ph. *Nature Nanotechnology*. **2007**, *2*, 725-730.

[29] Das, A.; Sood, A. K.; Govindaraj, A.; Saitta, A. M.; Lazzeri, M.; Mauri, F.; Rao, C. N. R. *Phys. Rev. Lett.* **2007**, *99*, 136803.

[30] Jorio, A.; et al. *Phys. Rev. B.* **2002**, *65*, 155412.

[31] Sze, S. M. Semiconductor Devices, Physics and Technology. In *p-n Junction*. John Wiley & Sons: Signapore, 1985; pp 92-95.

[32] Mahan, G. D. Many-Particle Physics. Plenum: New York, 1990.

[33] Ozel, T.; Gaur, A.; Rogers, J. A.; Shim, M. *Nano Lett.* **2005**, *5*, 905-911.

[34] Siddons, G. P.; Merchin, D.; Back, J. H.; Jeong, J. K.; Shim, M. *Nano Lett.* **2004**, *4*, 927-931

[35] Back, J. H.; Kim, S.; Mohammadi, S.; Shim, M. *Nano Lett.* **2008**, *8*, 1090-1094.

[36] Balasubramanian, K.; Fan, Y.; Burghard, M.; Kern, K. *Appl. Phys. Lett.* **2004**, *84*, 2400.

[37] Gabor, N. M.; Zhong, Z.; Bosnick, K.; Park, J.; McEuen, P. L. *Science* **2009**, *325*, 1367.

CHAPTER 7

SUMMARY AND FUTURE DIRECTION

7.1 Summary

A broad array of scientific aspects have been covered here, including elementary-quasi particle interactions, device fabrication and characterization, electronic and vibrational properties characterization in both the frequency and time domains, and even thermal transport. Chapter 1 motivated use of carbon nanotubes and graphene as promising materials for next generation electronics. Linear electronic dispersion results in high carrier mobility, the integral factor in materials selection for devices. Chapter 2 outlined different characterization, fabrication, and synthesis methods for making and understanding carbon nanotube/graphene devices and materials properties. High quality single-walled carbon nanotubes can be synthesized with chemical vapor deposition while mechanical exfoliation results in the best quality graphene. Device fabrication techniques with simple photolithography and metal evaporation provide means for electrical characterization using various gating geometries. Finally, our main method of characterization, Raman spectroscopy, was explained in detail for both static and time-domain measurements.

Changes in the Raman spectra of individual metallic single-walled carbon nantoubes (SWNTs) upon sidewall covalent bond formation have been described in Chapter 3. In light of the Fermi level shift dependent G-band lineshape and D-band intensity in metallic tubes, the validity of commonly used D to G intensity ratio as an assessment for covalent bond formation was first examined. G-band spectral evolution upon covalent reaction with 4-bromobenzene diazonium tetrafluoroborate was presented. The initial degree of disorder has a strong influence on covalent sidewall functionalization. Implications on developing electronically selective covalent chemistries and assessing their selectivity in separating metallic and semiconducting SWNTs were discussed.

Chapter 4 showed how doping and defects alter linewidth and lifetime of G-band optical phonons in carbon nanotubes. Optical phonon lifetime, T_1, in thin films of nanotubes was measured by time-resolved incoherent anti-stokes Raman spectroscopy and considered along with Raman linewidths of isolated individual nanotubes. Within the doping range achievable in nanotube films, T_1 did not appear to change. Varying degree of doping in individual nanotubes via electrostatic gating revealed decreasing full-width-at-half-maximum Γ down to ~4 cm^{-1} at the charge neutrality point. Increasing disorder, on the other hand, led to a decrease in T_1 along with an increase in Γ. A decrease in T_1 of ~0.4 ps at an estimated effective crystallite size L_a ~ 130 nm based on D-band to G-band peak intensity ratio was observed. In the limit of zero-doping and zero-defects, the measured Γ of single semiconducting nanotubes coincided with lifetime broadening of ~4 cm^{-1} based on measured T_1 of 1.2 ps. Samples displaying different degree of metallic/semiconducting contributions in their static Raman spectrum were also compared and shown to exhibit similar values of T_1.

Environment-induced effects on the E_{2G} G-band and A_1' 2D-band Raman spectral features of single-layer graphene were described in Chapter 5, providing insights on the intrinsic and extrinsic dependences of phonon energy and linewidth on temperature. Graphene prepared via mechanical exfoliation in air exhibited a G-band linewidth that increases with temperature between 298K and 573K but showed an opposite trend after being annealed under Ar. The opposing temperature dependences were considered within the context of Kohn anomaly induced phonon softening and broadening. The primary cause of the changes in E_{2G} phonon energy and the electron-phonon coupling was attributed to ambient O_2 shifting the Fermi level away from the Dirac point. Our results emphasized the need to carefully consider sample environment when investigating electronic and vibrational properties of graphene.

Finally, Chapter 6 outlined a method to construct two terminal abrupt junction diodes from single semiconducting carbon nanotubes with simple photolithographically patterned polymer layers defining air-stable p- and n-regions. These intratube diodes have shown nearly ideal behavior with relatively low series resistance and no sign of Zener breakdown at room temperature. Spatial doping profiles measured by Raman spectroscopy and selective electrochemical gating of the n-region indicated that diode performance depends strongly on relative doping levels. A short circuit current of 1.4 nA with an open circuit voltage of 205 mV were measured when illuminated to saturation.

7.2 Future Direction

Selectivity of covalent functionalization still needs to be improved. Chapter 3 details one out of a collection of possible reasons why selective functionalization of metallic carbon nanotubes in thin films is not optimal. Even with this knowledge, it is difficult to implement a solution since initial I_D/I_G values are solely a result of synthesis. In addition, the wide variety of electronic structures of individual tubes, as discussed in Chapter 1, is expected to produce a range of reactivity to a single reagent, even within the same nanotube type (metallic or semiconducting). This method must take advantage of the primary difference between semiconducting and metallic nanotubes, and that is the density of states at charge neutral. Since nanotubes are doped by ambient air, as discussed in Chapters 3, 4, and 6, it is necessary for thin films to be gated to their charge neutral position and then reacted. If one goes through the trouble of doing this, it is easier to just thermally break down metallic nanotubes with high bias since semiconducting nanotubes would be electrically insulating. Selective covalent chemistry of carbon nanotubes does not seem to be a good method for improving nanotube thin film devices. Chirality-dependent electronic properties is what makes nanotubes so exciting which is why chirality-controlled growth or post-synthesis sorting are what should be focused on.

Optical phonon (OP) lifetime studies in carbon nanotubes and graphene are in their infancy, primarily due to these materials just recently being discovered, but also because the advantages of such studies seem to be overlooked. For example, our study shows that for recently proposed phonon lasers to be feasible, it is important that sample quality be exceptional. Quantum computing power can also be significantly enhanced using phonons, such as with ion trap qubits where phonons act as a databus by coupling individual bits. Not only does the phonon population need to remain intact, but phonon dephasing must also be prevented. Therefore, material disorder must be controlled and doping effects on pure dephasing and population extinction must be fully understood. Another major concern is in the graphene electronics field where electrons may scatter with substrate polar phonon modes. OP lifetimes can be used to infer interactions between graphene and substrate which can lead to a better understanding of mobility limitations for non-suspended graphene devices.

The doping abilities of graphene and carbon nanotubes facilitate device fabrication. Chemical doping via adsorption as well as gate-induced carrier concentration control implies nanotube and graphene transistors can be realized. Importantly, due to these systems being nearly perfect 1D and 2D conductors having linear electronic dispersion with strong correlation allows previously impossible experimental physics to be feasible, such as in-depth studies on electron-phonon coupling. Ease of modulating carrier concentration adds another system variable that can be tuned. Electron-phonon coupling is not just the subject of interesting studies, but a practical issue as well, and its reduction at elevated temperatures is an advantage for carbon-based devices which, due to Joule heating, are expected to operate at higher temperatures. Because this phenomenon is doping dependent, it is also an advantage that it is an additional scattering mechanism at intrinsic carrier concentration when a transistor is desired to be insulating. Of course, in this state, OP decay paths are important so excessive heating does not ensue.

The culmination of all work presented here, taking advantage of everything discussed to some extent, would be arrays of carbon nanotube solar cells. Using information from Chapter 3, thin films of aligned carbon nanotubes would be functionalized to remove metallic nanotube conduction such that semiconducting films result. High doping sensitivity of sp^2-bonded carbon systems, studied in Chapter 5, would be utilized to construct functioning diodes, such as those described in Chapter 6, but on thin film devices which increases total active area footprint. These films would contain nanotubes of different diameters and, therefore, bandgaps which would be able to harvest a large range of the solar spectrum efficiently. Of course, the open circuit voltage would suffer and be only as large as the smallest bandgap within the nanotube array, but preferential functionalization of metallic carbon nanotubes may be reactive to small bandgap carbon nanotubes as well due to similarities in electronic structure. Finally optical phonon scattering would be suppressed with functionalization in metallic nanotube interconnects which could connect these devices together and serve as contacts. Conductivity may be preserved given the proper choice of functionalizing agent. [1]

7.3 References

[1] A. Lopez-Bezanilla, F. Triozon, S. Latil, X. Blasé, and S. Roche, Nano Lett. **9**, 940 (2009).

APPENDIX A

GUIDE TO OPERATING TIME-RESOLVED INCOHERENT ANTI-STOKES RAMAN SPECTROSCOPY APPARATUS

A. 1 Optics Table Setup

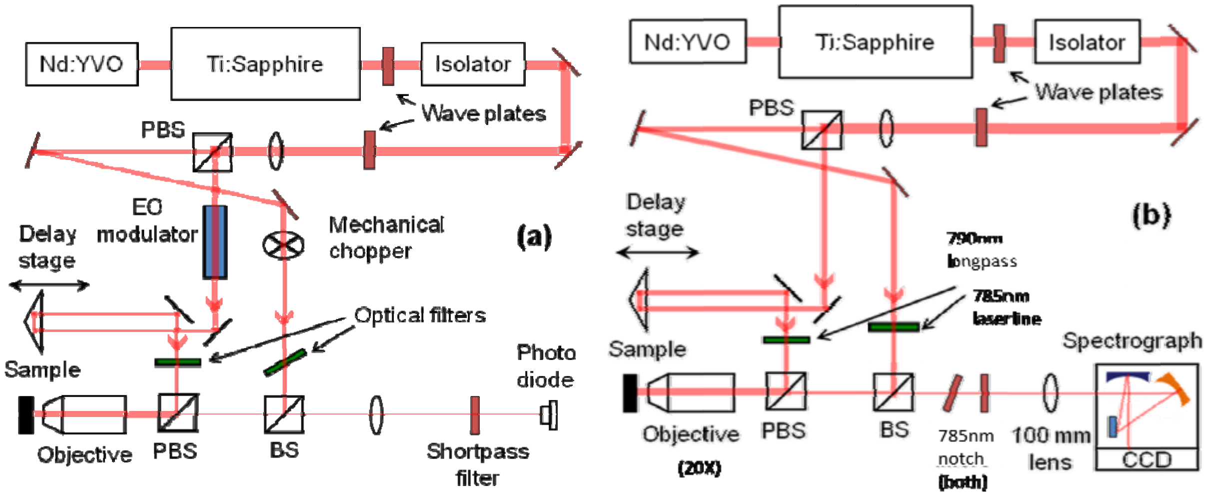

Figure A.1. Optics table setup for time-domain thermoreflectance (TDTR) (a) and time-resolved incoherent anti-Stokes Raman spectroscopy (TRIARS) (b).

1) Begin with TDTR setup which will be used to spatially overlap pump and probe beams.
2) Make sure pump and probe beams are incident perpendicular to 790nm and 785nm filters, respectively.
3) Tune laser to 787nm with 10nm linewidth mode-locked mode at 80MHz repetition.
4) Mount Leica 20x objective in holder and adjust position so that both pump and probe beams enter roughly through the center of the objective. This can be verified by observing beam path of reflected probe as it should hit the slit of the spectrometer.
5) Adjust waveplates so that pump:probe power ratios are 3:2. For thin film nanotube samples, a total power of 3.5mW is used. Graphene requires about 25mW.
6) Turn function generator on and set to 9.8MHz, 1.5Vpp amplitude square wave, and

0.75Vpp offset for the EO modulator. Turn chopper on and set to 200Hz. Mount sample.

7) Focus on substrate using a beam splitter projecting the image to the CCD camera (not shown). Another beam splitter can be placed just before the objective so a light source can be used to form a bright-field image of the substrate.
8) Remove two additional beam splitters used for imaging and adjust the Si diode position to get maximum signal from the reflected light. Note, the "shortpass filter" is <780nm.
9) Maximize in-phase signal by adjusting the polarizing beam splitter in the pump beam path. This signal is acquired from a lock-in amplifier and is read out in "pump-probe.vi".
10) Once the signal is maximized, the pump and probe beams are overlapped. Switch to TRIARS setup [Figure A.1(b)] and keep the shortpass filter in the beam path before the spectrometer.
11) Collect spectra and adjust the angle of the first 785nm notch filter after the objective to minimize the background and reflected light intensity.
12) Maximize Si/nanotube/graphene (the latter two being difficult to obtain signal for at 1s collection time) signal by moving the 100mm lens in the perpendicular directions to the beam path.
13) Set collection mode to "image" which maps the CCD array. Collect signal and adjust the 100mm lens along the direction of the beam path to narrow the Raman scattered light beam width as much as possible (can be 4-10 pixels usually).
14) Input the pixel range in which Raman scattered light is collected into the "multi-track" range. This reduces the background and stray noise.
15) Set collection time to desired value and data collection mode to "background subtracted". Set delay stage position to -10ps and collect a background spectrum. After this is done,

set the delay stage to desired time and collect signal. The spectrum should automatically be background subtracted.

16) Integrate peak areas and plot as a function of delay stage position. Fit to equation described in Chapter 2.

APPENDIX B

THERMAL TRANSPORT IN SUSPENDED BILAYER GRAPHENE

In this section, a discussion of heat transport in suspended bilayer graphene, as investigated experimentally with Raman spectroscopy is provided. The E_{2G} phonon energy shift is used to determine sample temperature and a simple method for determining laser power absorbed by graphene layers using optical imaging has been developed. Finite-element analysis is used to model the temperature profile in suspended sheets. Thermal conductivity κ of bilayer graphene in the diffusive regime is determined to be $\kappa = 123\ \mathrm{Wm^{-1}K^{-1}}$ at room temperature.

B. 1 Introduction

Decreasing size and dimensionality has led to a wealth of interesting phenomena that suggest many possibilities of performance limits beyond those of traditional materials. One exciting example is the thermal conductivity, κ, of single layer graphene (SLG) which has been calculated [1, 2], and, more recently, experimentally measured to be ~ 2200 to 5300 $\mathrm{Wm^{-1}K^{-1}}$ [3-5], even higher than that of diamond [6]. Such a high thermal conductivity may help in advancing thermoelectrics and facilitate thermal management in devices exploiting outstanding electronic performance of graphene [7, 8].

While a large body of work exists for graphite and even carbon nanotubes [9-13], experimental studies on κ of graphene, the parent material, have been quite limited. Only very recently, κ of suspended SLG has been reported utilizing a simple but elegant Raman approach where the incident laser heats the sample [3-5]. Here, we investigate thermal transport in bilayer graphene (BLG), potentially a technologically more relevant material having an electric field tunable bandgap [14]. While we also utilize the Raman approach [3], a general and a more direct way to experimentally determine absorbed laser power through simple contrast analysis in optical images of graphene is established. Such an approach is especially useful in instances, such as in devices, where transparent substrates may not be a viable option. Using finite-element analysis, temperature profiles within laser-irradiated suspended BLG sheets are determined which lead to a temperature-dependent thermal conductivity of $\kappa \sim 36900/T$ $Wm^{-1}K^{-1}$ in the Umklapp scattering regime.

B. 2 Experimental Details

Suspended BLG samples were prepared by mechanical exfoliation [15] of highly-oriented pyrolytic graphite (HOPG) on Si wafers with 300 nm oxide having predefined 2 or 5 μm wide trenches etched with RIE down to the Si. Figure B.1(a) shows an optical microscope image (illuminated with a halogen lamp through a 100X objective) of a suspended BLG sample. An atomic force microscope (Dimension 3100) image obtained after all data have been collected is shown in Figure B.1(b) to verify that the BLG remains suspended throughout the measurements. Raman spectroscopy is conducted with a Jobin Yvon LabRam HR 800 micro-Raman spectrometer with a 633 nm laser and a 100X air objective providing a $1/e^2$ spot size of 1 μm. The upper inset of the 2D band (~2630 cm^{-1}) in Figure B.2(a) shows a lineshape characteristic of BLG [16]. The D band is indicative of physical disorder [17] and is absent even at the highest incident laser power, P_I, showing that our measurements in ambient environment do not damage the BLG. Full range spectra taken before and after all data collection remain unchanged.

Thermal transport due to electrons is negligible [2] and is not considered in the subsequent discussion. Radiation and convection are also negligible [18] making all absorbed power, P_A, dissipate toward the trench edges. All finite-element simulations were carried out with the COMSOL software package.

B. 3 Results

In the absence of experimentally verified absorption cross-section, determining the power absorbed by BLG is non-trivial but is absolutely necessary for an accurate measurement of thermal conductivity where the incident laser is used as the heat source. Since graphene and carbon nanotubes are known not to reflect light [19, 20], the absorbed intensity is given by $\mathrm{I_A = (1 - T_{BLG}) I_I H}$ where $\mathrm{I_I}$ is the incident intensity, $\mathrm{T_{BLG}}$ is the transmission coefficient of BLG and H is the correction for interference due to laser coherence. Considering a simple traveling wave which reflects off the substrate, $\mathrm{I_A}$ = A*A where

$$\mathrm{A = A_I[\exp(\mathit{i}\,|\,k\,|\,r) + \sqrt{R_{Si}}\exp(\mathit{i}\varphi)\exp(-\mathit{i}\,|\,k\,|\,r)]} \qquad \text{Eq. B1}$$

with $\mathrm{A_I}$ being the incoherent light amplitude [$\mathrm{A_I^* A_I = (1\text{-}T_{BLG}) I_I}$], $k = 2\pi/\lambda$ is the light wavevector where λ is wavelength, $\mathrm{R_{Si}}$ is the silicon reflection coefficient, r is the position relative to the substrate surface, and $\varphi = \pi$ is the phase shift due to reflection. Therefore,

$$\mathrm{H = 1 + R_{Si} - 2\sqrt{R_{Si}}\cos(2\,|\,k\,|\,r)} \qquad \text{Eq. B2}$$

and, using λ = 633 nm, r = 300 nm, and $\mathrm{R_{Si}}$ = 0.35, H = 0.22. Contrast of a piece of graphene on substrate is defined as $\mathrm{C = 1 - I^R_{BLG}/I^R_{Si}}$, where $\mathrm{I^R_{BLG} = I_I R_{Si} (T_{BLG})^2}$ and $\mathrm{I^R_{Si} = I_I R_{Si}}$ are the intensities of the reflected beam in an area with and without BLG, respectively, leading to $T_{BLG} = \sqrt{1-C}$. In order to determine C, an optical image of each sample is passed through a software filter to extract out only the color corresponding to the 633 nm laser used (R, G, B = 255, 47, 0),[21] as shown in Figure B.1(c). This image is then used to obtain a line scan of the intensity profile along the path where bare Si is on one side and BLG over Si is on the other [Figure B.1(d)]. From 3 samples considered, T_{BLG} is determined to be 94.5 $\pm$ 0.3% and therefore, $I_A/I_I = P_A/P_I \sim 1\%$, where P_A and P_I are absorbed and incident powers, respectively. For comparison, SLG gives a value of $T_{SLG} = 96.3\%$ using this method. These values agree closely with Ref. [22] where $T_{BLG} \sim 95\%$ and $T_{SLG} \sim 97\%$ have been obtained by optical transmission measurements on large-area graphene supported on transparent substrates. We note that $T_{SLG} = 89\%$ of Refs. [3-5] has been calculated based on several assumptions including that Raman cross-sections and absorption coefficients of SLG and HOPG are the same. Differences in Raman cross-section might be difficult to analyze as it can be dependent on many factors, but absorption coefficient of HOPG is expected to be higher due to graphene's linear electronic dispersion which, according to this method of calculation, would make T_{SLG} larger. The smaller T_{SLG} used would lead to an overestimation of κ since less power is actually being conducted through the graphene. Our reflection method here, consistent with transmission measurements of Ref. [22], provides a simple experimental approach to determine the transmission coefficient of graphene layers potentially for any wavelength in the visible.

Having determined a method for estimating absorbed power, the temperature of BLG within the laser spot is needed which can be probed with Raman spectroscopy. Figure B.2(a) shows how the Γ-point E_{2G} phonon energy of suspended BLG decreases with increasing laser power for a 2 μm trench width sample. The E_{2G} peak (the G band) is fitted with one Lorentzian and the downshift with increasing P_I is shown in Figure B.2(b) for both suspended and supported areas of BLG and also in Figure B.2(c) for a 5 μm trench width sample. Linear fitting provides the laser power dependences of E_{2G} peak frequency of supported, $\omega_G^{Sub.}(P_I)$, and suspended, $\omega_G^{Sus.}(P_I)$, regions. To determine sample temperature from $\omega_G^{Sus.}(P_I)$, an independent measurement is carried out on an on-substrate sample at low laser intensity using a heating stage in the same manner as described for SLG in Ref. [23] and in Chapter 5. We obtain temperature dependence of E_{2G} peak frequency $\omega_G(T)$ = -0.0327 cm^{-1}/K × T + 1591.8 cm^{-1} for BLG as shown in the inset of Figure B.3.[24] It is important to emphasize that this relationship is for BLG on-substrate and that suspended samples might behave differently if substrate interactions are strong enough. Determining the relationship for suspended samples is difficult due to heat-induced rippling which affects ω_G simply from the strain.[25] Incident laser power dependent sample temperature, $T(P_I)$, for suspended and supported BLG are then obtained from $\omega_G^{Sus.}(P_I)$, $\omega_G^{Sub.}(P_I)$ and $\omega_G(T)$. $\omega_G^{Sus.}(P_I)$ is shown in the main panel of Figure B.3.

Note that $\omega_G(T)$ can be approximated to be linear with T only within a limited temperature range [23, 26]. $\omega_G(T)$ for our BLG sample has been determined in the temperature range of 300 - 573 K, a similar range as our thermal conductance measurements. We have also previously determined the temperature coefficient, or the slope of linearized $\omega_G(T)$, for SLG as χ_{SLG} = -0.035 cm^{-1}/K in the same temperature range [23]. These results are significantly different from χ_{SLG} = -0.016 cm^{-1}/K for 83 K < T < 373 K of Ref. [27] which has been used to calculate κ_{SLG} in Refs. [3-5]. Although we used a different laser energy than Ref. [27], ω_G is not dependent on excitation energy because it is a single-resonance scattering process. The choice of appropriate range of calibration is important in determining sample temperature of graphene and therefore critical in calculating values of thermal conductivity.

Using $\omega_G(T)$ allows us to estimate the temperature of BLG within the laser spot. This information, in conjunction with the approximate power absorbed from the laser, provides a way to extract κ through finite-element analysis. We first assume that $\kappa(\mathrm{T}) \propto 1/\mathrm{T}$ for T greater than room temperature, a reasonable assumption given this is observed for carbon nanotubes.[13] We also estimate the BLG thickness as 2×0.345nm and assume the temperatures we extract from Raman thermometry are those at the $1/e^2$ radius of the Gaussian intensity distribution. Despite this being a crude approximation, it should be noted that the G-band frequency itself is a collective average from the entire laser spot size and, thus, should correspond to the "average" of a Gaussian laser spot which is typically considered to be the $1/e^2$ radius. Finally, as discussed earlier, all heat dissipation is expected to be via conduction to the substrate for which we use a thermal resistance of 5.6×10^{-9} m^2K/W for the graphene-substrate interface.[28]

Results for the suspended BLG sample having a 5 μm wide trench are summarized in Figure B.4. Thermal coupling to the SiO_2 substrate is strong as it takes the heat only ~200 nm past the trench edge to dissipate. This particular simulation was for a laser power of $P_l = 10$mW which resulted in $\kappa = 47400/\mathrm{T}$ $\mathrm{Wm^{-1}K^{-1}}$. An average of the three simulations done here, for $P_l = 10$, 4.9, and 2.1 mW, yields an overall thermal conductivity of $\kappa = 36900/\mathrm{T}$ $\mathrm{Wm^{-1}K^{-1}}$. Therefore, at room temperature, $\kappa = 123$ $\mathrm{Wm^{-1}K^{-1}}$, comparable to that reported for single layer graphene encased in SiO_2.[29]

B. 4 Conclusion

We have demonstrated a simple experimental method for determining the optical transmission coefficient of SLG and BLG which in turn allow measurements of the power absorbed from laser excitation. Along with *T* dependence of Raman G band shift in the appropriate *T* range established here, consideration of predominant heat dissipation into the substrate near the trench edges allows for the determination of κ for BLG. In the regime where Umklapp scattering dominates, $\kappa \sim 37000/T$ $Wm^{-1}K^{-1}$.

B.5 Acknowledgements

We thank Zhun-Yong Ong and Eric Pop for the simulation work as well as the valuable discussions regarding the experiments and results presented here.

B. 6 References

[1] Kong, B. D.; Paul, S.; Nardelli, M. B.; Kim, K. W., *Phys. Rev. B* **2009**, *80*, 033406.

[2] Saito, K.; Nakamura, J.; Natori, A., *Phys. Rev. B* **2007**, *76*, 115409.

[3] Balandin, A.A.; Ghosh, S.; Bao, W.; Calizo, I.; Teweldebrhan, D.; Miao, F.; Lau, C. N., *Nano Lett.* **2008**, *8*, 902.

[4] Ghosh, S.; Calizo, I.; Teweldebrhan, D.; Pokatilov, E. P.; Nika, D. L.; Balandin, A. A.; Bao, W.; Miao, F.; Lau, C. N., *Appl. Phys. Lett.* **2008**, *92*, 151911.

[5] Ghosh, S.; Nika, D. L.; Pokatilov, E. P.; Balandin, A. A., *New J. Phys.* **2009**, *11*, 095012.

[6] Onn, D. G.; Witek, A.; Qiu, Y. Z.; Anthony, T. R.; Banholzer, W. F., *Phys. Rev. Lett.* **1992**, *68*, 2806.

[7] Du, X.; Skachko, I.; Barker, A.; Andrei, E. Y., *Nat. Nanotechnol.* **2008,** *3*, 491.

[8] Morozov, S. V.; Novoselov, K. S.; Katsnelson, M. I., Schedin, F.; Elias, D. C.; Jaszczak, J. A.; Geim, A. K., *Phys. Rev. Lett.* **2008,** *100*, 016602.

[9] Smith, A. W., *Phys. Rev.* **1954**, *95*, 1095.

[10] Tyler, W. W.; Wilson Jr., A. C., *Phys. Rev.* **1953**, *89*, 870.

[11] Kim, P.; Shi, L.; Majumdar, A.; McEuen, P. L., *Phys. Rev. Lett.* **2001**, *87*, 215502.

[12] Yu, C.; Shi, Li; Yao, Zhen; Li, D.; Majumdar, A., *Nano Lett.* **2005**, *5*, 1842.

[13] Pop, E.; Mann, D.; Wang, Q.; Goodson, K.; Dai, H., *Nano Lett.* **2006**, *6*, 96.

[14] Zhang, Y.; Tsung-Ta, T.; Girit, C.; Hao, Z.; Martin, M. C.; Zettl, A.; Crommie, M. F.; Shen, Y. R.; Wang, F., *Nature* **2009**, *459*, 820.

[15] Novoselov, K. S.; Jiang, D.; Schedin, F.; Booth, T. J.; Khotkevich, V. V.; Morozov, S. V.; Geim, A. K., *Proc. Natl. Acad. Sci.* **2005**, *102*, 10451.

[16] Ferrari, A. C.; Meyer, J. C.; Scardaci, V.; Casiraghi, C.; Lazzeri, M.; Mauri, F.; Piscanec, S.; Jiang, D.; Novoselov, K. S.; Roth, S.; Geim, A. K., *Phys. Rev. Lett.* **2006**, *97*, 187401.

[17] Abdula, D.; Nguyen, K. T.; Shim, M., *J. Phys. Chem. C* **2007**, *111*, 17755.

[18] Freitag, M.; Steiner, M.; Martin, Y.; Perebeinos, V.; Chen, Z.; Tsang, J. C.; Avouris, Ph., *Nano Lett.* **2009**, *9*, 1883.

[19] Blake, P.; Hill, E. W.; Castro Neto, A. H.; Novoselov, K. S.; Jiang, D.; Yang, R.; Booth, T. J.; Geim, A. K., *Appl. Phys. Lett.* **2007**, *91*, 063124.

[20] Mizuno, K.; Ishii, J.; Kishida, H.; Hayamizu, Y.; Yasuda, S.; Futaba, D. N.; Yumura, M.; Hata, K., *Proc. Natl. Acad. Sci.* **2009**, *106*, 6044.

[21] The GNU Image Manipulation Program (GIMP) was used. Under “Color Tools”, the “Levels” tool was selected where Red was set from 0 to 255, Green from 0 to 47, and Blue from 0 to 0.

[22] Li, X.; Zhu, Y.; Cai, W.; Borysiak, M.; Han, B.; Chen, D.; Piner, R. D.; Colombo, L.; Ruoff, R. R., *Nano Lett.* **2009**, *9*, 4359.

[23] Abdula, D.; Ozel, T.; Kang, K.; Cahill, D. G.; Shim, M., *J. Phys. Chem. C* **2008**, *112*, 20131.

[24] This relationship accounts for slight heating by laser power of 3 mW used which artificially downshifts $\omega_G(T)$. $\omega_G^{Sub.}(P_I = 0\ mW) - \omega_G^{Sub.}(P_I = 3\ mW) \sim 1\ cm^{-1}$ is added to each raw datapoint that determines $\omega_G(T)$, thereby subtracting laser heating effects resulting in the relationship shown in the inset of Figure B.3.

[25] Chen, C. C.; Bao, W.; Theiss, J.; Dames, C.; Lau, C. N.; Cronin, S. B., *Nano Lett.* **2009,** *9*, 4172.

[26] Bonini, N.; Lazzeri, M.; Marzari, N.; Mauri, F., *Phys. Rev. Lett.* **2007**, *99*, 176802.

[27] Calizo, I.; Miao, F.; Bao, W.; Lau, C. N.; Balandin, A. A., *Appl. Phys. Lett.* **2007**, *91*, 071913.

[28] Chen, Z.; Jang, W.; Bao, W.; Lau, C. N.; Dames, C., *Appl. Phys. Lett.* **2009**, *95*, 161910.

[29] Jang, W.; Chen, Z.; Bao, W.; Lau, C. N.; Dames, C., *Nano Lett.* **2010**, *10*, 3909.

B. 7 Figures

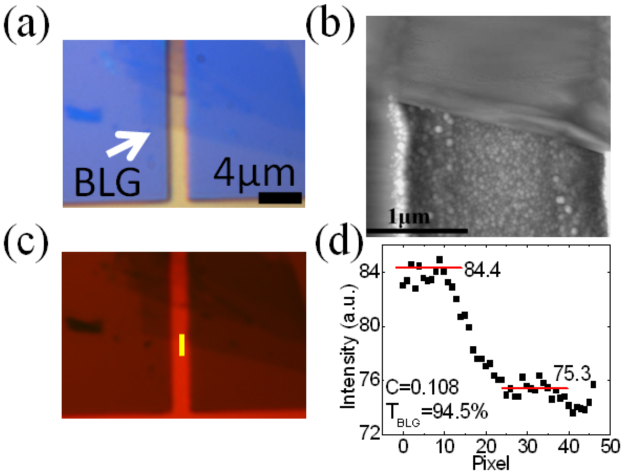

Figure B.1. (a) Optical image of BLG sample with 2 µm trench width obtained with a halogen white light. (b) Tapping mode AFM image of suspended BLG area. (c) Optical image in (a) after it has been passed through a software filter leaving color equivalent to 633 nm remaining. Yellow line represents the line scan of which the intensity profile is shown in (d).

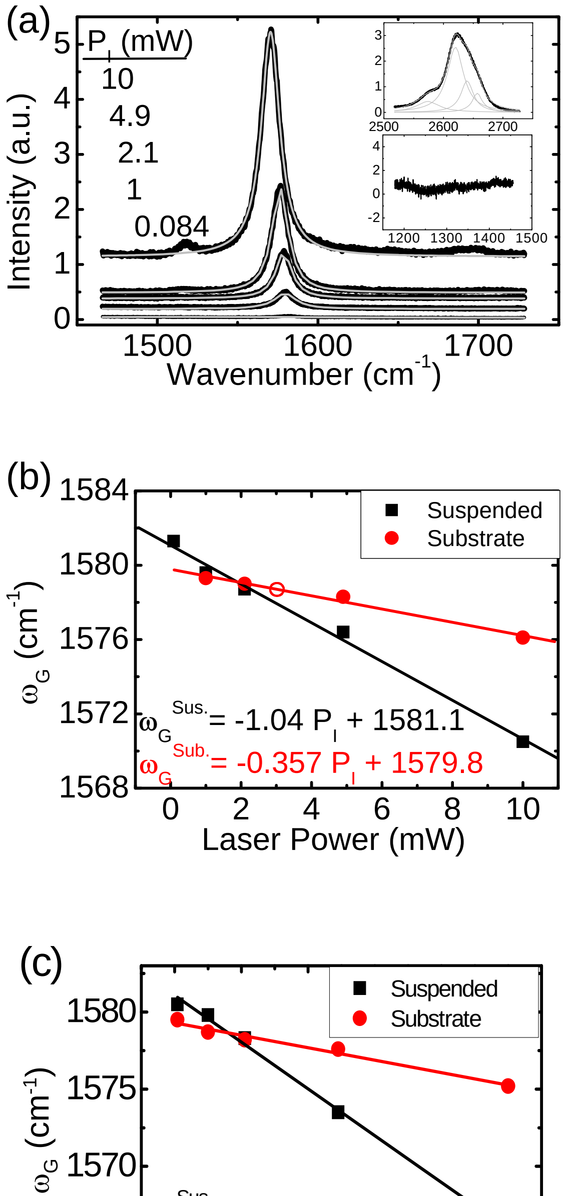

Figure B.2. (a) Raman spectra of the E_{2G} phonon peak and its dependence on laser power, P_l, for 2 um trench width sample. Spectra are offset for clarity. Lorentzian fits are shown in gray. Taken at the highest P_l, the 2D band (upper inset) verifies the samples are bilayer and the D band (lower inset) shows no defects arise from laser heating, as is the case for all samples tested. E_{2G} phonon peak frequency, ω_G, dependence on P_l for on-substrate and suspended portions of BLG for (b) 2 µm trench and (c) 5 µm trench samples. Open circle represents point used for laser heating correction in the calibration data relating ω_G to temperature [23].

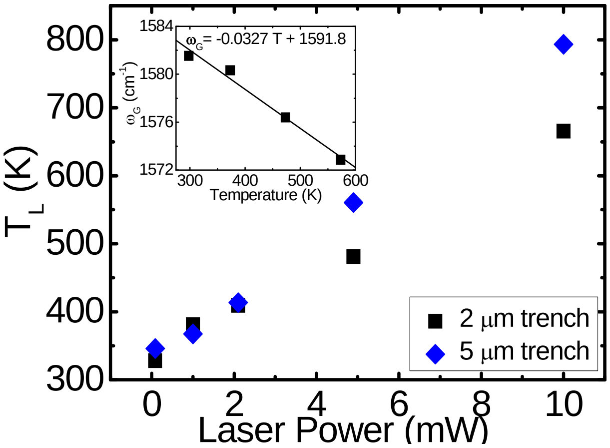

Figure B.3. Dependence of absolute temperature of suspended BLG at laser spot position with laser power. Inset is the calibration data used for determining sample temperature from the E_{2G} peak position, as described in the text.

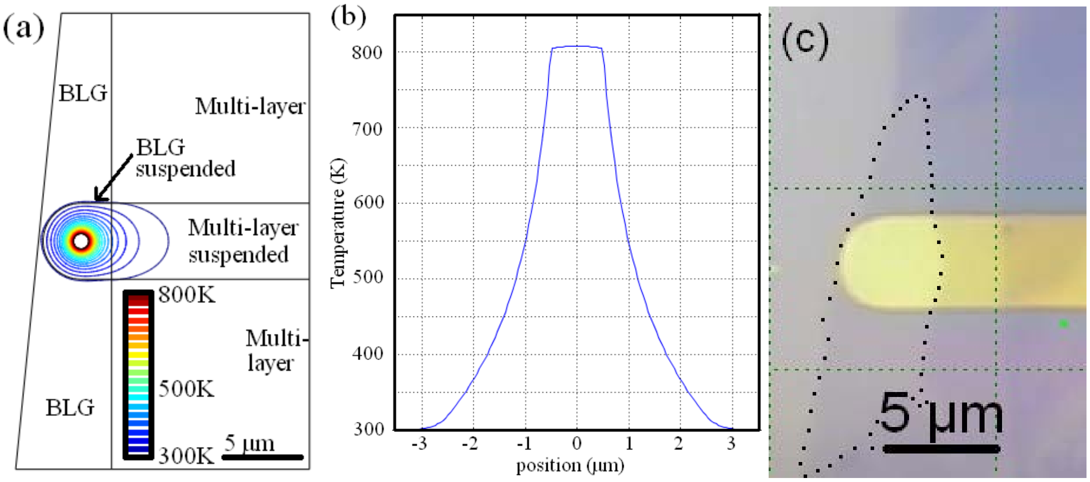

Figure B.4. (a) Temperature profile of suspended BLG anchored to SiO$_2$/Si substrate for P_I = 10mW. Areas of BLG and multi-layer graphene are indicated. Suspended regions are noted. (b) Cross-section of BLG temperature profile along the vertical direction in (a). Trench edges are at ±2.5 μm. (c) Optical image of the corresponding sample with BLG area outlined.